

学位論文

**Pressure-induced phase transitions of metastable phases  
of calcium carbonate**

(炭酸カルシウム準安定相の圧力誘起相転移)

平成 27 年 12 月 博士 (理学) 申請

東京大学大学院理学系研究科  
化学専攻

丸山 浩司



## Abstract

Calcium carbonate,  $\text{CaCO}_3$ , is a ubiquitous mineral on the Earth's surface. Calcium carbonate has three anhydrous polymorphs (calcite, aragonite, and vaterite) at ambient pressure. In addition to these crystalline phases, amorphous calcium carbonate (ACC:  $\text{CaCO}_3 \cdot x\text{H}_2\text{O}$ ,  $x \leq 1.5$ ) is known as a precursor of more stable crystalline phases in biomineralization and inorganic formation. In nature, ACC exists only in biominerals. Calcium carbonate crystals with complex morphology are formed via ACC in biomineralization. Therefore, the crystallization from ACC is an important process to understand biomineralization. It is already known that ACC crystallizes to calcite via anhydrous ACC by heating (e.g., Kojima et al., 1993). In a super-saturated solution, Rodriguez-Blanco et al. (2011) reported the crystallization from ACC to calcite via vaterite by time-resolved XRD measurements. Recently, Yoshino et al. (2012) presented a different type of crystallization process, pressure-induced crystallization from ACC at room temperature. The pressure-induced crystallization from ACC resulted in coexistence of calcite and vaterite, a metastable phase of calcium carbonate, occurred below 1 GPa. The crystallization mechanism of ACC is still unclear, because previous experiments were based on observations of recovered samples. Moreover, pressure responses of calcium carbonate polymorphs would provide useful information for the crystallization from ACC at high pressure. Many studies have investigated the high-pressure behavior of calcite and aragonite. On the other hand, no report described the pressure response of vaterite. In this study, to elucidate the mechanism of pressure-induced crystallization from ACC, I conducted in situ X-ray diffraction (XRD) observations on ACC and vaterite at high pressure.

Chapter 2 describes basic properties of ACC used in this study and pressure-induced crystallization from ACC based on observations of the recovered samples using a piston-cylinder. XRD patterns of synthesized ACCs with different water contents and its recovered samples from high pressure are presented in Fig. 1. ACC crystallized to calcite and vaterite by applying pressure ( $< 1$  GPa) at room temperature. The vaterite/calcite ratios decreased with increase of applied pressure. ACC with lower  $\text{H}_2\text{O}$  content needed higher pressure for its crystallization than ACC with higher  $\text{H}_2\text{O}$  content did. Moreover, this crystallization was associated with dehydration. These results indicate that  $\text{H}_2\text{O}$  in ACC plays an important role in the crystallization process.

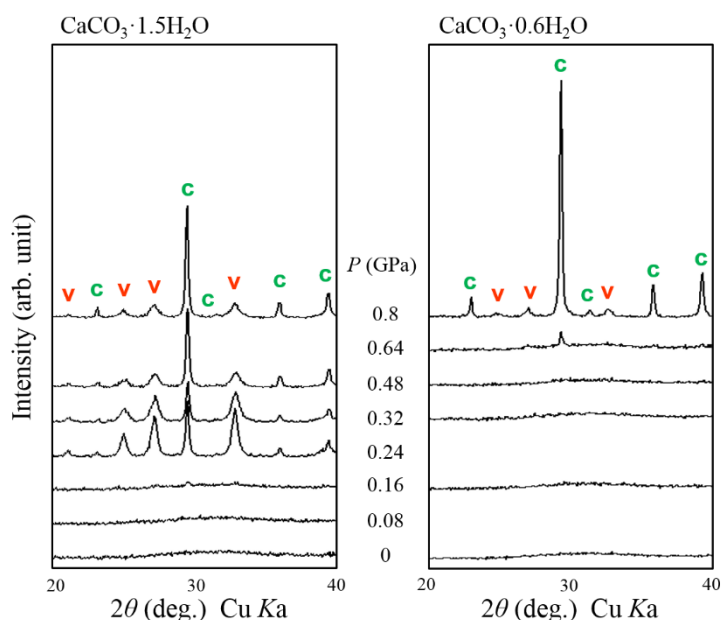


**Fig. 1.** XRD patterns of synthesized ACC ( $\text{CaCO}_3 \cdot 1.5\text{H}_2\text{O}$  and  $\text{CaCO}_3 \cdot 0.6\text{H}_2\text{O}$ ) and its recovered samples from high pressure: **c**, calcite; **v**, vaterite.

In Chapter 3, in situ time-resolved X-ray diffraction studies are presented to understand the mechanisms and kinetics of pressure-induced crystallization from ACC to calcite and vaterite. The SEM observations were also conducted to obtain more information of the crystallization mechanism. High pressure was generated using the cubic-type high-pressure apparatus (MAX80) at the Photon Factory–Advanced Ring (PF–AR), KEK. In order to control pressure precisely at a low-pressure range, below 1 GPa, a relatively large truncated edge length of 10 mm for the second stage anvil made by WC was used. Figure 2 shows time-resolved XRD patterns obtained for every 10 seconds. From the XRD results, degree of transformation is represented in Fig. 3a, suggesting that calcite and vaterite simultaneously crystallized from ACC. To understand the mechanism of pressure-induced crystallization from ACC, I introduced Avrami model (Fig. 3b). The  $n$  value in Avrami model

is a constant dependent on the nucleation and crystal growth process at time. The obtained  $n$  values suggest that the formation of calcite is more controlled by the nucleation process than that of vaterite is. However, the grain sizes of calcite and vaterite observed from SEM images are about 100 to 200 nm; there is no significant difference in the grain size between calcite and vaterite (see Fig. 4a and 4b). Figure 4c shows the polymorph distributions in the recovered sample determined from Raman spectra. Vaterite mainly distributed around cavities, which would be filled with aqueous fluid dehydrated from ACC.

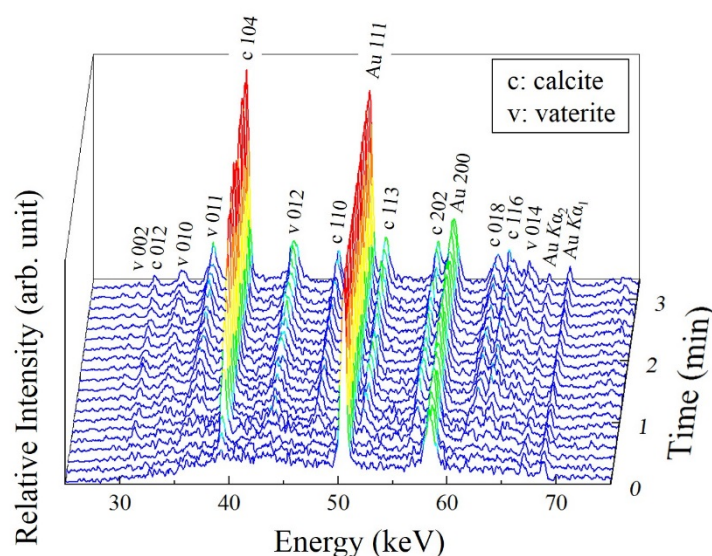


**Fig. 2.** Time-resolved X-ray diffraction patterns of ACC ( $\text{CaCO}_3 \cdot 0.67\text{H}_2\text{O}$ ) with Au powder during compression. Intensity was normalized by the diffraction intensity from the 111 reflection of Au. Indices of vaterite were referred from the structure model proposed by Kamhi (1963).

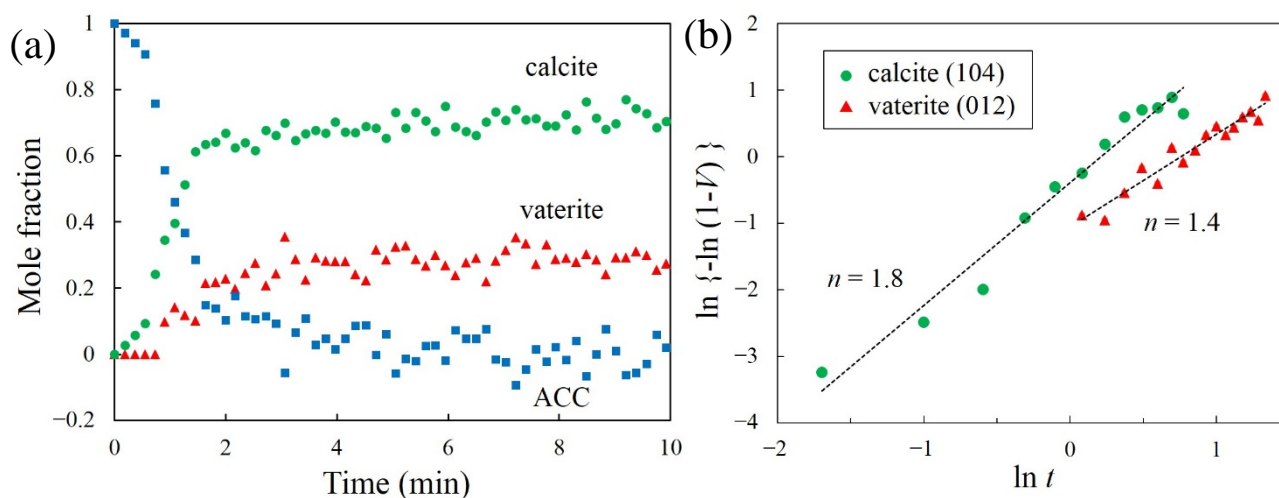


**Fig. 3.** (a) Degree of transformation determined from the intensities of vaterite 010 and calcite 104 reflections as a function of time. The vaterite/calcite ratio was calculated using the calibration line described in Chapter 2. The fraction of ACC was estimated from the balance of calcite and vaterite. (b) Plots of Avrami fitting for calcite (104 reflection) and vaterite (012 reflection) during crystallization from ACC.

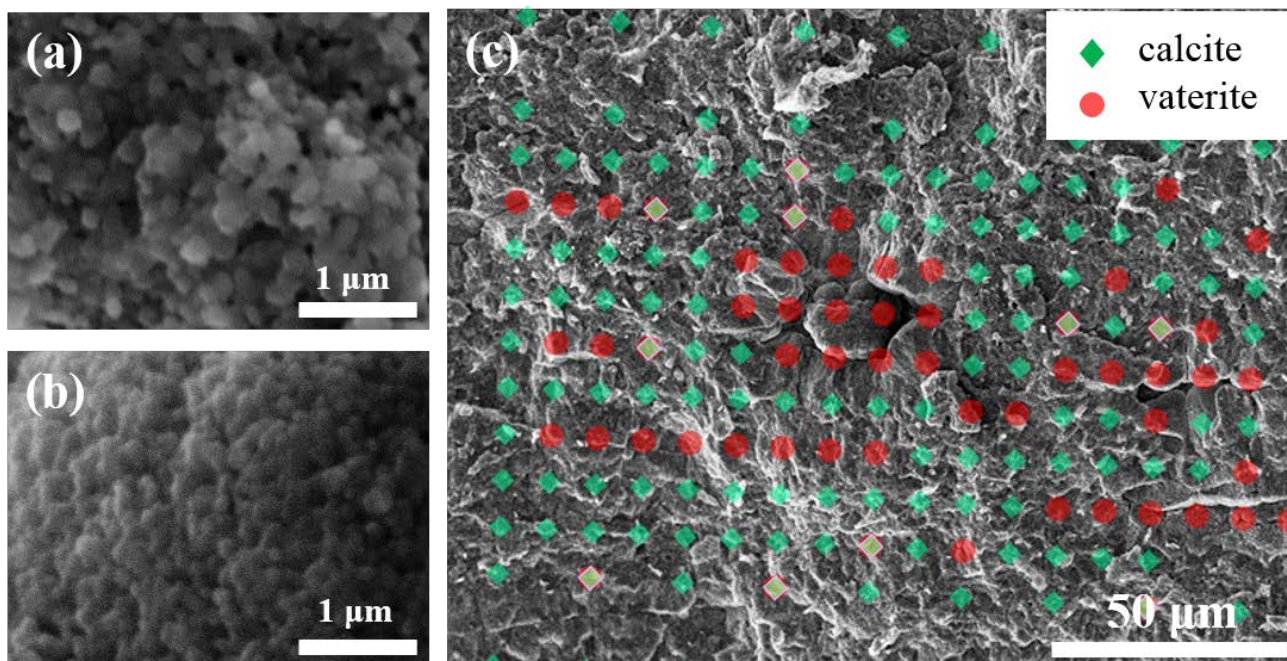


**Fig. 4.** SEM images of a recovered run product: (a) calcite, (b) vaterite, and (c) polymorph distribution on an SEM image determined with Raman mapping.

This observation suggests that the formation of vaterite strongly connects to the existence of fluid. In contrast, calcite distributed throughout the sample. Moreover, calcite exhibited a spherical texture which is the pseudomorph of ACC, which suggests that calcite crystallized directly from ACC. These results indicate that the crystallization mechanisms from ACC to calcite and vaterite differ from each other, and this difference might result in the difference in the  $n$  values.

In Chapter 4, the pressure responses of vaterite were studied using diamond anvil cells (DACs). Representative XRD patterns obtained on a synchrotron beamline at PF are shown in Fig. 5. At 4.7 GPa, several peaks of vaterite were split and new peak attributable to calcite III appeared. The unit-cell parameters refined using a crystal structure model proposed by Le Bail et al. (2011) suggests that vaterite (vaterite I)

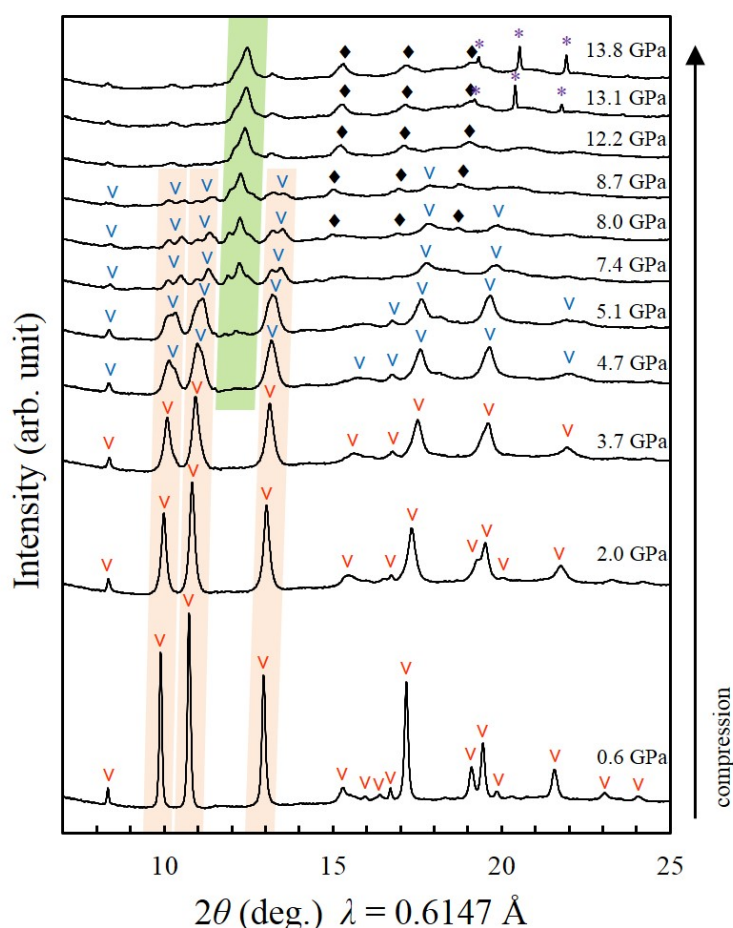


**Fig. 5.** Representative XRD patterns at high pressure with compression. The intensity has been normalized to the same measurement time. v, vaterite I; v, vaterite II; ♦, vaterite III; \*, vaterite IV. The orange- and green-shaded regions indicate the highest intensity peaks of vaterite and calcite III, respectively.

transformed to a high-pressure phase (vaterite II) at 4.7 GPa. Vaterite II was more compressible than vaterite I was. At 8.7 GPa, another phase transition was observed with discontinuous changes of  $2\theta \approx 8.3^\circ$ . This change suggests that vaterite II transformed to a new phase, vaterite III. These phase transitions were also suggested by Raman spectra. At 13.1 GPa, new diffraction spots were observed around  $20^\circ$  in  $2\theta$ . These spots were not explainable with any polymorphs of calcium carbonate. This implies that these spots are derived from another high-pressure phase of vaterite (vaterite IV). At ambient pressure after decompression, the recovered sample was identified as a mixture of calcite I and vaterite. This observation suggests that vaterite II transformed to calcite III irreversibly.

For summary of this study, in situ observations of ACC and vaterite at high pressure provided us the information of crystallization mechanism from ACC at high pressure. The crystallization from ACC to calcite and vaterite proceeded by different mechanisms. ACC transformed to calcite directly by solid-to-solid phase transition accompanied by dehydration, which differs from the mechanism of calcite formation via vaterite in a super-saturated solution. The high-pressure experiments on vaterite, which clarified that vaterite does not transform to calcite at pressures lower than 4 GPa, supports the direct formation of calcite from ACC at high pressure. In contrast, ACC transformed to vaterite in dehydrated fluid, for example, a dissolution-reprecipitation process.

# Table of Contents

<b>Abstract</b> .....	<b>i</b>
<b>Table of Contents</b> .....	<b>v</b>
<b>Chapter 1. General Introduction of calcium carbonate</b> .....	<b>1</b>
1.1. Calcium carbonate (CaCO <sub>3</sub> ) .....	2
1.2. Polymorphs of calcium carbonate .....	3
1.3. Pressure responses of crystalline phases of calcium carbonate .....	6
1.4. Amorphous calcium carbonate (ACC) .....	8
1.5. Crystallization from ACC .....	10
1.6. Purpose and contents of this study .....	14
References .....	16
<b>Chapter 2. Basic properties of ACC: experimental identification and pressure response</b> .....	<b>21</b>
2.1. Introduction .....	22
2.2. Experimental procedures .....	23
2.2.1. Synthesis of ACC .....	23
2.2.2. Control of water contents in ACC .....	23
2.2.3. Thermal analysis .....	23
2.2.4. Powder X-ray diffraction .....	24
2.2.5. Infrared spectroscopy .....	24
2.2.6. Structural analysis .....	25
2.2.7. Setup for high-pressure experiments .....	27
2.3. Results and discussion .....	28

2.3.1.	Basic properties of ACC .....	28
2.3.1.1.	Thermal analysis.....	28
2.3.1.2.	X-ray diffraction .....	32
2.3.1.3.	IR spectroscopy .....	35
2.3.1.4.	Structural analysis using atomic pair distribution function (PDF) .....	38
2.3.2.	High-pressure experiments of ACC for recovered samples .....	40
2.3.2.1.	X-ray diffraction patterns .....	40
2.3.2.2.	Pressure-induced crystallization process .....	45
2.4.	Conclusion .....	47
	References .....	48

**Chapter 3. Kinetic observation of pressure-induced crystallization of ACC: in situ time-resolved X-ray observation and observation by SEM and Raman spectroscopy ..... 51**

3.1.	Introduction .....	52
3.2.	Experimental procedures.....	53
3.2.1.	Sample preparation .....	53
3.2.2.	Setup for high-pressure experiments .....	54
3.2.3.	In situ X-ray diffraction observations at high pressure .....	57
3.2.4.	SEM observations for the recovered samples.....	59
3.3.	Results and discussion .....	60
3.3.1.	Time-resolved X-ray diffraction .....	60
3.3.2.	Estimation of pressure .....	61
3.3.3.	Kinetics of pressure-induced crystallization from ACC.....	64
3.3.4.	Microtexture of the recovered samples .....	67
3.3.5	Mechanism of pressure-induced crystallization form ACC .....	71
3.4.	Conclusion .....	73
	References .....	74

<b>Chapter 4. Pressure response of vaterite: in situ observation at high pressure by powder X-ray diffraction and Raman spectroscopy.....</b>	<b>77</b>
4.1. Introduction.....	78
4.2. Experimental procedures.....	79
4.2.1. Synthesis of vaterite.....	79
4.2.2. Setup for high-pressure experiments .....	80
4.2.3. Powder X-ray diffraction.....	81
4.2.4. Raman spectroscopy .....	82
4.3. Results and discussion .....	83
4.3.1. X-ray diffraction patterns at high pressure with compression.....	83
4.3.2. Determination of unit-cell parameters and bulk moduli.....	85
4.3.3. High-pressure phases of vaterite at pressures higher than 8 GPa.....	90
4.3.4. X-ray diffraction patterns at high pressure with decompression .....	92
4.3.5. Raman spectroscopy on vaterite and calcite at high pressure .....	95
4.3.6. Summary of phase transitions of vaterite at high pressure.....	99
4.4. Conclusion .....	100
References.....	101
 <b>Chapter 5. Conclusions of this thesis.....</b>	 <b>105</b>
 <b>Acknowledgements.....</b>	 <b>108</b>



## **Chapter 1.**

### **General introduction of calcium carbonate**

## **1.1. Calcium carbonate (CaCO<sub>3</sub>)**

Calcium carbonate is a ubiquitous mineral on the Earth's surface. Calcium carbonate is known as a major CO<sub>2</sub> reservoir, and plays an important role in the global carbon cycle. Calcium carbonate can form not only in inorganic system but also under biological control. From this reason, calcium carbonate is a major chemical substance of biominerals, which are mineralized tissues produced by living organisms. For example, shells, corals, and exoskeletons of Crustacea consist of calcium carbonate. Moreover, foraminifers and coccolithophores, which are planktons producing biominerals of calcium carbonate, contribute to the formation of most of deep-sea sediments (Schiebel, 2002).

Calcium carbonate attracts attentions not only for natural systems but also in industrial applications. For example, calcium carbonate is used for rubbers, paints, chalks, paper manufacturing and so on. On the other hand, scale formation (incrustation) of calcium carbonate can result in significant obstruction problems in machines and pipes. To understand the properties of calcium carbonate is also required for the inhabitation of the scale formation.

Because of its abundance and importance for geoscience and industrial fields, the calcium carbonate system has been investigated for a long time. However, there are still many unsolved problems on calcium carbonate, in spite of a number of previous researches. For example, Gebauer et al. (2008) suggested the existence of stable prenucleation calcium carbonate clusters instead of the classical nucleation theory; nucleation occurs when metastable clusters grow larger than critical size. The mechanism of precipitation from the stable clusters remains still unknown. It needs further researches on calcium carbonate system to understand geoscience and to advance industrial applications.

## 1.2. Polymorphs of calcium carbonate

Calcium carbonate has six forms as described in Table 1–1. Calcite, aragonite, and vaterite are anhydrous crystalline phases of calcium carbonate. Figure 1–1 shows the crystal structures of these anhydrous phases, each of them having different stacking of calcium atoms. In a broader definition, following two hydrous crystalline phases are often categorized as polymorphs of calcium carbonate; monohydrocalcite (MHC) and ikaite (hexahydrate calcium carbonate, HCC) described as  $\text{CaCO}_3 \cdot \text{H}_2\text{O}$  and  $\text{CaCO}_3 \cdot 6\text{H}_2\text{O}$ , respectively. In addition to these crystalline phases, amorphous calcium carbonate (ACC) is known as an intermediate phase precipitated from a highly supersaturated solution (Ogino et al., 1987). Generally, ACC is a hydrated phase described as  $\text{CaCO}_3 \cdot x\text{H}_2\text{O}$  ( $x \leq \sim 1.5$ ). Basic properties of these forms are listed in Table 1–1.

Table 1–1. Polymorphs of calcium carbonate

CaCO <sub>3</sub> forms	chemical formula	crystal system	density (g cm <sup>-3</sup> )	solubility -log K <sub>sp</sub> at 25 °C
calcite	CaCO <sub>3</sub>	trigonal	2.71* <sup>1</sup>	8.48* <sup>6</sup>
aragonite	CaCO <sub>3</sub>	orthorhombic	2.93* <sup>2</sup>	8.34* <sup>6</sup>
vaterite	CaCO <sub>3</sub>	(#)	2.65* <sup>3</sup>	7.91* <sup>6</sup>
monohydrocalcite	CaCO <sub>3</sub> ·H <sub>2</sub> O	trigonal	2.42* <sup>4</sup>	7.15* <sup>7</sup>
ikaite	CaCO <sub>3</sub> ·6H <sub>2</sub> O	monoclinic	1.73* <sup>5</sup>	6.59* <sup>8</sup>
ACC	CaCO <sub>3</sub> ·xH <sub>2</sub> O (x ≤ 1.5)	–	–	6.40* <sup>9</sup>

(#) Vaterite structure has been controversial. Historically, two crystal structure models with hexagonal and orthorhombic symmetries have been proposed.

\*1 Markgraf and Reeder (1985); \*2 De Villiers (1971), Dal Negro and Ungaretti (1971); \*3 Kamhi (1963); \*4 Swainson (2008); \*5 Hesse et al. (1983); \*6 Plummer and Busenberg (1982); \*7 Kralj and Brecevic (1995); \*8 Bischoff et al. (1993); \*9 Brečević and Nielsen (1989)

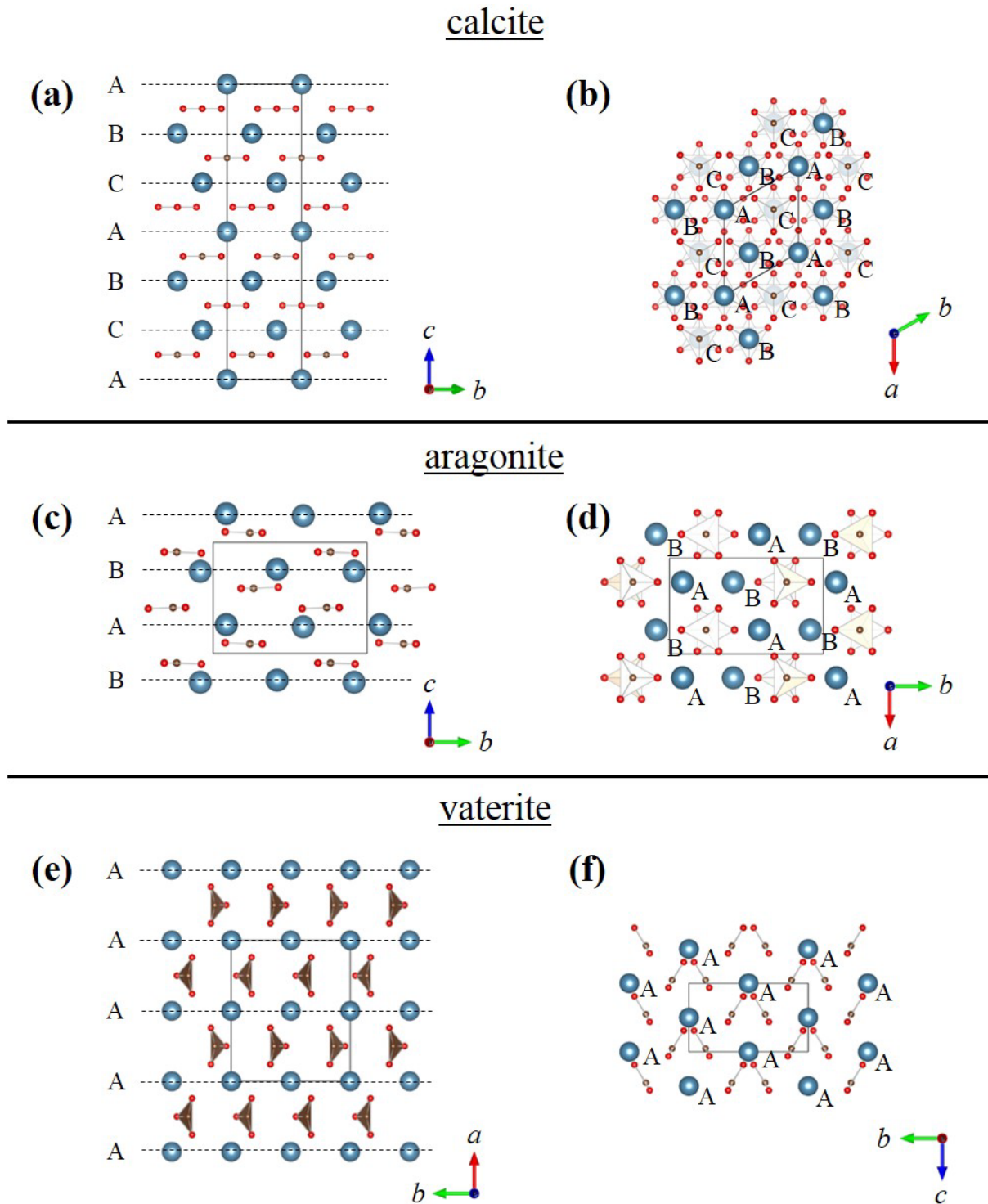


Figure 1–1. Crystal structures of anhydrous calcium carbonates: calcite from the  $a$ -axis **(a)** and  $c$ -axis **(b)**, trigonal structure ( $R\bar{3}c$ ) reported by Markgraf and Reeder (1985); aragonite from the  $a$ -axis **(c)** and  $c$ -axis **(d)**, orthorhombic structure ( $Pmcn$ ) reported by De Villiers (1971); vaterite from the  $c$ -axis **(e)** and  $a$ -axis **(f)**, which is one of structure models of vaterite (orthorhombic  $Ama2$ ) proposed by Le Bail et al. (2011). Blue, brown, and red spheres respectively indicate Ca, C, and O atoms. Rectangles and a rhombus represent unit cells of these crystal structures.

## *Chapter 1. General introduction of calcium carbonate*

Calcite is the most thermodynamically stable phase at ambient pressure and temperature, and is a major carbonate phase on the surface of the Earth. On the other hand, aragonite is thermodynamically stable at high pressure. However, aragonite can form at the ambient condition in the presence of  $\text{Mg}^{2+}$  and organic additives (Park et al., 2008). Calcite and aragonite are often found in biominerals, for example, the prismatic layer of shells and sea urchins formed by calcite, and the nacreous layer of shells and corals formed by aragonite. Impurity elements with ionic radii larger than that of  $\text{Ca}^{2+}$ , such as  $\text{Sr}^{2+}$ ,  $\text{Ba}^{2+}$ , and  $\text{Pb}^{2+}$ , tend to be captured in the crystal structure of aragonite (Faust, 1950; Wray and Daniels, 1957).

Vaterite is a metastable phase in all  $P$ - $T$  regions, and is much rare as a natural product compared to calcite and aragonite. Several studies reported occurrence of vaterite as biominerals in freshwater cultured pearls (Wehrmeister et al., 2010), in coho salmon otoliths (Gauldie et al., 1997), and in freshwater snail shell (Hasse et al., 2000). Abiogenic vaterite is found as a minor component of rocks (Wehrmeister et al., 2010), as Portland cement (Cole and Kroone, 1959), and as Pesyanoe meteorite (DuFresne and Edward, 1962). In laboratory experiments, vaterite is easily obtained from a supersaturated solution, but transforms into calcite or aragonite within a short period of time (Ogino et al., 1987). The crystal structure of vaterite has been controversial for almost a century because it is difficult to obtain large and pure single crystals.

After the observations of hydrous phases of calcium carbonate based on laboratory experiments (Johnston et al., 1916; Krauss and Schrieffer, 1930), natural minerals of both monohydrocalcite and ikaite were reported by Sapozhnikov and Tsvetkov (1959) and Pauly (1963), respectively. The formation of monohydrocalcite requires  $\text{Mg}^{2+}$  in the mother solution (Dejehet et al., 1999; Nishiyama et al., 2013). Monohydrocalcite is a metastable phase, and transforms to aragonite in an aqueous solution (Munemoto and Fukushi, 2008). Ikaite is also metastable at ambient pressure and temperature, and transforms to calcite, aragonite, vaterite and/or monohydrocalcite (Krauss and Schrieffer, 1930; Ito, 1998; Ito et al., 1999). However, ikaite forms in cold environments and/or under high pressure, and is stable with respect to calcite and aragonite at 25 °C and at 0.6–0.7 GPa (Marland, 1975).

### 1.3. Pressure responses of calcium carbonate

Many studies have investigated the high-pressure behavior of calcite and aragonite, but details of the phase transformations remain controversial. To date, three high-pressure phases of calcite at ambient temperature have been reported. These phases are described as the term of “calcite X” or “CaCO<sub>3</sub> X” (X = I, II, III, and VI, including ambient phase of calcite). In this thesis, the former term is used for the description of these phases. Figure 1–2 shows *P–T* diagram of CaCO<sub>3</sub> system produced by previous studies.

At ambient temperature, calcite I transforms to calcite II at about 1.5 GPa and to calcite III at 1.8–2.5 GPa (Bridgman, 1939; Liu and Mernagh, 1990; Suito et al., 2001; Merlini et al., 2012). Merlini et al. (2014) represented that calcite II can be described as a distortion of calcite I, and calcite III has different arrangements of carbonate units (see Figure 1–3). Calcite II and III are regarded as metastable phases, because the densities of these polymorphs are lower than that of aragonite (Merlini et al., 2012). In fact, calcite III transformed to aragonite by heating (Suito et al., 2001). Further compression beyond 15 GPa at 25 °C induces transformation from calcite III to calcite VI, which has density higher than that of aragonite. Calcite VI was reported as stable up to 40 GPa. It can replace aragonite in the Earth’s mantle (Merlini et al., 2012).

The transformation of aragonite has been investigated at higher pressures. Santillán and Williams (2004) reported that a pressure-induced phase transition from aragonite to a trigonal structure at 300 K occurred at about 50 GPa. They suggested that the trigonal form of CaCO<sub>3</sub> can exist within the lower mantle. Ono et al. (2005) reported the phase transition to a post-aragonite phase with an orthorhombic structure at about 40 GPa by heating to 1500–2000 K. Ono et al. (2005) concluded that the inconsistency between the two studies resulted from differences in the experimental temperature conditions.

Marland (1975) described the *P–T* diagram of the water-saturated CaCO<sub>3</sub> system, and presented the stability region of ikaite, which was found at low temperature and high pressure condition. On the other hand, no report in the relevant literature has described the high-pressure behavior of vaterite and monohydrocalcite, which are also metastable and rare as a natural product. This is probably due to little relationship between these phases and pressure in nature.

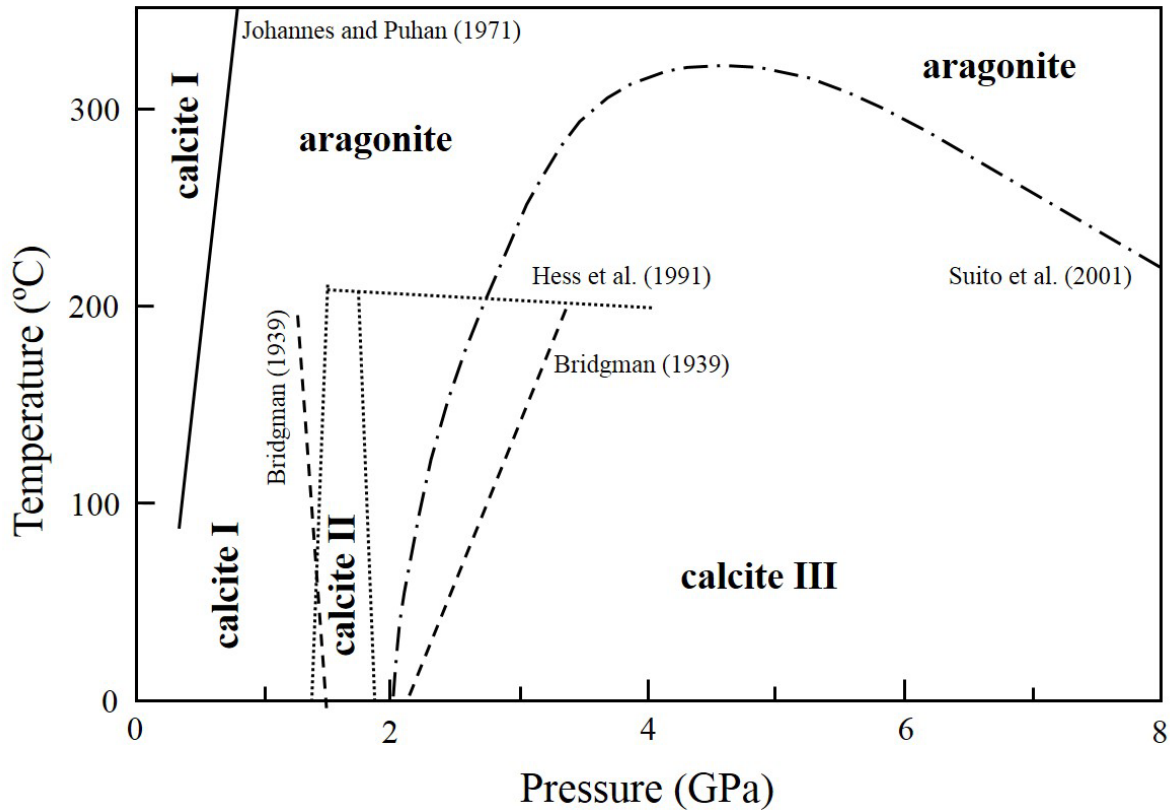


Figure 1–2.  $P$ - $T$  diagram of  $\text{CaCO}_3$  system, modified from Suito et al. (2001). The phase boundary between calcite I and aragonite reported by Johannes and Puhan (1971) is added in this figure.

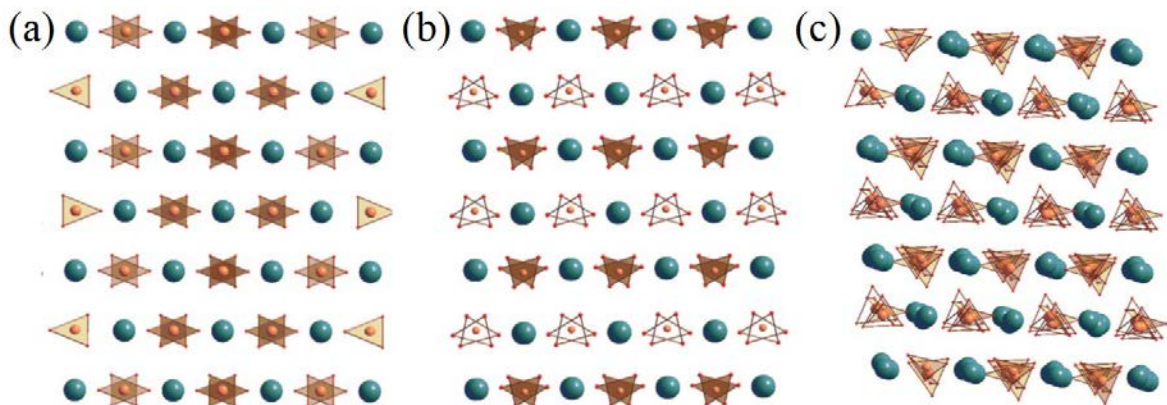


Figure 1–3. Schematic structures of (a) calcite I, (b) calcite II (monoclinic  $P2_1/c$ ), and (c) calcite III (triclinic  $P\bar{1}$ ) viewed along corresponding crystallographic directions:  $[\bar{2} \ 2 \ \bar{1}]$  for calcite I,  $c$ -axis for calcite II, and  $[4 \ 2 \ \bar{2}]$  for calcite III (Merlini et al., 2014). Blue, orange, and red spheres respectively indicate Ca, C, and O atoms.

## 1.4. Amorphous calcium carbonate (ACC)

Amorphous calcium carbonate (ACC) is described as a chemical formula of  $\text{CaCO}_3 \cdot x\text{H}_2\text{O}$  ( $x \leq \sim 1.5$ ) with variable water contents. In this thesis, water contents of ACC is presented by not “ $n$ ”, which is generally used for describing water contents of ACC, but “ $x$ ” because the term of “ $n$ ” is used as Avrami component in Chapter 3. ACC is the most metastable phase of calcium carbonate with the highest solubility (see Table 1–1; Brečević and Nielsen, 1989). Radha et al. (2010) indicated that the energetic sequence of increasing stability was described as follows: more metastable hydrated ACC  $\rightarrow$  less metastable hydrated ACC  $\rightarrow$  anhydrous ACC  $\rightarrow$  vaterite  $\rightarrow$  aragonite  $\rightarrow$  calcite.

In a laboratory, ACC is easily obtained from a highly supersaturated solution as an intermediate phase. Several synthesis methods have been reported, and the formation of ACC by mixing  $\text{CaCl}_2$  and  $\text{Na}_2\text{CO}_3$  solutions is the most common method (Ogino et al., 1987; Kojima et al., 1993; Koga et al., 1998; Rodriguez-Blanco et al., 2008). Synthetic ACC often exhibits spherical shape with a diameter smaller than  $1.2 \mu\text{m}$  (see Figure 1–4; Gorna et al., 2008). Gebauer et al. (2008) suggested that two types of ACC, ACC I and ACC II, were obtained using solutions with different pH conditions (pH = 9.00–9.50 and 9.75–10.0). After the report, they analyzed these ACCs using NMR and Ca  $K$ -edge EXAFS, and identified ACC I and ACC II as proto-calcite ACC and proto-vaterite ACC, respectively (Gebauer et al., 2010).

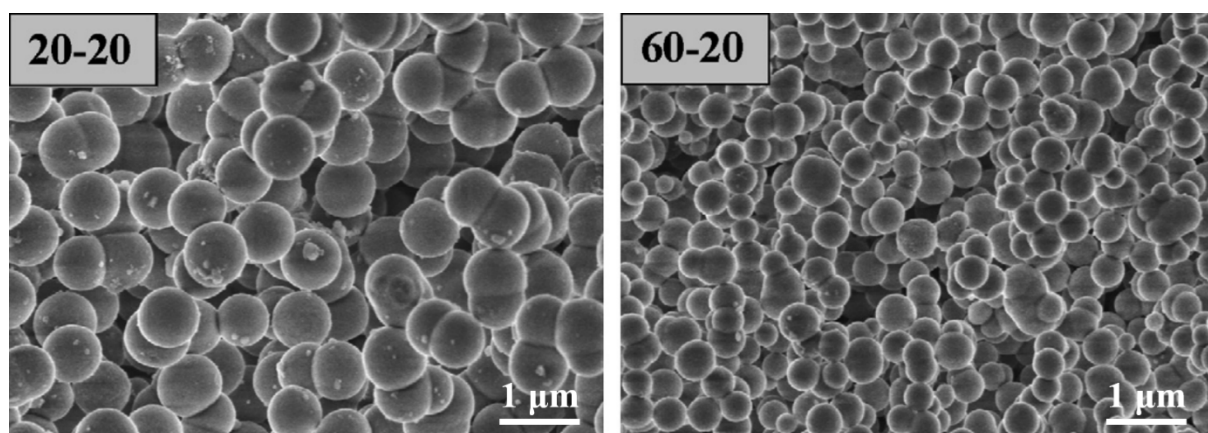


Figure 1–4. SEM images of ACC particles synthesized from 20 mM (left) and 60 mM (right) of  $\text{CaCl}_2$  with equimolar dimethyl carbonate and 20 mM NaOH (rescaled from Gorna et al., 2008).

## *Chapter 1. General introduction of calcium carbonate*

In nature, ACC exists in biominerals. There are two types of biogenic ACC: stable ACC and transient ACC (Addadi et al., 2003). Stable ACC is used as a temporary storage of calcium because of its high solubility or as a stiffener for exoskeletons owing to lack of cleavage planes. Crustaceans use stable ACC due to their molting-mineralization cycles, which require intensive mineral mobilization and storage. This type of ACC is prevented from crystallization by some kind of materials such as phosphate-containing molecules (Bentov et al., 2010; Sato et al., 2011), and magnesium ion (Raz et al., 2000; Addadi et al., 2003; Tao et al., 2009). On the other hand, transient ACC functions as a precursor phase of calcium carbonate crystals by utilizing its isotropic structure. For example, Politi et al. (2004) reported that ACC formed at the edge of sea urchin spines as a precursor phase of single crystal calcite during regeneration. Sponge spicules also consist of calcite via ACC precursor (Gilis et al., 2011). In biomineralization, deposition of transient ACC is a strategy for the formation of single crystals with complex texture.

ACC has unique optical and mechanical properties: optical isotropy and lack of cleavage planes (Aizenberg et al., 2002; Oaki et al., 2008; Bentov et al., 2010). Recently, some studies on the innovation of new materials using ACC were reported by mimicking biominerals (Oaki et al., 2008; Maruyama et al., 2011). As mentioned above, ACC is metastable in aqueous solutions or humid condition, and then the stabilization of ACC requires the presence of additives that prevent it from crystallization. Oaki et al. (2008) reported a glass-like material consisting of ACC and poly(acrylic acid) (PAA). The amorphous composites were obtained by adding 0.1 M Na<sub>2</sub>CO<sub>3</sub> into a solution containing 0.1 M CaCl<sub>2</sub> and 0.1 M PAA, and by drying at room temperature. They suggested that ACC is stabilized by the formation of nanosegregated structures. Maruyama et al. (2011) reported that a composite material of ACC and aspartic acid (Asp), which is a small molecule, was synthesized by CO<sub>2</sub>-gas bubbling into calcium aspartate solution. This report indicated that Asp can also stabilize ACC, suggesting intermolecular interaction between ACC and Asp.

## **1.5. Crystallization from ACC**

As described above, single crystals of calcium carbonate with complex texture are formed via ACC precursor in biomineralization. Therefore, the crystallization from ACC is an important process for biomineralization. Tao et al. (2009) reported that magnesium-aspartate-rich compound deeply involved in crystallization process of ACC. On the other hand, it is also important to understand the crystallization of ACC in inorganic process in order to understand the nature of calcium carbonate. Previous studies about the crystallization of ACC in inorganic system are described as below.

In an aqueous solution, ACC transforms to calcite, aragonite and/or vaterite depending on the physical and chemical conditions. Ogino et al. (1987) reported that ACC transformed to calcite and vaterite at 10–30 °C, and to calcite and aragonite at 60–80 °C. At intermediate temperatures (40–50 °C), the formation of all three polymorphs was observed. Aragonite and vaterite, which are metastable phases at ambient pressure and temperature, gradually transformed to the most stable form, calcite. Rodriguez-Blanco et al. (2011) reported time-resolved observation of the transformation from ACC to crystalline phases at a range of environmentally relevant temperatures (7.5–25 °C) using energy-dispersive X-ray diffraction (ED-XRD) method. They suggested that ACC crystallized in two stages: rapid dehydration from ACC and crystallization to vaterite, and the transformation from vaterite to calcite by a dissolution and reprecipitation mechanism. Bots et al. (2012) also reported the transformation from ACC to calcite via vaterite using small- and wide-angle X-ray scattering (SAXS/WAXS) with a high time resolution in the order of seconds. They suggested three stages in the crystallization from ACC to vaterite: spherulitic growth, dissolution and reprecipitation, and Ostwald ripening (see Figure 1–5).

Nielsen et al. (2014) conducted in situ transmission electron microscopy (TEM) observations on nucleation of calcium carbonate from supersaturated solutions with several concentrations. They suggested that multiple nucleation pathways, which are direct formation from solution and indirect transformation via metastable precursors, occurred. However, direct transformation from ACC to calcite was not observed in their experiments.

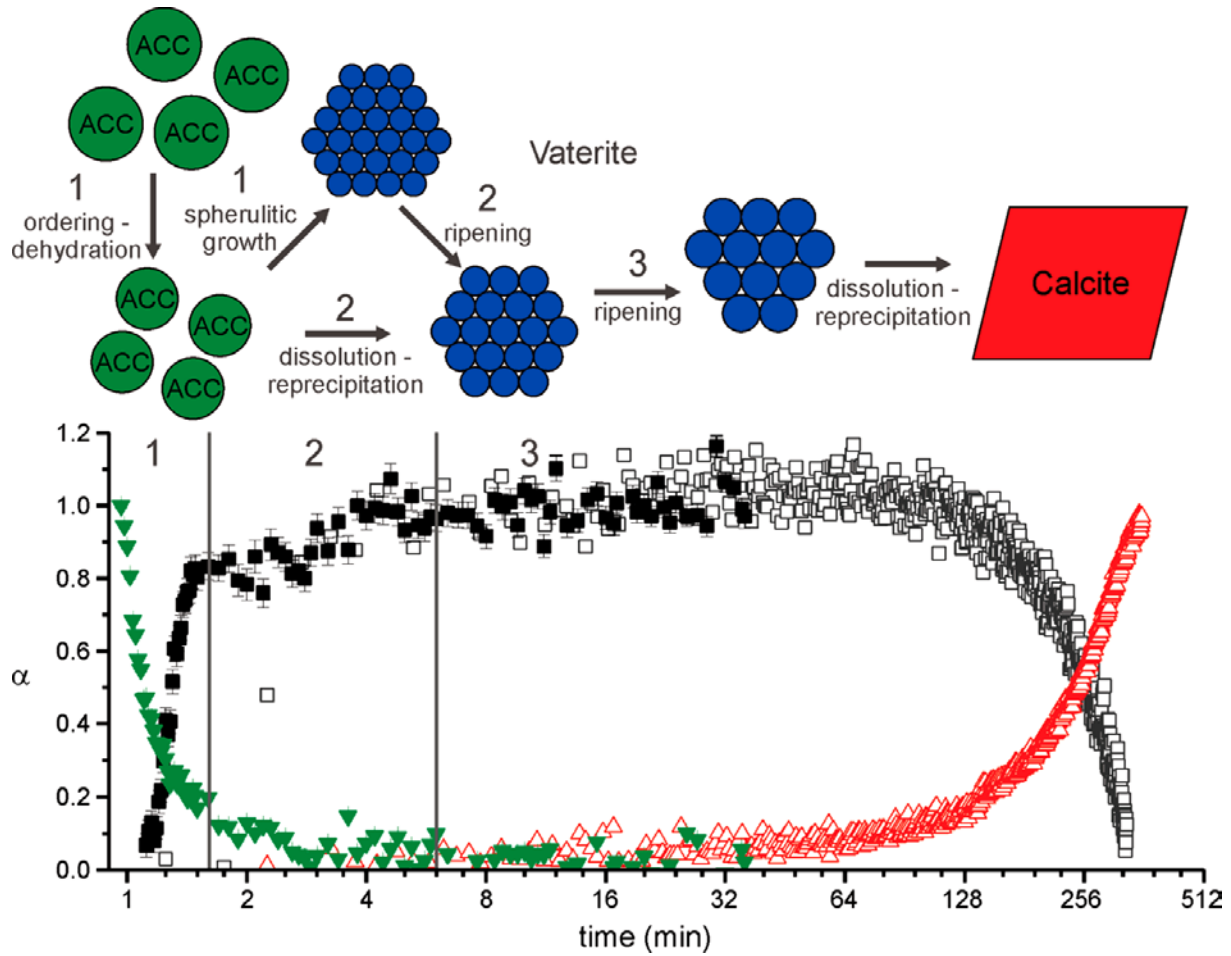


Figure 1–5. Schematic representation of the multistage crystallization pathway (top) with the underlying combined reaction progress  $\alpha$  for the full crystallization reaction in the pure ACC system (Bots et al., 2012). Green triangles and full black squares show ACC and vaterite from their study, and open squares and red triangles show vaterite and calcite from Rodriguez-Blanco et al. (2011).

## Chapter 1. General introduction of calcium carbonate

Crystallization of ACC also occurs by heating treatments. Kojima et al. (1993) and Koga et al. (1998) reported the crystallization from ACC by heating. The dehydration from ACC gradually occurred until about 300 °C, and then the anhydrous ACC crystallized to calcite at dry condition at about 350 °C (see Figure 1–6). Aragonite and vaterite respectively transform to calcite at 455 °C (Wolf and Günther, 2001) and at 370–490 °C depending on the way of sample preparation and measurement conditions (Rao, 1973; Maciejewski et al., 1994; Baitalow et al., 1998; Wolf and Günther, 2001). ACC has a distinct thermal stability field compared with anhydrous crystalline phases.

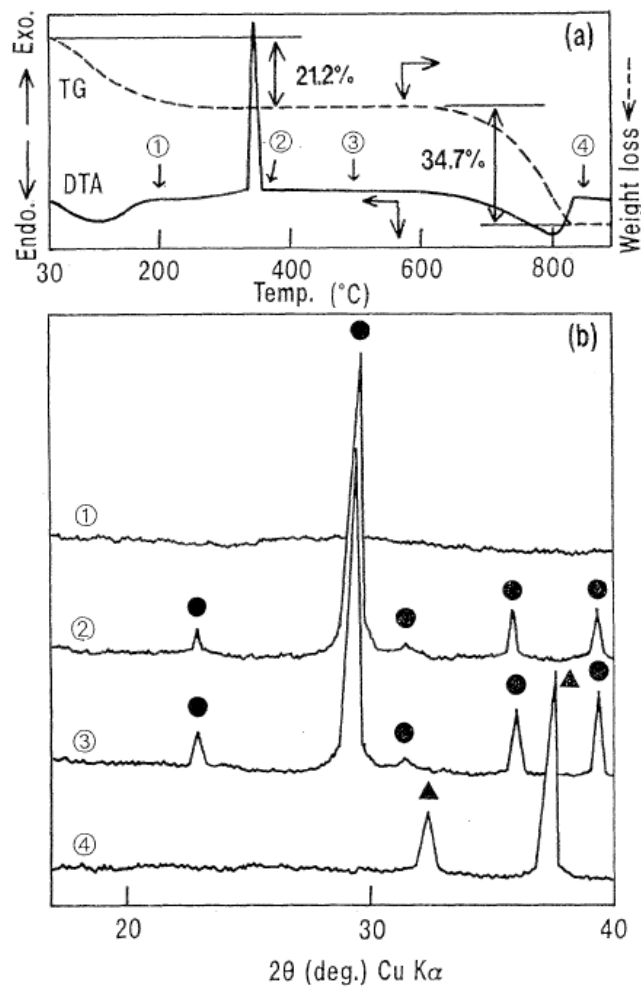


Figure 1–6. Thermal decomposition of ACC ( $\text{CaCO}_3 \cdot 1.5\text{H}_2\text{O}$ ) with heating. (a) TG–DTA curve at  $20\text{ }^\circ\text{C min}^{-1}$  of heating rate, and (b) X-ray diffraction patterns at temperatures (1) 200, (2) 370, (3) 500, (4) 850 °C: ●, calcite; and ▲, CaO (Kojima et al., 1993).

## *Chapter 1. General introduction of calcium carbonate*

Yoshino et al. (2012) presented a new crystallization process of ACC by applying pressure at room temperature. The pressure-induced crystallization phenomenon was observed by serendipity. At first, ACC was pressurized with seed crystals of calcite or aragonite in expectation of epitaxial growth of ACC. The molding using a pelleter was conducted to fill spaces between ACC powder and a seed crystal. However, the crystallization of ACC was observed without seed crystals.

The detail of pressure-induced crystallization of ACC is described in Chapter 2. Here, the obtained results are presented briefly. The crystallization of ACC occurred below 1 GPa, and stable calcite and metastable vaterite were observed in samples recovered from high pressure. The crystallized pressure increased with decreased H<sub>2</sub>O content of ACC. At the same pressure, ACC with higher H<sub>2</sub>O content had higher vaterite/calcite ratio than ACC with lower H<sub>2</sub>O content. Moreover, the dehydration from ACC occurred during the crystallization. These results indicate that H<sub>2</sub>O in ACC plays an important role in the crystallization process.

## **1.6. Purpose and contents of this study**

The pressure-induced crystallization from ACC to calcite and vaterite was reported by previous experiments. However, the crystallization mechanism is still unclear because of the observation based on recovered samples. Previous experiments resulted in the coexistence of thermodynamically stable calcite and metastable vaterite. It suggests two possibilities on the pathway of transformation to calcite in the phenomenon: direct transformation from ACC or indirect transformation via vaterite like the crystallization in a solution. Moreover, pressure responses of calcium carbonate polymorphs would provide useful information for the crystallization of ACC at high pressure. Many studies have reported the phase-transformation behavior of calcite and aragonite at high pressure. However, no report has presented the pressure response of vaterite. Therefore, to gain a better understanding of the pressure-induced crystallization from ACC to calcite and vaterite, it is important to perform in situ observation during crystallization of ACC and obtain information of pressure response of vaterite.

The present study mainly focuses on in situ observations on ACC and vaterite at high pressure to elucidate the mechanism of pressure-induced crystallization of ACC. This thesis consists of five chapters including introduction (Chapter 1) and conclusions (Chapter 5). The contents of Chapters 2–4 are described as below.

## *Chapter 1. General introduction of calcium carbonate*

In Chapter 2, I introduced details of pressure-induced crystallization of ACC using a tungsten-carbide pelleter. The identification of samples recovered from high pressure was conducted by powder X-ray diffraction measurements. In addition, basic properties of ACC used in this study are presented by thermal analysis, X-ray diffraction, infrared spectroscopy, and structural analysis.

In Chapter 3, in situ time-resolved X-ray diffraction studies were conducted to understand the mechanisms and kinetics of pressure-induced crystallization from ACC to calcite and vaterite. X-ray diffraction patterns of ACC during compression every 10 s were obtained by energy-dispersive X-ray diffraction method installed in a cubic-type multi-anvil apparatus. Moreover, SEM observations were also conducted to obtain more detail information of the crystallization mechanism. Raman mapping on the SEM images presented the relation between the texture and polymorphs. The possible mechanism of pressure-induced crystallization from ACC to calcite and vaterite are discussed.

In Chapter 4, the pressure responses of vaterite were investigated with powder X-ray diffraction and Raman spectroscopy under high pressure using diamond anvil cells (DACs). Several phase transitions from vaterite are described and this study suggests the existence of new high-pressure phases of calcium carbonate unreported previously.

## References

- Addadi L, Raz S, and Weiner S (2003) Taking Advantage of Disorder: Amorphous Calcium Carbonate and Its Roles in Biomineralization. *Advanced Materials*, **15**, 959–970.
- Aizenberg J, Lambert G, Weiner S, and Addadi L (2002) Factors Involved in the Formation of Amorphous and Crystalline Calcium Carbonate: A Study of an Ascidian Skeleton. *Journal of the American Chemical Society*, **124**, 32–39.
- Baitalow F, Wolf G, and Schmidt HG (1998) THERMOCHEMICAL INVESTIGATIONS OF CALCIUM CARBONATE PHASE TRANSITIONS I. Thermal activated vaterite–calcite transition. *Journal of Thermal Analysis*, **52**, 5–16.
- Bentov S, Weil S, Glazer L, Sagi A, and Berman A (2010) Stabilization of amorphous calcium carbonate by phosphate rich organic matrix proteins and by single phosphoamino acids. *Journal of Structural Biology*, **171**, 207–215.
- Bischoff JL, Fitzpatrick JA, and Rosenbauer RJ (1993) The Solubility and Stabilization of ikaite ( $\text{CaCO}_3 \cdot 6\text{H}_2\text{O}$ ) from 0° to 25°C: Environmental and Paleoclimatic Implications for Thinolite Tufa. *The Journal of Geology*, **101**, 21–33.
- Bots P, Benning LG, Rodriguez-Blanco JD, Roncal-Herrero T, and Shaw S (2012) Mechanistic Insights into the Crystallization of Amorphous Calcium Carbonate (ACC). *Crystal Growth & Design*, **12**, 3806–3814.
- Brečević L, and Nielsen AE (1989) SOLUBILITY OF AMORPHOUS CALCIUM CARBONATE. *Journal of Crystal Growth*, **98**, 504–510.
- Bridgman PW (1939) THE HIGH PRESSURE BEHAVIOR OF MISCELLANEOUS MINERALS. *American Journal of Science*, **237**, 7–18.
- Cole WF, and Kroone B (1959) Carbonate Minerals in Hydrated Portland Cement. *Nature*, **184**, B.A.57.
- Dejehet F, Idrissi S, and Debuyst R (1999) Magnesium and occluded water in calcium carbonate monohydrate. *Journal de Chimie Physique et de Physico-Chimie Biologique*, **96**, 741–753.
- Dal Negro A, and Ungaretti L (1971) REFINEMENT OF THE CRYSTAL STRUCTURE OF ARAGONITE. *The American Mineralogist*, **56**, 768–772.
- De Villiers JPR (1971) CRYSTAL STRUCTURES OF ARAGONITE, STRONTIANITE, AND WITHERITE. *The American Mineralogist*, **56**, 758–767.

## Chapter 1. General introduction of calcium carbonate

- DuFresne ER, and Edward A (1962) On the retention of primordial noble gases in the Pesyanoe meteorite. *Geochimica et Cosmochimica Acta*, **26**, 251–262.
- Faust GT (1950) THERMAL ANALYSIS STUDIES ON CARBONATES I. ARAGONITE AND CALCITE. *American Mineralogist*, **35**, 207–224.
- Gauldie RW, Sharma SK, and Volk E (1997) Micro-Raman Spectral Study of Vaterite and Aragonite Otoliths of the Coho Salmon, *Oncorhynchus kisutch*. *Comparative Biochemistry and Physiology*, **118**, 753–757.
- Gebauer D, Gunawidjaja PN, Ko JYP, Bacsik Z, Aziz B, Liu L, Hu Y, Bergström L, Tai CW, Sham TK, Edén M, and Hedin N (2010) Proto-Calcite and Proto-Vaterite in Amorphous Calcium Carbonates. *Angewandte Chemie*, **49**, 8889–8891.
- Gebauer D, Völkel A, and Cölfen H (2008) Stable Prenucleation Calcium Carbonate Clusters. *Science*, **322**, 1819–1822.
- Gilis M, Grauby O, Willenz P, Dubois P, Legras L, Heresanu V, and Baronnet A (2011) Multi-scale mineralogical characterization of the hypercalcified sponge *Petrobiona massiliana* (Calcarea, Calcaronea). *Journal of Structural Biology*, **176**, 315–329.
- Gorna K, Hund M, Vučak M, Gröhn F, and Wegner G (2008) Amorphous calcium carbonate in form of spherical nanosized particles and its application as fillers for polymers. *Materials Science and Engineering A*, **477**, 217–225.
- Hasse B, Ehrenberg H, Marxen JC, Becker W, and Epple M (2000) Calcium Carbonate Modifications in the Mineralized Shell of the Freshwater Snail *Biomphalaria glabrata*. *Chemistry a European Journal*, **6**, 3679–3685.
- Hess NJ, Exarhos GJ, and Ghose S (1991) RAMAN SPECTROSCOPY AT SIMULTANEOUS PRESSURE AND TEMPERATURE: PHASE RELATIONS AND LATTICE DYNAMICS OF  $\text{CaCO}_3$ . *Conference: 13. AIRAPT international conference on high pressure science and technology, Bangalore (India)*, 7–11.
- Hesse K-F, Küppers H, and Suess E (1983) Refinement of the structure of Ikaite,  $\text{CaCO}_3 \cdot 6\text{H}_2\text{O}$ . *Zeitschrift für Kristallographie*, **163**, 227–231.
- Ito T (1998) Factors controlling the transformation of natural ikaite from Shiowkka, Japan. *Geochemical Journal*, **32**, 267–273.
- Ito T, Matsubara S, and Miyawaki R (1999) Vaterite after ikaite in carbonate sediment. *Journal of Mineralogy, Petrology and Economic Geology*, **94**, 176–182.

## Chapter 1. General introduction of calcium carbonate

- Johannes W, and Puhan D (1971) The Calcite-Aragonite Transition, Reinvestigated. *Contributions to Mineralogy and Petrology*, **31**, 28–38.
- Johnston J, Merwin HE, and Williamson ED (1916) The Several Forms of Calcium Carbonate. *The American Journal of Science*, **41**, 473–512.
- Kamhi SR (1963) On the Structure of Vaterite, CaCO<sub>3</sub>. *Acta Crystallographica*, **16**, 770–772.
- Koga N, Nakagoe Y, and Tanaka H (1998) Crystallization of amorphous calcium carbonate. *Thermochimica Acta*, **318**, 239–244.
- Kojima Y, Kawanobe A, Yasue T, and Arai Y (1993) Synthesis of Amorphous Calcium Carbonate and Its Crystallization. *Journal of the Ceramic Society of Japan*, **101**, 1145–1152.
- Kralj D, and Brecevic L (1995) Dissolution kinetics and solubility of calcium carbonate monohydrate. *Colloids and Surfaces*, **96**, 287–293.
- Krauss F, and Schriever W (1930) Die Hydrate des Calciumcarbonats. *Zeitschrift für Anorganische und Allgemeine Chemie*, **188**, 259–273.
- Le Bail A, Ouhenia S, and Chateigner D (2011) Microtwinning hypothesis for a more ordered vaterite model. *Powder Diffraction*, **26**, 16–21.
- Liu LG, and Mernagh TP (1990) Phase transitions and Raman spectra of calcite at high pressures and room temperature. *American Mineralogist*, **75**, 801–806.
- Maciejewski M, Oswald HR, and Reller A (1994) Thermal transformations of vaterite and calcite. *Thermochimica Acta*, **234**, 315–328.
- Markgraf SA, and Reeder RJ (1985) High-temperature structure refinements of calcite and magnesite. *American Mineralogist*, **70**, 590–600.
- Marland G (1975) The stability of CaCO<sub>3</sub>·6H<sub>2</sub>O (ikaite). *Geochimica et Cosmochimica Acta*, **39**, 83–91.
- Maruyama K, Yoshino T, and Kagi H (2011) Synthesizing a composite material of amorphous calcium carbonate and aspartic acid. *Materials Letters*, **65**, 179–181.
- Merlini M, Crichton WA, Chantel J, Guignard J, and Poli S (2014) Evidence of interspersed co-existing CaCO<sub>3</sub>-III and CaCO<sub>3</sub>-IIIb structures in polycrystalline CaCO<sub>3</sub> at high pressure. *Mineralogical Magazine*, **78**, 225–233.
- Merlini M, Hanfland M, and Crichton WA (2012) CaCO<sub>3</sub>-III and CaCO<sub>3</sub>-VI, high-pressure polymorphs of calcite: Possible host structures for carbon in the Earth's mantle. *Earth and Planetary Science Letters*, **333–334**, 265–271.

## Chapter 1. General introduction of calcium carbonate

- Munemoto T, and Fukushi K (2008) Transformation kinetics of monohydrocalcite to aragonite in aqueous solutions. *Journal of Mineralogical and Petrological Sciences*, **103**, 345–349.
- Nielsen MH, Aloni S, and De Yoreo JJ (2014) In situ TEM imaging of CaCO<sub>3</sub> nucleation reveals coexistence of direct and indirect pathways. *Science*, **345**, 1158–1162.
- Nishiyama R, Munemoto T, and Fukushi K (2013) Formation condition of monohydrocalcite from CaCl<sub>2</sub>–MgCl<sub>2</sub>–Na<sub>2</sub>CO<sub>3</sub> solutions. *Geochimica et Cosmochimica Acta*, **100**, 217–231.
- Oaki Y, Kajiyama S, Nishimura T, Imai H, and Kato T (2008) Nanosegregated Amorphous Composites of Calcium Carbonate and an Organic Polymer. *Advanced Materials*, **20**, 3633–3637.
- Ogino T, Suzuki T, and Sawada K (1987) The formation and transformation mechanism of calcium carbonate in water. *Geochimica et Cosmochimica Acta*, **51**, 2757–2767.
- Ono S, Kikegawa T, Ohishi Y, and Tsuchiya J (2005) Post-aragonite phase transformation in CaCO<sub>3</sub> at 40 GPa. *American Mineralogist*, **90**, 667–671.
- Park WK, Ko S-J, Lee SW, Cho K-H, Ahn J-W, and Han C (2008) Effects of magnesium chloride and organic additives on the synthesis of aragonite precipitated calcium carbonate. *Journal of Crystal Growth*, **310**, 2593–2601.
- Pauly H (1963) “IKAITE”, A NEW MINERAL FROM GREENLAND. *Arctic*, **16**, 263–264.
- Plummer LN, and Busenberg E (1982) The solubilities of calcite, aragonite and vaterite in CO<sub>2</sub>–H<sub>2</sub>O solutions between 0 and 90°C, and an evaluation of the aqueous model for the system CaCO<sub>3</sub>–CO<sub>2</sub>–H<sub>2</sub>O. *Geochimica et Cosmochimica Acta*, **46**, 1011–1040.
- Politi Y, Arad T, Klein E, Weiner S, and Addadi L (2004) Sea Urchin Spine Calcite Forms via a Transient Amorphous Calcium Carbonate Phase. *Science*, **306**, 1161–1164.
- Radha AV, Forbes TZ, Killian CE, Gilbert PUPA, and Navrotsky A (2010) Transformation and crystallization energetics of synthetic and biogenic amorphous calcium carbonate. *Proceedings of the National Academy of Sciences of the United States of America*, **107**, 16438–16443.
- Rao MS (1973) Kinetics and Mechanism of the Transformation of Vaterite to Calcite. *Bulletin of the Chemical Society of Japan*, **46**, 1414–1417.
- Raz S, Weiner S, and Addadi L (2000) Formation of High-Magnesian Calcites via an Amorphous Precursor Phase: Possible Biological Implications. *Advanced Materials*, **12**, 38–42.
- Rodriguez-Blanco JD, Shaw S, and Benning LG (2008) How to make ‘stable’ ACC: protocol and preliminary structural characterization. *Mineralogical Magazine*, **72**, 283–286.
- Rodriguez-Blanco JD, Shaw S, and Benning LG (2011) The kinetics and mechanisms of amorphous

## Chapter 1. General introduction of calcium carbonate

- calcium carbonate (ACC) crystallization to calcite, *via* vaterite. *Nanoscale*, **3**, 265–271.
- Santillán J, and Williams Q (2004) A high pressure X-ray diffraction study of aragonite and the post-aragonite phase transition in CaCO<sub>3</sub>. *American Mineralogist*, **89**, 1348–1352.
- Sapozhnikov DG, and Tsvetkov AI (1959) Precipitation of hydrous calcium carbonate on the bottom of Lake Issyk-Kul. *Doklady Akademii Nauk SSSR*, **24**, 131–133.
- Sato A, Nagasaka S, Furihata K, Nagata S, Arai I, Saruwatari K, Kogure T, Sakuda S, and Nagasawa H (2011) Glycolytic intermediates induce amorphous calcium carbonate formation in crustaceans. *Nature Chemical Biology*, **7**, 197–199.
- Schiebel R (2002) Planktic foraminiferal sedimentation and the marine calcite budget. *Global Biogeochemical Cycles*, **16**, 13-1–21.
- Suito K, Namba J, Horikawa T, Taniguchi Y, Sakurai N, Kobayashi M, Onodera A, Shimomura O, and Kikegawa T (2001) Phase relations of CaCO<sub>3</sub> at high pressure and high temperature. *American Mineralogist*, **86**, 997–1002.
- Swainson IP (2008) The structure of monohydrocalcite and the phase composition of the beachrock deposits of Lake Butler and Lake Fellmongery, South Australia. *American Mineralogist*, **93**, 1014–1018.
- Tao J, Zhou D, Zhang Z, Xu X, and Tang R (2009) Magnesium-aspartate-based crystallization switch inspired from shell molt of crustacean. *Proceedings of the National Academy of Sciences of the United States of America*, **106**, 22096–22101.
- Yoshino T, Maruyama K, Kagi H, Nara M, and Kim JC (2012) Pressure-Induced Crystallization from Amorphous Calcium Carbonate. *Crystal Growth & Design*, **12**, 3357–3361.
- Wehrmeister U, Soldati AL, Jacob DE, Häger T, and Hofmeister W (2010) Raman spectroscopy of synthetic, geological and biological vaterite: a Raman spectroscopic study. *Journal of Raman Spectroscopy*, **41**, 193–201.
- Wolf G, and Günther C (2001) THERMOPHYSICAL INVESTIGATIONS OF THE POLYMORPHOUS PHASES OF CALCIUM CARBONATE. *Journal of Thermal Analysis and Calorimetry*, **65**, 687–698.
- Wray JL, and Daniels F (1957) Precipitation of Calcite and Aragonite. *Journal of the American Chemical Society*, **79**, 2031–2034.

## **Chapter 2.**

### **Basic properties of ACC: experimental identification and pressure response**

## **2.1. Introduction**

In biomineralization, single crystals of calcium carbonate with complex texture are formed via ACC precursor (Politi et al., 2004; Tao et al., 2009). The crystallization of ACC is an essential process to understand the formation mechanism of calcium carbonate biominerals. It is important to investigate organic molecules involved in the crystallization process of ACC. On the other hand, the crystallization of ACC in inorganic process is also important. There are previous studies reporting the crystallization of ACC in supersaturated solutions or by heating.

Ogino et al. (1987) reported that ACC transformed to calcite, aragonite, and/or vaterite depending on temperature and solution conditions in aqueous solutions. Time-resolved X-ray diffraction studies indicated that at room temperature and no additives, ACC rapidly crystallized to vaterite, and vaterite gradually transformed to calcite (Rodriguez-Blanco et al., 2011; Bots et al., 2012). Moreover, Nielsen et al. (2014) observed multiple nucleation pathways including direct formation from solution and indirect transformation via metastable phases by in situ transmission electron microscopy (TEM). On the other hand, ACC crystallizes to calcite via anhydrous ACC by heating treatments. The dehydration from ACC gradually occurred by heating until 300 °C, and then the anhydrous ACC crystallized to calcite at about 350 °C (Kojima et al., 1993; Koga et al., 1998).

Until recently, there is no report about the pressure response of ACC. However, the crystallization and the structural change of amorphous materials at high pressure have been reported extensively (He et al., 2002; Xu et al., 2010; Pandey et al., 2011; Sato and Funamori, 2008). For example, Xu et al. (2010) indicated pressure-induced crystallization of amorphous  $\text{Ge}_2\text{Sb}_2\text{Te}_5$  at 28 GPa at room temperature. It is expected that ACC also crystallizes by applied pressure. In this chapter, high-pressure experiments on ACC based on the recovered samples are presented to investigate the pressure response of ACC, which is detail of Yoshino et al. (2012). In addition, it is also described the basic properties of ACC used in this study by thermal analysis, X-ray diffraction, infrared spectroscopy, and structural analysis.

## **2.2. Experimental procedures**

### **2.2.1. Synthesis of ACC**

Powder ACC samples were synthesized from an aqueous system of  $\text{CaCl}_2\text{-Na}_2\text{CO}_3$  (Kojima et al., 1993; Koga et al., 1998). Aqueous solutions were prepared using Milli-Q water ( $> 18.2 \Omega\cdot\text{m}$ ). Powder reagents of  $\text{CaCl}_2\cdot 2\text{H}_2\text{O}$  and  $\text{Na}_2\text{CO}_3$  were purchased from Wako Pure Chemical Industries Ltd.

First, two aqueous solutions,  $\text{CaCl}_2$  (0.1 M) and  $\text{Na}_2\text{CO}_3$  (0.1 M), were prepared and kept at about  $0^\circ\text{C}$ . Ten milliliter of these chilled solutions were mixed, and then filtered immediately using an aspirator and a membrane filter with a pore size of  $0.45 \mu\text{m}$ . The precipitates were washed twice with 10 mL of acetone to remove water and dried in vacuum condition using a diaphragm pump for one day.

### **2.2.2. Control of water contents in ACC**

To investigate the dependence of pressure response of ACC on its water contents, ACC samples with less water contents were prepared by changing vacuum condition. In addition to a diaphragm pump (about  $10^2 \text{ Pa}$ ), vacuum treatment using a turbomolecular pump (about  $10^{-3} \text{ Pa}$ ) was further applied. The additional vacuum treatments were conducted under various time durations, 0.5, 1, 5, and 37 days.

### **2.2.3. Thermal analysis**

Water contents of ACC samples were estimated from weight loss in TG curves. Thermogravimetry–differential thermal analysis (TG–DTA) measurements were conducted using a thermal analysis instrument (TG-8120; Rigaku Corp.). About 10 mg of powdered ACC samples were weighed into a platinum crucible (5 mm diameter and 2.5 mm height). As a reference, alumina powder was used. Heating rate was  $10 \text{ K min}^{-1}$  at temperatures from room temperature to  $1000^\circ\text{C}$ . Measurements were performed under  $\text{N}_2$  gas flow ( $130 \text{ mL min}^{-1}$ ).

#### **2.2.4. Powder X-ray diffraction**

Angler-dispersive X-ray diffraction (XRD) patterns of powdered samples were obtained using an X-ray diffractometer (Miniflex II; Rigaku Corp.) with  $\text{CuK}\alpha$  radiation. XRD measurements were performed at  $2\theta$  of  $10\text{--}70^\circ$  at a scan rate of  $1^\circ \text{ min}^{-1}$  or  $20\text{--}60^\circ$  at a scan rate of  $5^\circ \text{ min}^{-1}$  using a zero background plate made of single crystal of silicon at room temperature.

#### **2.2.5. Infrared spectroscopy**

Infrared (IR) absorption spectra of powdered samples were obtained using the KBr-pellet method and the attenuated total reflection (ATR) method.

Measurements on the KBr-pellet method were carried out using an FT-IR spectrometer (Spectrum 2000; PerkinElmer Inc.). Powdered samples were ground and molded to pellets with KBr powder using a hand press. Measurements were conducted in the range of  $7800\text{--}370 \text{ cm}^{-1}$  at room temperature. Nitrogen gas was filled in a sample room. One IR spectrum was obtained from the average of data from 100 scans for normal measurements or from 20 scans for time-resolved measurements.

ATR measurements were conducted using another FT-IR spectrometer (Spectrum One; PerkinElmer Inc.) at room temperature. Powdered samples were mounted on a diamond/ZnSe crystal plate and were held by the force gauge of 1. Data from 20 scans at the range of  $4000\text{--}650 \text{ cm}^{-1}$  were averaged to one spectrum.

### 2.2.6. Structural analysis

Structural analysis was conducted using pair distribution function (PDF) analysis. High-energy X-ray diffraction measurements were carried out using a synchrotron radiation source at the AR–NW10A beamline of Photon Factory–Advanced Ring (PF–AR), High Energy Accelerator Research Organization (KEK), Japan (Figure 2–1). Powder sample of ACC ( $\text{CaCO}_3 \cdot 1.5\text{H}_2\text{O}$ ), filled into holders with 0.5 mm or 2 mm in thickness and sandwiched between two Kapton films with 20  $\mu\text{m}$  in thickness, was used for X-ray diffraction measurements (Figure 2–2 (a)). The incident X-ray energy was monochromated at 35 keV by a Si (311) double-crystal monochromator and diffraction data were collected in an asymmetrical (sample holder was fixed 90° to the incident beam) transmission mode (Figure 2–2 (b)).

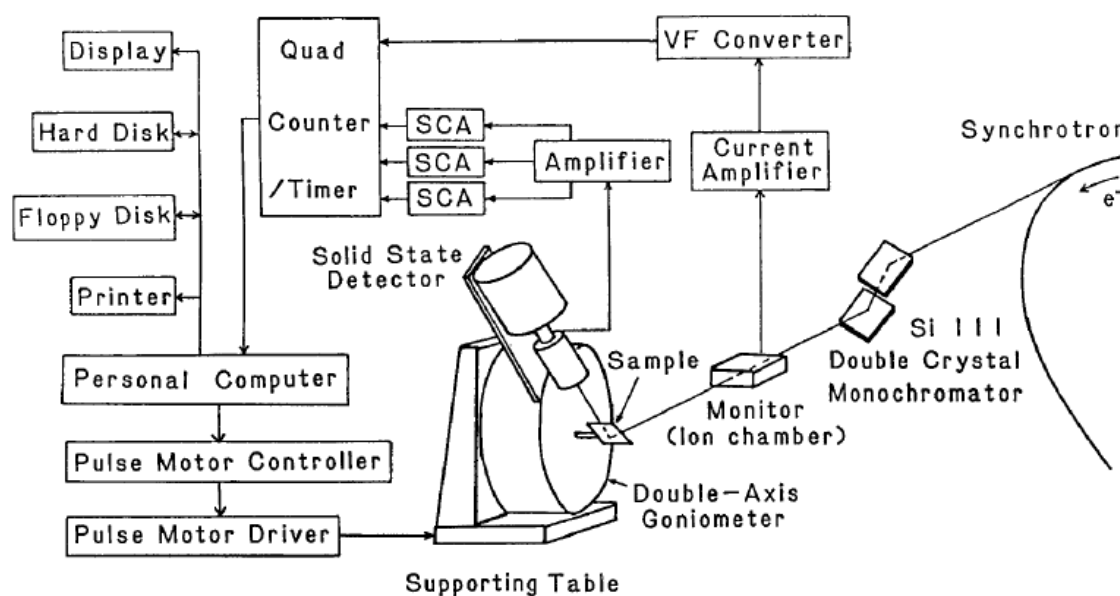


Figure 2–1. Schematic diagram of the facility for X-ray diffraction experiments at synchrotron beamline of Photon Factory (Waseda et al., 1988).

## Chapter 2. Basic properties of ACC

Observed X-ray scattering intensity was corrected for absorption and, subsequently, converted to electron unit per atom (Wagner et al., 1965). The Compton scattering effect was corrected by using the theoretical values for a free atom with the so-called Breit–Dirac recoil factor (Cromer and Mann, 1967). The atomic scattering factors used in this thesis were taken from *International Tables for X-ray Crystallography* (Ibers and Hamilton, 1974).

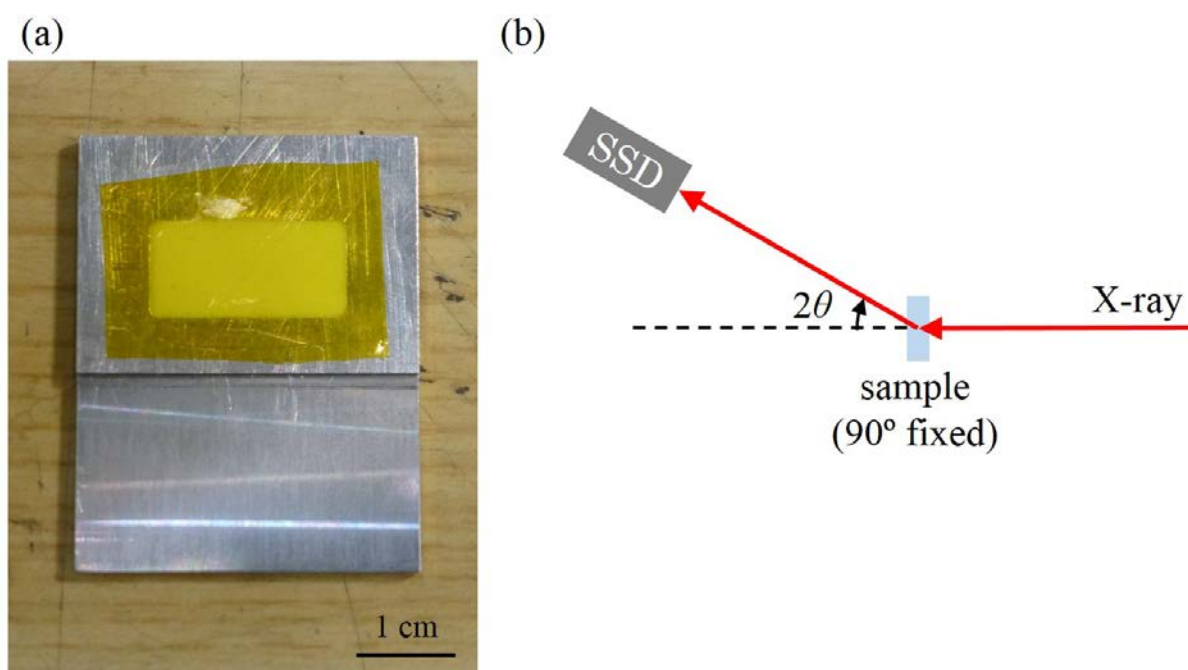


Figure 2–2. **(a)** Photograph of a sample holder. ACC powder sample was filled in the holder and kept to 2 mm of thickness between two Kapton films. **(b)** Schematic diagram of asymmetric transition mode for high-energy X-ray diffraction measurements.

### 2.2.7. Setup for high-pressure experiments

High pressure was generated using a hydraulic press (Figure 2–3). Ten milligrams of powder ACC samples were loaded in a tungsten-carbide (WC) pelleter with 4 mm inner diameter (Figure 2–4). The samples were pressurized for 10 min at pressure range of 0.08 to 0.8 GPa estimated from the load of the pressure and the area of piston. After decompression, all recovered samples were dried at vacuum condition using a diaphragm pump, because some samples were soaked with fluid dehydrated from ACC. All high-pressure experiments were conducted at room temperature. After vacuum drying, the polymorphs existed in the samples recovered from high pressure were investigated by XRD measurements.



Figure 2–3. Photograph of hydraulic press.

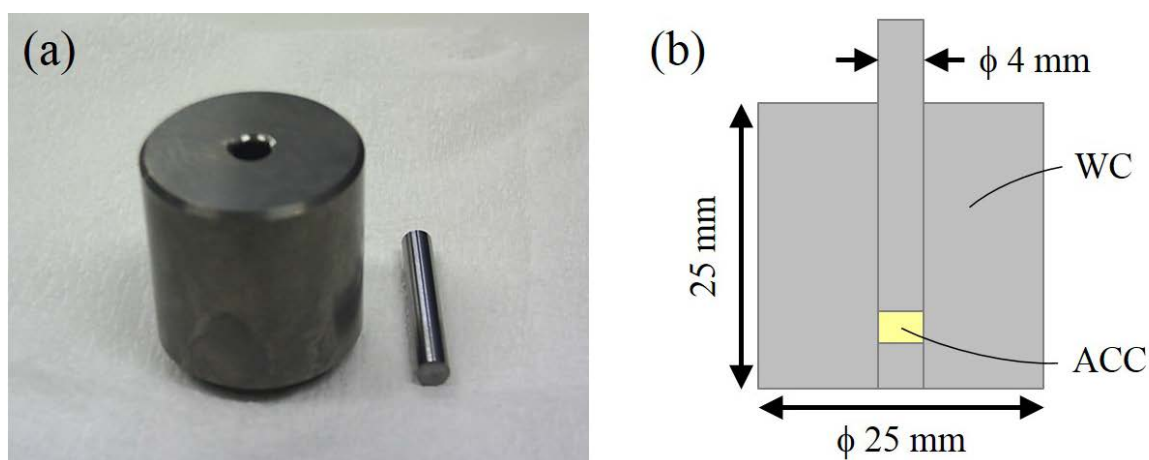


Figure 2–4. Photograph (a) and cross section (b) of the pelleter made of tungsten carbide.

## 2.3. Results and discussion

### 2.3.1. Basic properties of ACC

#### 2.3.1.1. Thermal analysis

Figure 2–5 shows TG curve of typical ACC synthesized from a supersaturated solution. Two apparent weight losses were observed in the curve. The first one up to 250 °C is assigned to the dehydration loss. Water contents ( $x$  value) of ACC were determined from the first weight loss.

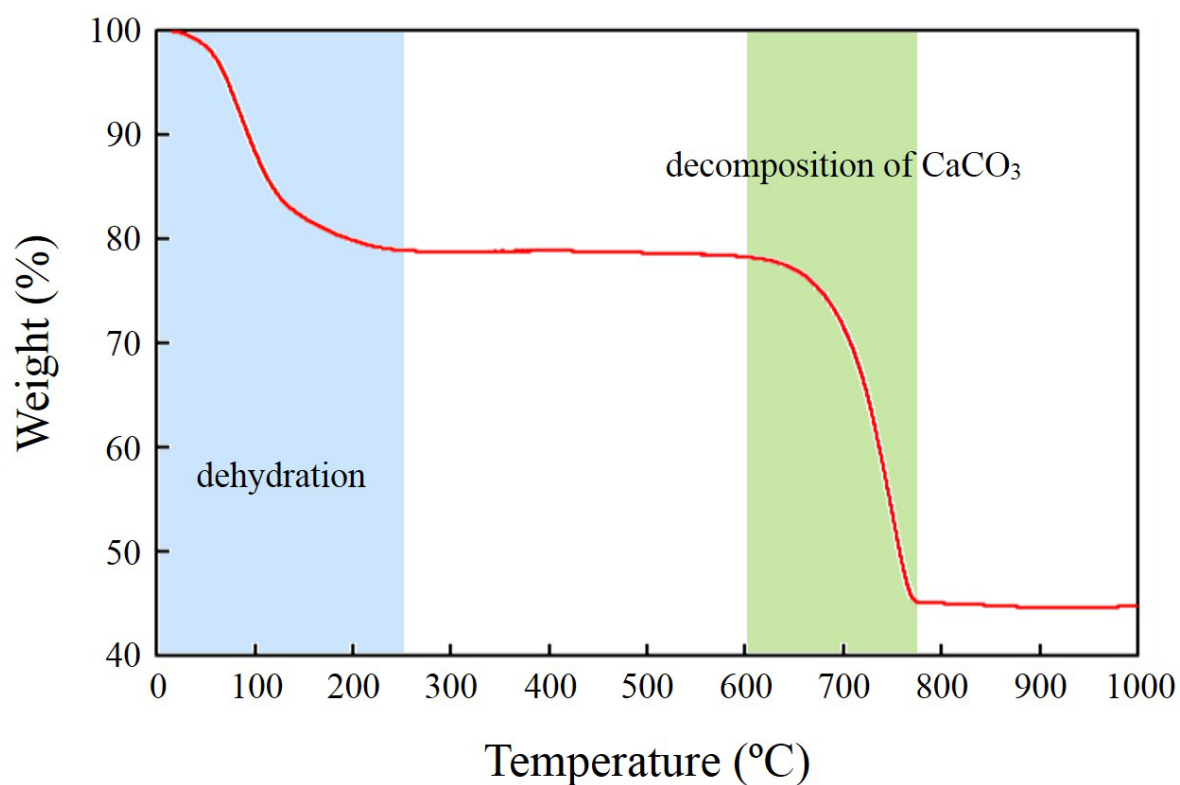


Figure 2–5. TG curve of synthesized ACC. First weight loss (up to about 250 °C; blue-shaded region) is attributable to the dehydration from ACC. Second weight loss (about 600 to 770 °C; green-shaded region) is explainable to decomposition of CaCO<sub>3</sub>.

## Chapter 2. Basic properties of ACC

Figure 2–6 shows water contents of ACCs ( $\text{CaCO}_3 \cdot x\text{H}_2\text{O}$ ) after various vacuum treatments. Water content of ACC for starting material was 1.5 as  $x$  value. This  $x$  value is consistent with previous reports (Kojima et al., 1993; Koga et al., 1998). Water contents decreased with evacuation time. ACCs after vacuum treatment using a turbo-molecular pump have lower water contents than that using a diaphragm pump. This result indicates that ACCs with various water contents could be prepared by additional evacuation treatments.

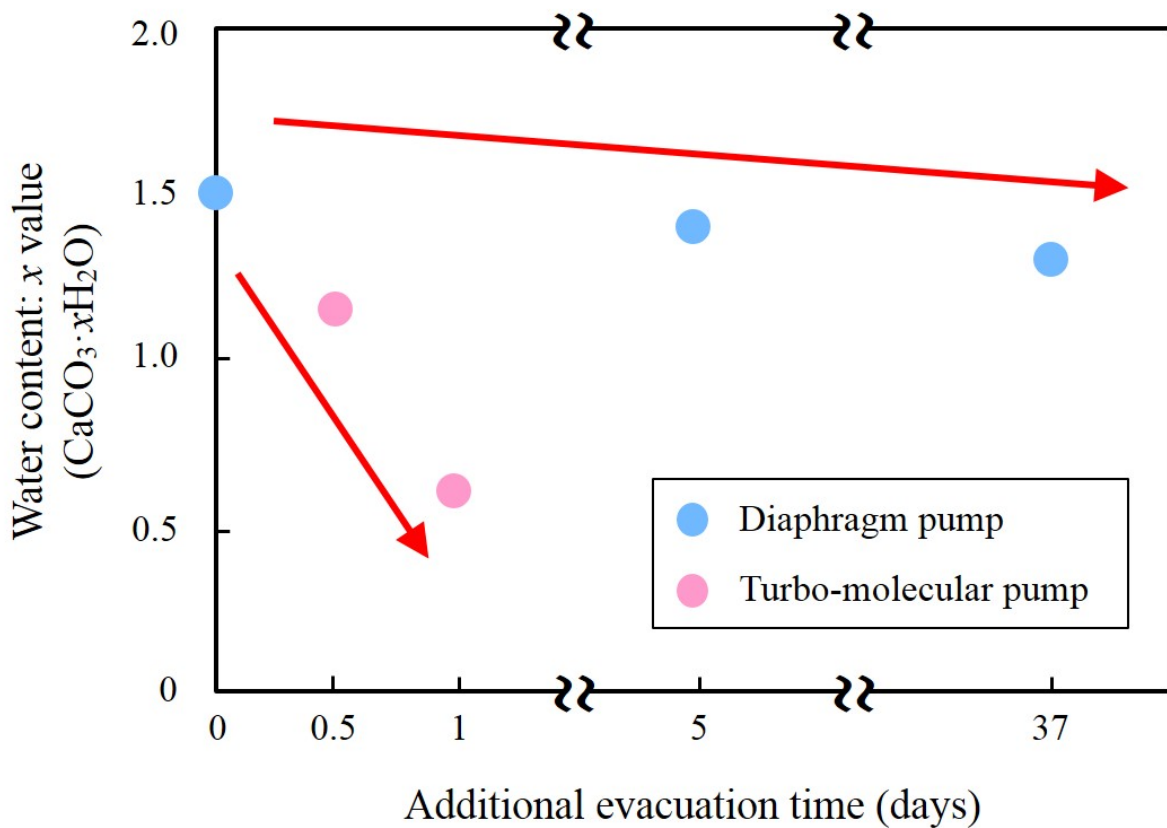


Figure 2–6. Relation between water contents ( $x$  value) of ACC and vacuum treatments.

## *Chapter 2. Basic properties of ACC*

In general, weight loss occurring up to 100 °C in TG curve is explainable by dehydration of absorbed water. However, weight loss from ACC occurred continuously up to about 250 °C. Kojima et al. (1993) reported that absorbed water and structural water of ACC could not be separated from each other by TG analysis with slow heating rate. In this study, the differential TG (DTG) was obtained from the experimental data (Figure 2-7). The DTG curve of ACC could be fitted by two peaks at about 90 °C and 170 °C. Figure 2-8 shows DTG curves of ACC samples with different water contents. The first peak at about 90 °C was selectively-weakened with lower water contents. This result suggests that two types of H<sub>2</sub>O exists in ACCs; the first peak at about 90 °C is attributable to weakly-bound H<sub>2</sub>O like adsorbed water and the second one at about 170 °C is assigned to tightly-bound H<sub>2</sub>O like structural water. This suggestion is consistent with the most recent study by Ihli et al. (2014). They also reported that ACC has two types of water existing in distinct environments by thermal analyses and solid-state nuclear magnetic resonance measurements.

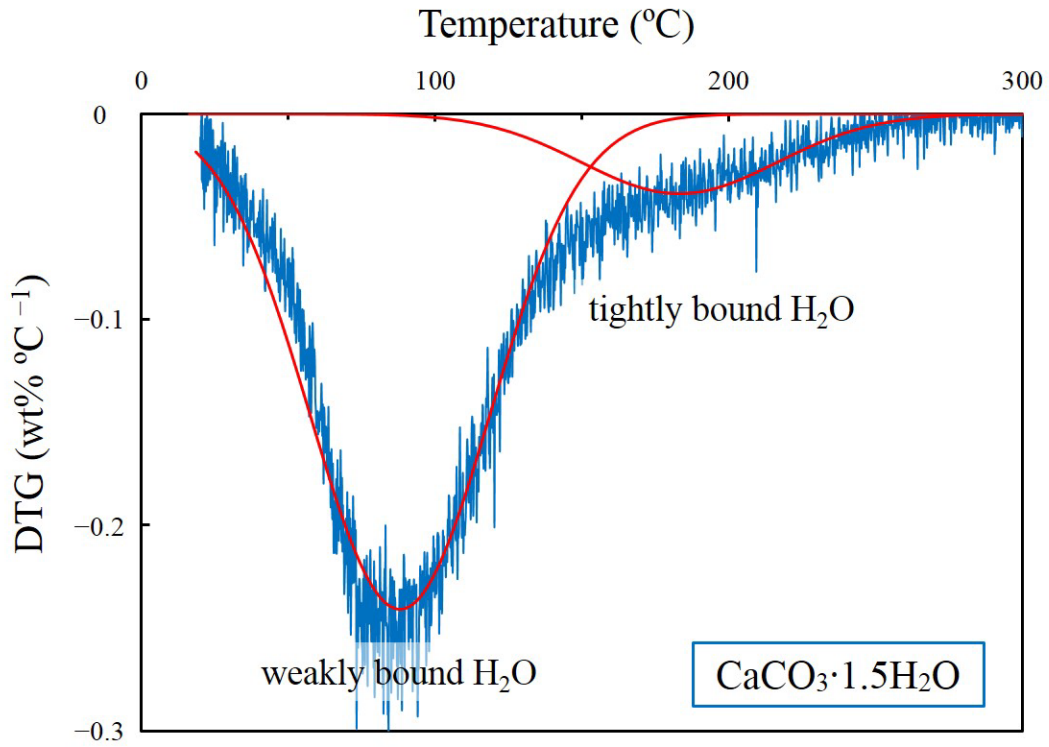


Figure 2–7. Differential TG (DTG) curve of synthesized ACC (blue line) and the obtained curves from peak fitting (red lines).

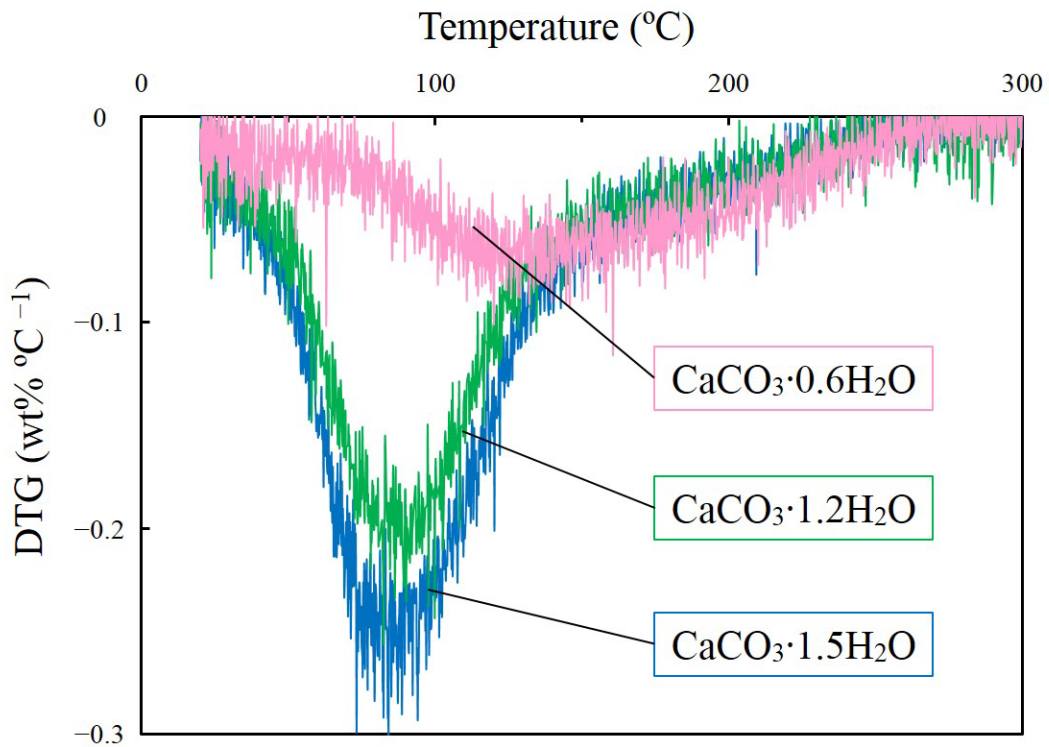


Figure 2–8. DTG curves of synthesized ACCs with different water contents.

### **2.3.1.2. X-ray diffraction**

XRD measurements is one of effective methods to identify ACC. Figure 2–9 shows XRD patterns of synthesized ACCs with different water contents and crystalline phases of calcium carbonate. The patterns of ACC samples presented no diffraction peak attributable to any crystalline phases of calcium carbonate but some broad halos which are specific to amorphous materials (Addadi et al., 2003; Michel et al., 2008). There is no significant difference in these peaks by water contents of ACCs.

It should be careful to store ACC samples because ACC easily crystallizes to more stable phases in a high-humidity condition. At the typical atmospheric condition in Japan (at about 20 °C and about 60 % relative humidity), ACC ( $\text{CaCO}_3 \cdot 1.5\text{H}_2\text{O}$ ) crystallized to vaterite and calcite in one day (see Figure 2–10 (a)). On the other hand, no crystallization was observed on the samples stored in a vacuum desiccator and in a refrigerator (see Figure 2–10 (b) and (c)). These results suggest that ACC samples should be stored at a vacuum condition or at low temperature.

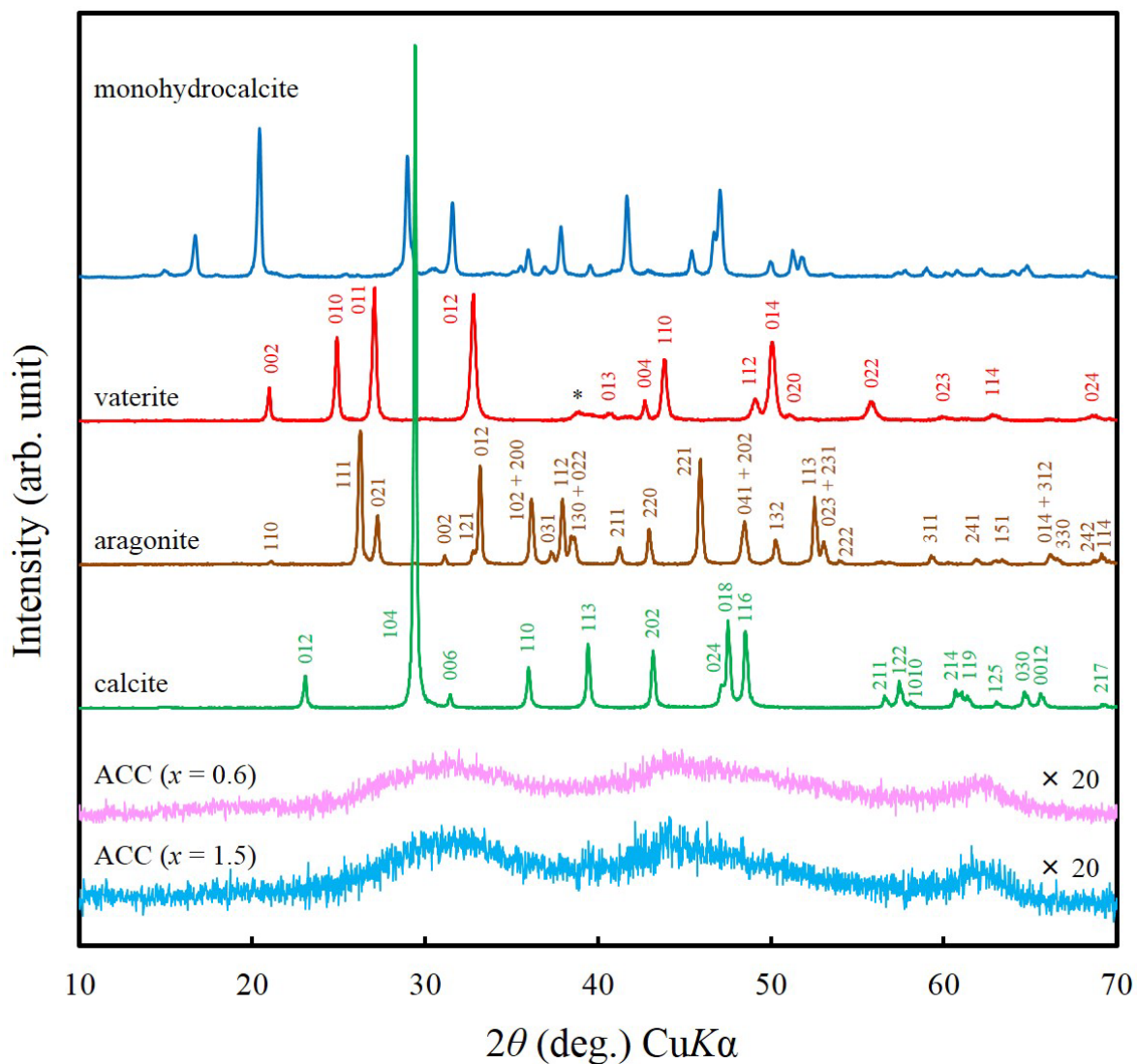


Figure 2–9. XRD patterns of ACCs ( $\text{CaCO}_3 \cdot x\text{H}_2\text{O}$ ) and crystalline phases of calcium carbonate. Indices of vaterite were referred from the structure model proposed by Kamhi (1963). Asterisk denotes a peak assignable to supercell. Indices of monohydrocalcite are not shown in the figure in order to avoid complication. In XRD patterns of ACC samples, no significant diffraction peak was observed.

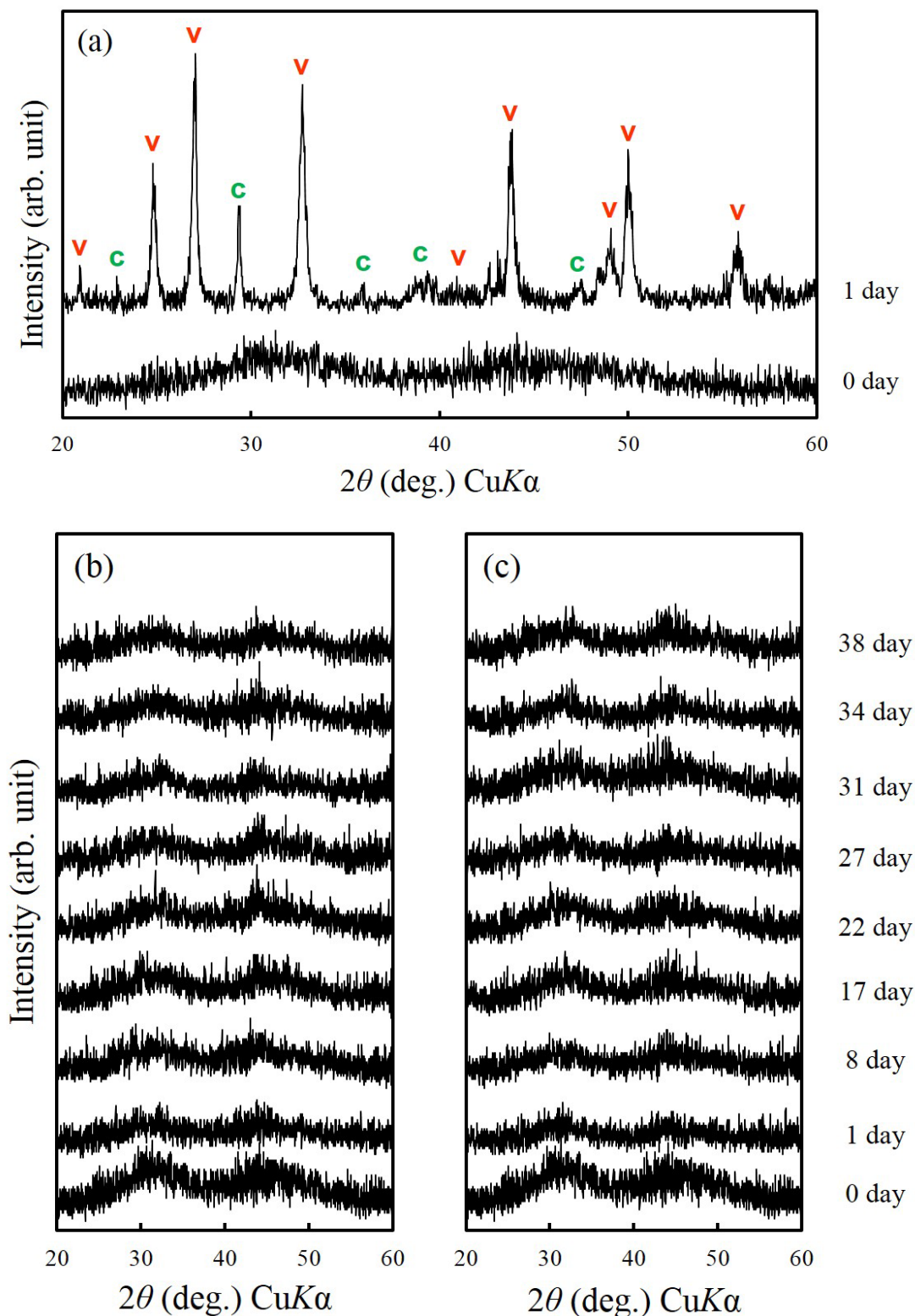


Figure 2–10. Time variation of XRD patterns of ACC ( $\text{CaCO}_3 \cdot 1.5\text{H}_2\text{O}$ ) at 3 different storage conditions: (a) in a glass vial at ambient pressure at room temperature, (b) in a vacuum desiccator at about  $10^2$  Pa at room temperature, and (c) in a glass vial cooled by a refrigerator at ambient pressure. **c**: calcite, and **v**: vaterite.

### 2.3.1.3. IR spectroscopy

Infrared spectroscopy has been also performed for the identification of ACC (Brečević and Nielsen, 1989; Addadi et al., 2003; Weiner et al., 2003; Politi et al., 2004; Radha et al., 2010; Gebauer et al., 2010). In general, the KBr-pellet method is applied to obtain IR spectra. Figure 2–11 shows IR spectra of ACC samples and standard crystalline phases of calcium carbonate obtained by the KBr-pellet method. It is known that IR spectra of ACC show four characteristic peaks attributable to carbonate ion of the symmetric stretch at  $1080\text{ cm}^{-1}$  ( $\nu_1$ ), the out-of-plane bending at  $866\text{ cm}^{-1}$  ( $\nu_2$ ), the asymmetric stretch at around  $1450\text{ cm}^{-1}$  ( $\nu_3$ ), and the in-plane bending at about  $700\text{ cm}^{-1}$  ( $\nu_4$ ) (Addadi et al., 2003; Weiner et al., 2003). IR spectra of ACC are especially characterized by the broad peak of  $\nu_1$  and split peaks of  $\nu_3$ , which indicate a lack of symmetry in the environment of the carbonate ions. The peaks of  $\nu_2$  and  $\nu_4$  are also broaden and are shifted to lower wavenumber than that of crystalline phases of calcium carbonate. These characteristics of ACC in IR spectra were observed in the spectrum of ACC ( $\text{CaCO}_3 \cdot 0.6\text{H}_2\text{O}$ ) (see Figure 2–11). However, IR spectrum of ACC ( $\text{CaCO}_3 \cdot 1.5\text{H}_2\text{O}$ ) shows a peak at  $745\text{ cm}^{-1}$  assigned by  $\nu_4$  of vaterite (Dupont et al., 1997), which is inconsistent with the results from XRD measurements. This result suggests that crystallization of ACC may occur during the preparation of KBr pellets and/or during IR measurements. Figure 2–12 (a) presents time-resolved IR spectra of ACC ( $\text{CaCO}_3 \cdot 1.5\text{H}_2\text{O}$ ). The peaks attributable to  $\nu_4$  of vaterite and calcite appears with time. This result indicates that ACC gradually crystallized during IR measurements by the KBr-pellet method.

## Chapter 2. Basic properties of ACC

The attenuated total reflection (ATR) method was introduced for IR measurements. The ATR method provides IR spectra without pretreatment. Time-resolved IR spectra from ATR measurements are shown in Figure 2–12 (b). In contrast to the KBr-pellet method, no crystalline phase was observed during ATR measurements. This result suggests that the ATR method is preferred for IR measurements of ACC.

Because of hygroscopic nature of KBr, water absorbed from ACC and/or air might promote the crystallization of ACC in this study. This observation is consistent with the results from XRD which ACC crystallized at a humid condition. However, the crystallization of ACC was not observed by many studies on IR spectra of ACC even with the KBr-pellet method (Brečević and Nielsen, 1989; Addadi et al., 2003; Politi et al., 2004; Radha et al., 2010). These results suggest that IR measurements of ACC by the KBr-pellet method required to avoid artifacts and to consider the stability of ACC and the experimental conditions.

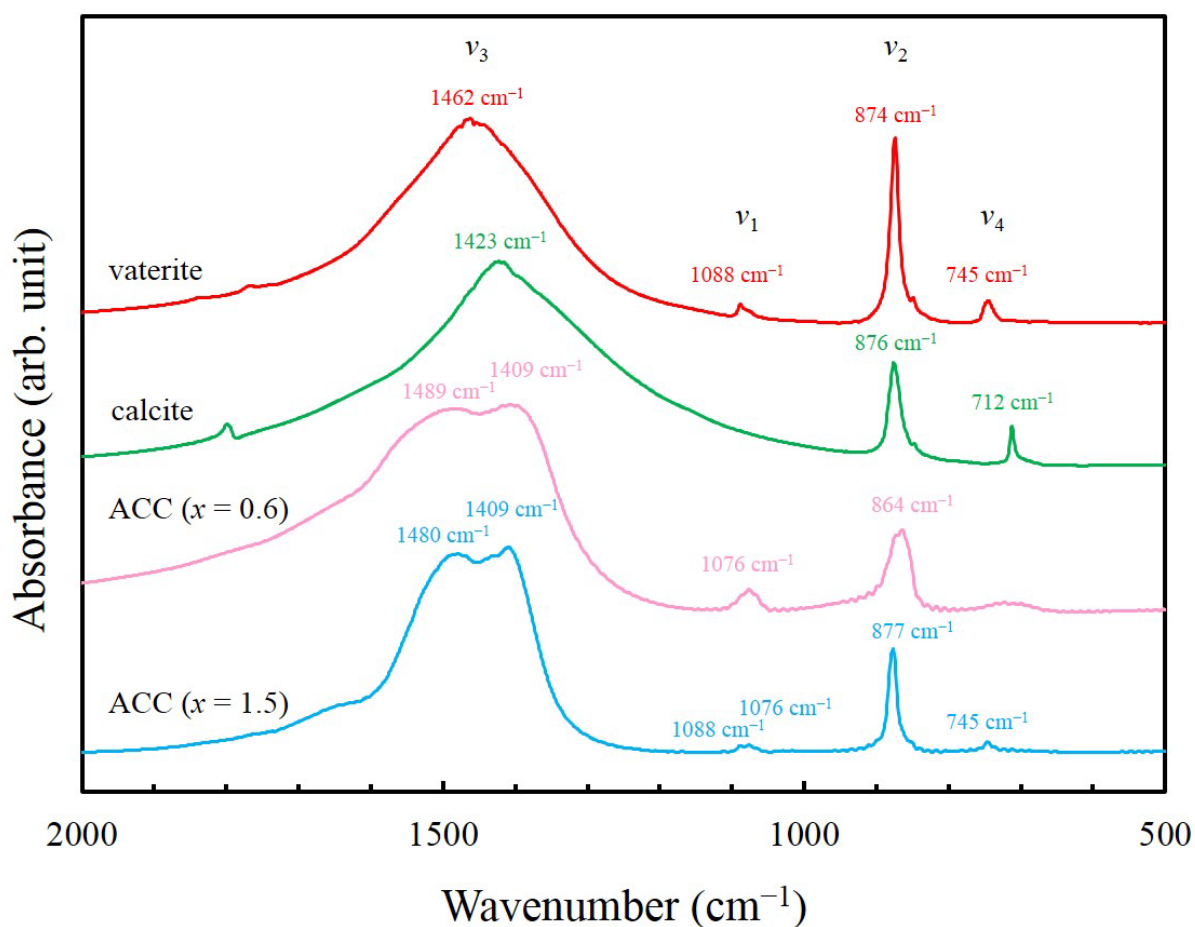


Figure 2–11. IR spectra of ACCs ( $\text{CaCO}_3 \cdot x\text{H}_2\text{O}$ ) and crystalline phases of calcium carbonate.

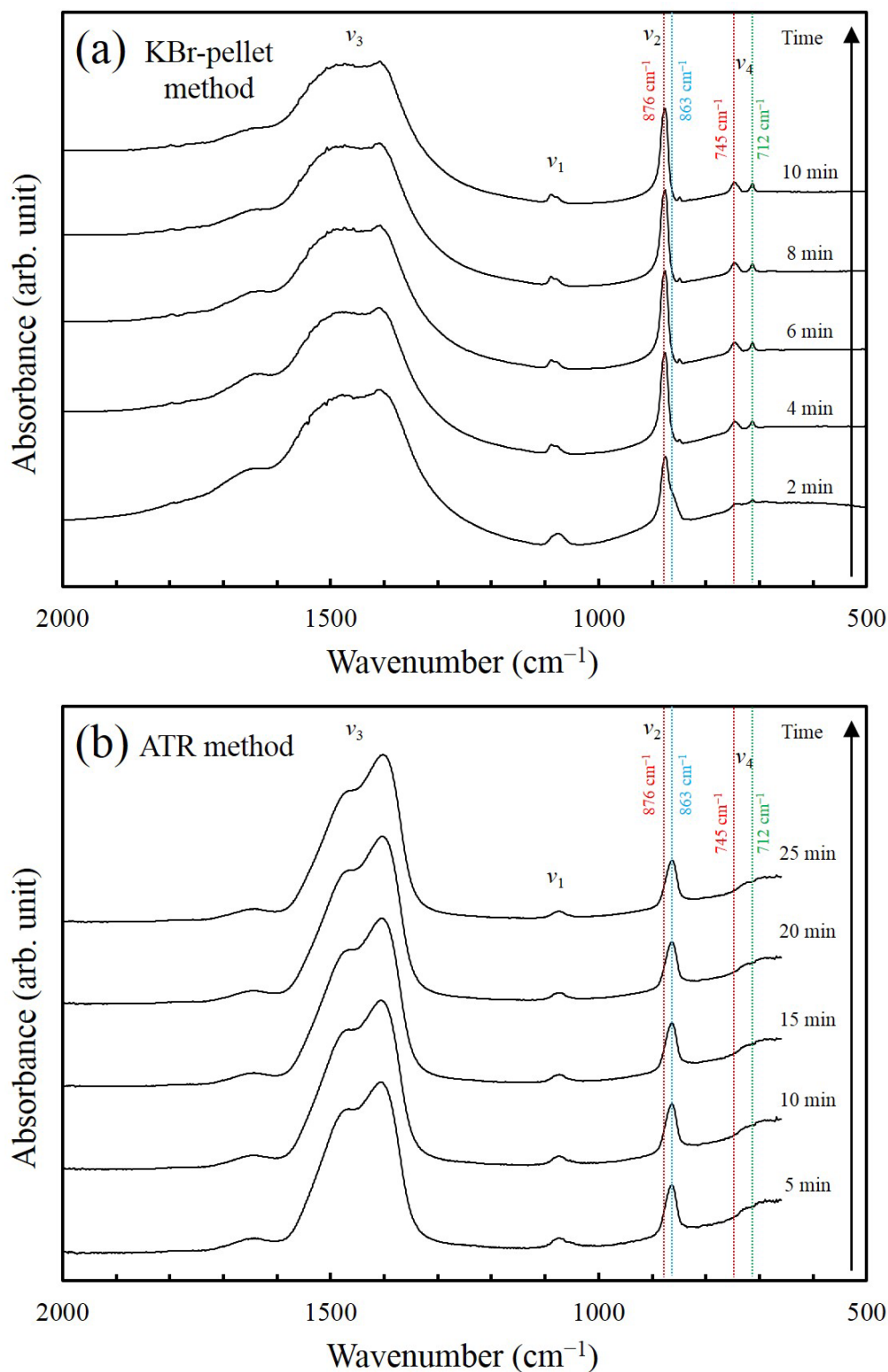


Figure 2–12. Time-resolved IR spectra of synthesized ACC ( $\text{CaCO}_3 \cdot 1.5\text{H}_2\text{O}$ ) using (a) the KBr–pellet method every 20 scans corresponding to about 2 min and (b) ATR method every 20 scans corresponding to about 5 min. Several lines present in-plane bending mode ( $\nu_4$ ) of vaterite ( $745 \text{ cm}^{-1}$ , red line) and calcite ( $712 \text{ cm}^{-1}$ , green line) and out-of-plane bending mode ( $\nu_2$ ) of calcite ( $876 \text{ cm}^{-1}$ , red line) and ACC ( $863 \text{ cm}^{-1}$ , light-blue line).

**2.3.1.4. Structural analysis using atomic pair distribution function (PDF)**

The reduced atomic pair distribution function (PDF)  $G(r)$  of ACC sample was obtained from the experimental X-ray diffraction data via a Fourier transform of the interference function by the following equation:

$$G(r) = 4\pi r(\rho(r) - \rho_0) = \frac{2}{\pi} \int_0^\infty Q[S(Q) - 1] \sin Qr \, dQ \quad (2-1),$$

where  $\rho_0$  is the average number density,  $\rho(r)$  is the atomic pair distribution function (PDF),  $Q$  is the magnitude of the scattering vector, and  $S(Q)$  is the structure factor (Murao et al., 2011).

Figure 2-13 (a) shows X-ray scattering profile of a synthesized ACC. Several diffuse peaks at about 2.3, 3.2, 5.5, and 8.4  $\text{\AA}^{-1}$  in  $Q$  were observed in this profile. The obtained  $G(r)$  is presented in Figure 2-13 (b). The atomic correlations at 1.3 and 2.4  $\text{\AA}$  are attributable to C–O and Ca–O correlations. The obtained result is consistent with that reported by Michel et al. (2008), which is characterized by the correlation at around 4 and 6  $\text{\AA}$ . However, it is difficult to discuss the structural similarity between ACC and crystalline polymorphs of calcium carbonate because the attenuation of intensity was remarkable at long-range correlation.

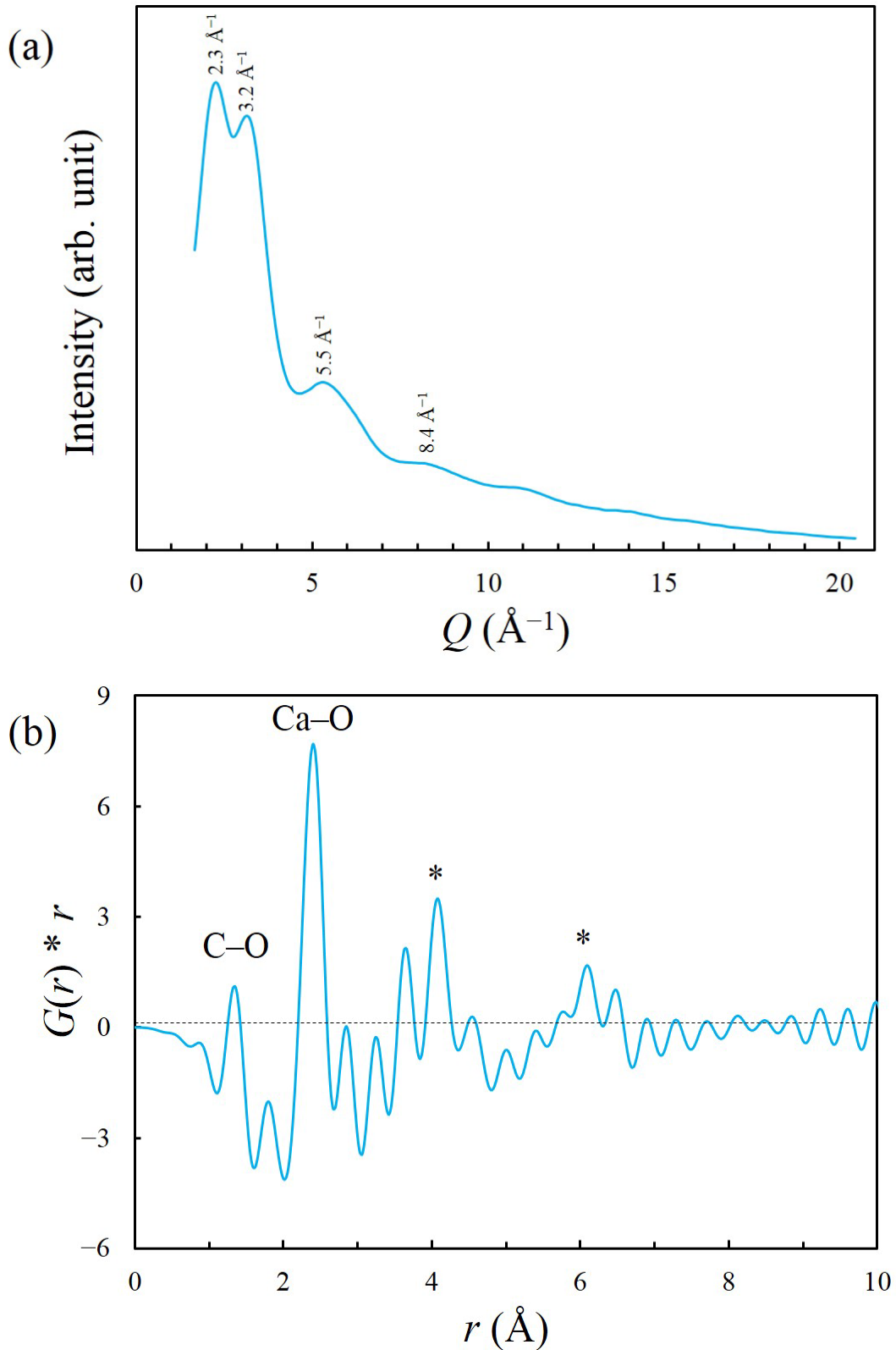


Figure 2-13. (a) X-ray scattering profile of ACC (CaCO<sub>3</sub>·1.5H<sub>2</sub>O) obtained in this study. (b) Reduced PDF  $G(r)$  obtained by a Fourier transform of the interference function. Vertical axis is scaled as  $G(r) \times r$  to amplify the weak correlations at high  $r$ . Asterisks denote the correlation characterized to ACC.

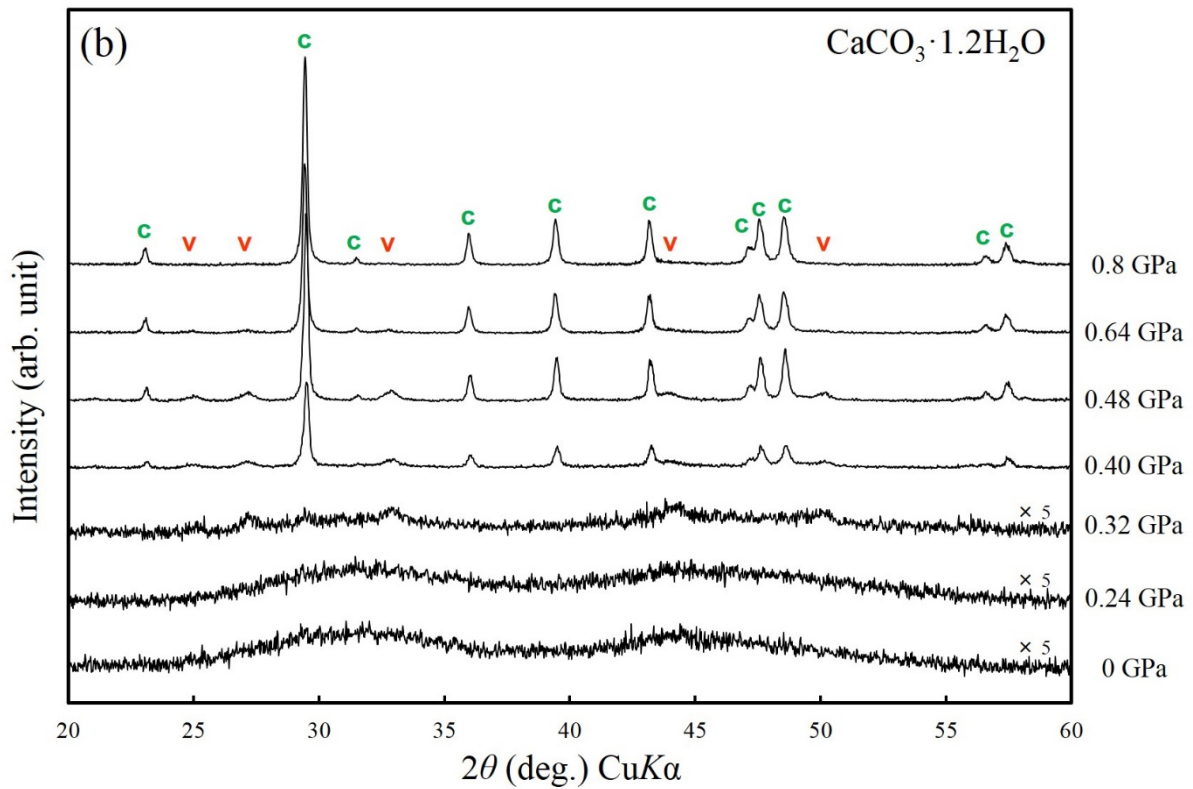
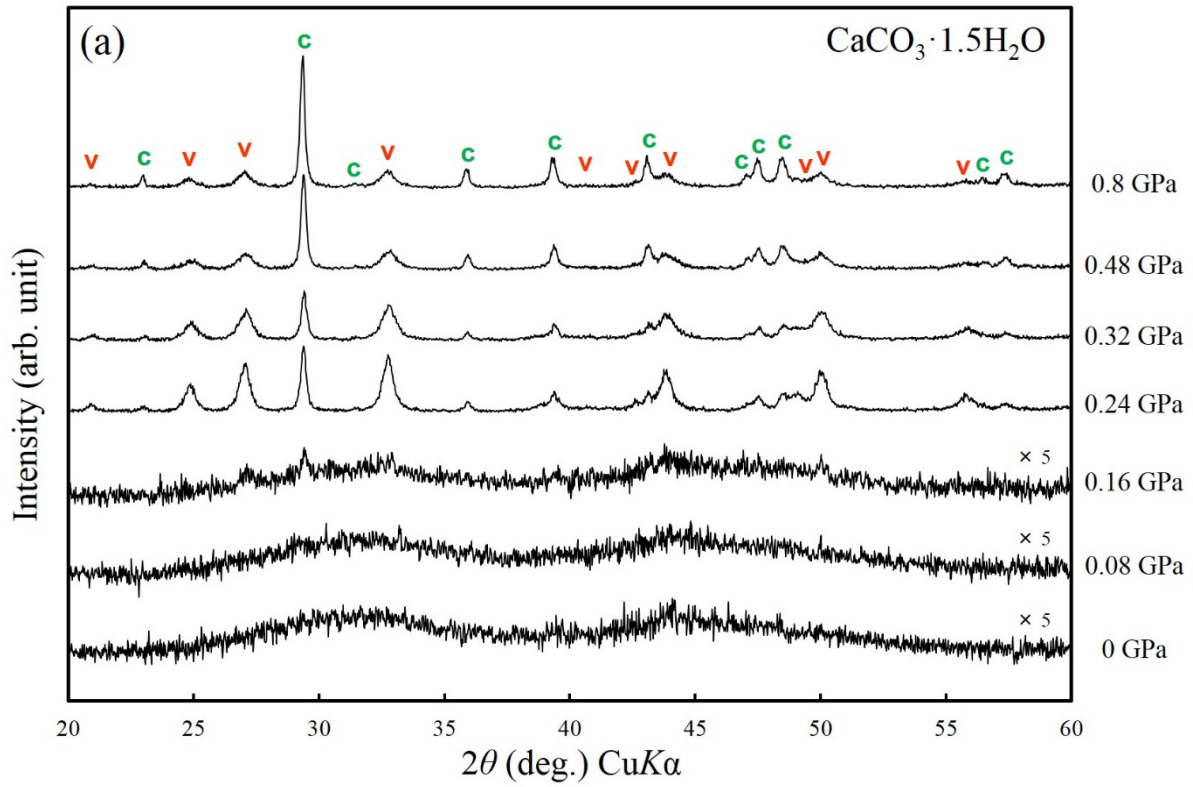
## **2.3.2. High-pressure experiments of ACC for recovered samples**

### **2.3.2.1. X-ray diffraction patterns**

Figure 2–14 shows XRD patterns of three types of ACC with different water contents and the samples recovered from each pressure. No diffraction peak was observed in the XRD patterns from ACC samples before compression. In some XRD patterns of pressurized samples, sharp diffraction peaks were observed. These peaks were attributable to crystalline phases of calcium carbonate: calcite and vaterite. These results indicate that ACC crystallized to calcite and vaterite by applying pressure. The crystallized pressures of  $\text{CaCO}_3 \cdot 1.5\text{H}_2\text{O}$ ,  $\text{CaCO}_3 \cdot 1.2\text{H}_2\text{O}$ , and  $\text{CaCO}_3 \cdot 0.6\text{H}_2\text{O}$  were 0.24, 0.4, and 0.64 GPa, respectively. The crystallized pressure of lower  $\text{H}_2\text{O}$  content was higher than that of higher  $\text{H}_2\text{O}$  content. This result is consistent with Radha et al. (2010), which reported that anhydrous ACC was more stable energetically than hydrous ACC.

The pressure-induced crystallization of ACC occurred at more than one order of magnitude lower pressures than that of amorphous materials reported previously (He et al., 2002; Xu et al., 2010; Pandey et al., 2011). This result implies that the mechanism of pressure-induced crystallization of ACC is different from that of other amorphous materials. In fact, water in ACC would play an important role in the crystallization mechanism, because dehydration from ACC was observed on crystallized samples after recovered from high pressure.

Chapter 2. Basic properties of ACC



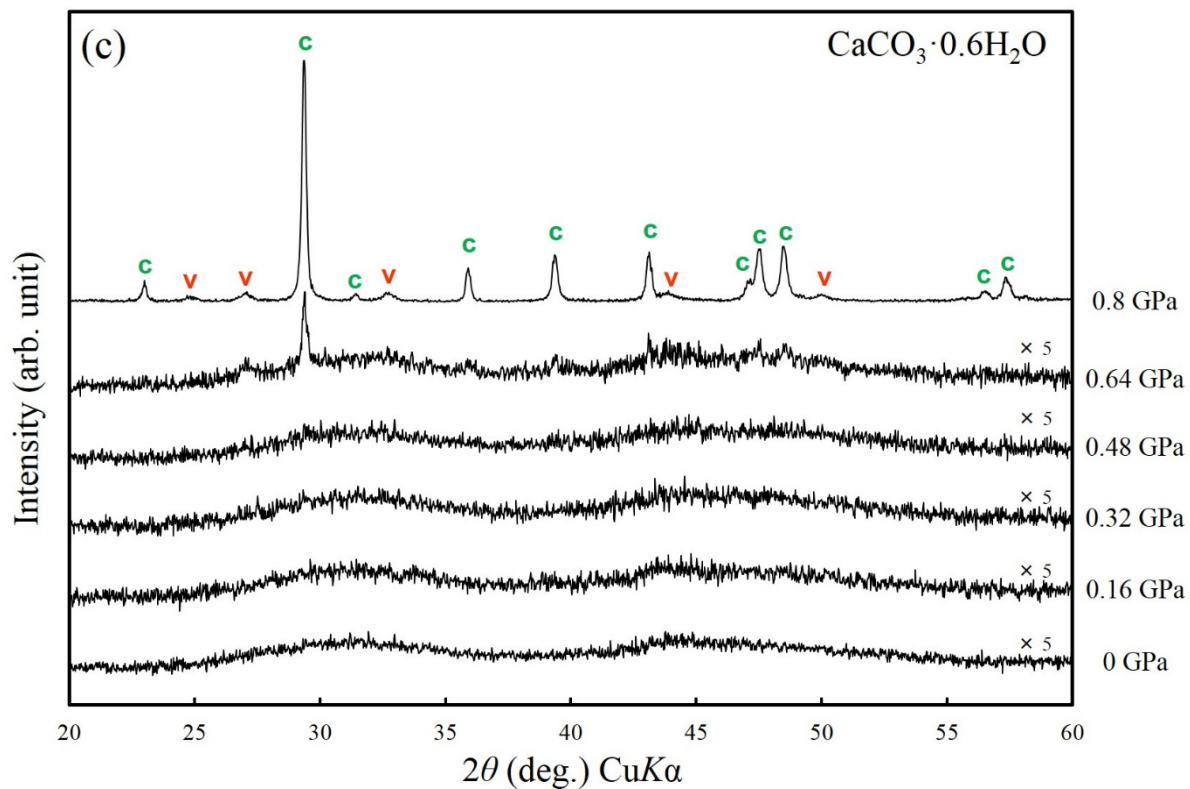


Figure 2–14. XRD patterns of the synthesized ACCs and compressed samples: (a)  $\text{CaCO}_3 \cdot 1.5\text{H}_2\text{O}$ , (b)  $\text{CaCO}_3 \cdot 1.2\text{H}_2\text{O}$ , and (c)  $\text{CaCO}_3 \cdot 0.6\text{H}_2\text{O}$ . ‘v’ and ‘c’ denote the diffraction peaks of vaterite and calcite, respectively.

## Chapter 2. Basic properties of ACC

The relative abundance of vaterite to calcite was calculated from the intensity ratio of diffraction peaks at 012 for vaterite and 104 for calcite (Kontoyannis and Vagenas, 2000). Figure 2–15 shows the calibration line obtained from standard mixtures, which were prepared from reagent calcite and synthesized vaterite (detail of the synthesizing method of vaterite was described in Chapter 4). The vaterite/calcite ratios of recovered samples are shown in Table 2–1. The relative abundance of vaterite decreased with increased applied pressure. The density of vaterite is  $2.65 \text{ g cm}^{-3}$ , which is smaller than that of calcite ( $2.71 \text{ g cm}^{-3}$ ) at ambient condition (Kamhi, 1963; Markgraf and Reeder, 1985). Therefore, the decrease of vaterite/calcite ratio at higher pressure might be reasonable.

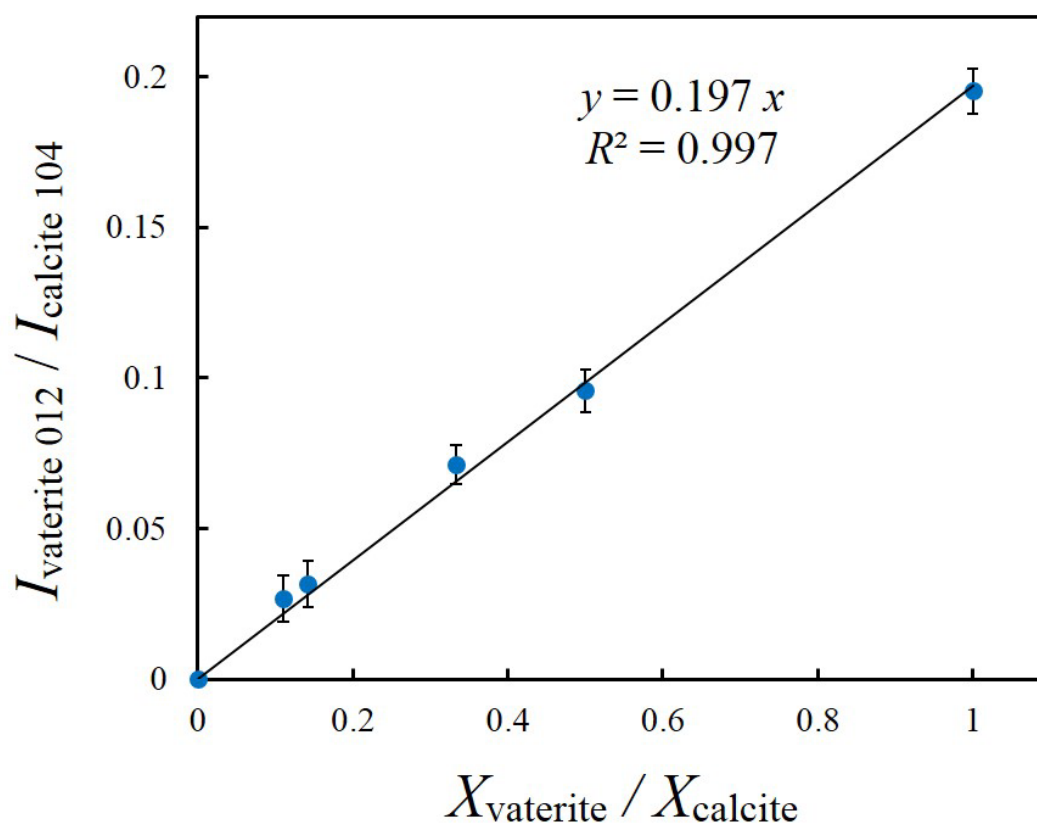


Figure 2–15. Calibration line for vaterite/calcite ratio calculated from the intensities of vaterite (012 reflection) and calcite (104 reflection). The index of vaterite was referred from the structure model proposed by Kamhi (1963).

Chapter 2. Basic properties of ACC

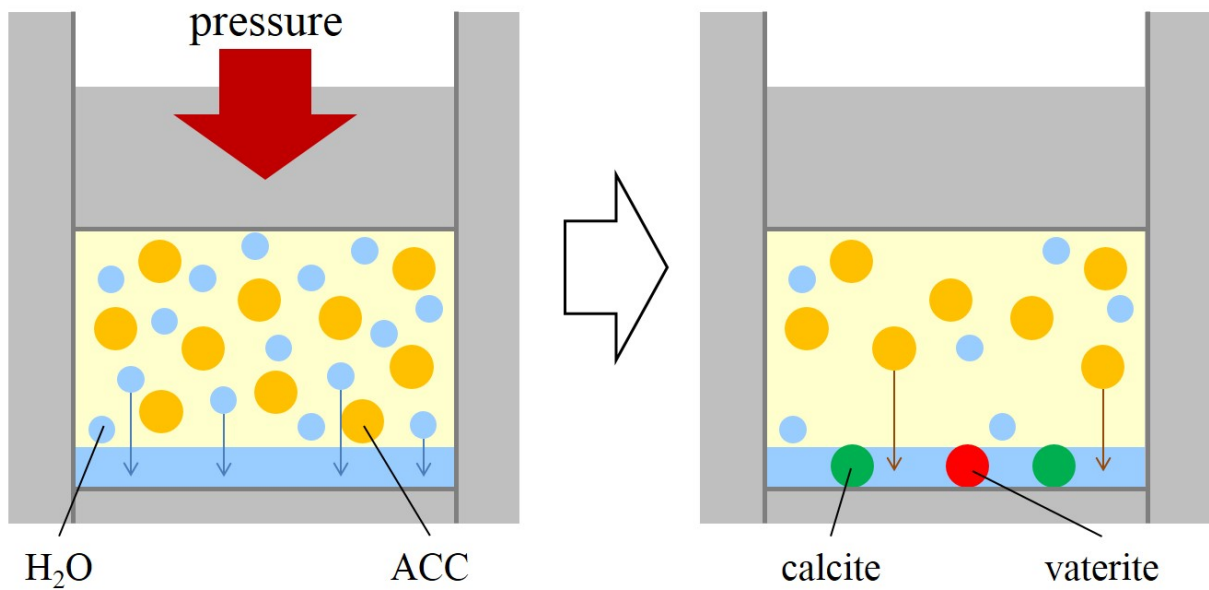
Table 2–1. Relative abundance of vaterite to calcite in the recovered samples.

Pressure (GPa)	$X_{\text{vaterite}} / X_{\text{calcite}}$		
	$\text{CaCO}_3 \cdot 1.5\text{H}_2\text{O}$	$\text{CaCO}_3 \cdot 1.2\text{H}_2\text{O}$	$\text{CaCO}_3 \cdot 0.6\text{H}_2\text{O}$
0.08	–	(no data)	(no data)
0.16	–	(no data)	–
0.24	0.165(2)	–	(no data)
0.32	0.139(3)	0.23(4)	–
0.40	(no data)	0.0145(16)	(no data)
0.48	0.0356(13)	0.0098(12)	–
0.64	(no data)	0.0024(11)	0.014(7)
0.80	0.0237(11)	0.0011(8)	0.0063(9)

**2.3.2.2. Pressure-induced crystallization process**

The present study clarified that the crystallization pressure and the vaterite/calcite ratio were dependent on water contents of ACC. Moreover, the difference in water contents of ACC resulted from the amount of adsorbed water. These results indicate that the adsorbed water in ACC plays an important role for the crystallization process at high pressure. The higher water contents resulted in higher vaterite/calcite ratio. Water in ACC would promote the crystallization to vaterite or inhibit the formation of calcite. In a supersaturated solution, ACC transforms to metastable vaterite in an early stage because of kinetic advantages (Tsuno et al., 2001; Navrotsky, 2004). From these results, I proposed a possible mechanism of pressure-induced crystallization (see Figure 2-16). At first, pressure-induced dehydration from ACC occurred. ACCs with lower H<sub>2</sub>O contents would require higher pressure for dehydration. ACC dissolved in the dehydrated water because of its high solubility, and then, vaterite and calcite crystallized from the supersaturated solution with respect to those crystalline phases. In other words, pressure-induced crystallization from ACC occurred by pressure-induced dehydration and dissolution-reprecipitation process.

ACC with high H<sub>2</sub>O content



ACC with low H<sub>2</sub>O content

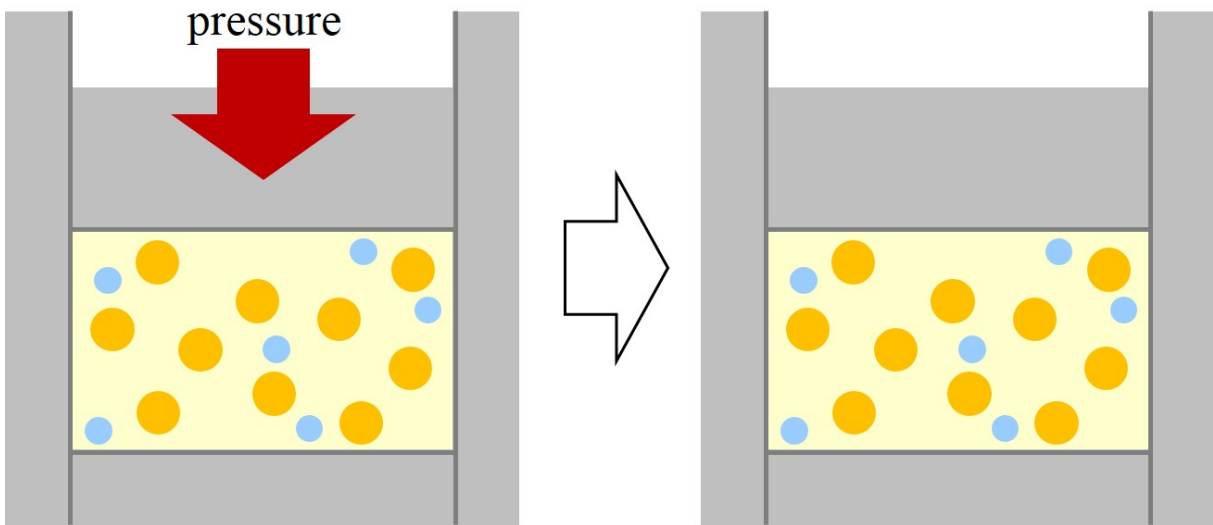


Figure 2–16. Schematic illustrations of proposed mechanism of pressure-induced crystallization from ACC to vaterite and calcite. ACC with high H<sub>2</sub>O content dehydrated by applied pressure, and vaterite and calcite crystallized in dehydrated fluid by dissolution-reprecipitation process. On the other hand, ACC with low H<sub>2</sub>O content did not dehydrate at lower pressure, which resulted in no crystallization.

## **2.4. Conclusion**

Basic properties of ACC used in this study investigated by TG analysis, XRD, IR spectroscopy, and PDF analysis. The crystallization of ACC occurred by the preservation at humid conditions and by the preparation of KBr pellets because of its metastability. The careful treatments are required to prevent from the crystallization of ACC when ACC is used for some experiments.

I have found the pressure-induced crystallization phenomena from ACC to vaterite and calcite. The crystallization pressure and the polymorph ratio depended on water contents of ACC. Moreover, I proposed a possible mechanism of the pressure-induced crystallization from the obtained results. However, additional experiments are required to validate the proposed crystallization mechanism. For example, the crystallization pathway is still unclear. The dependence of vaterite/calcite ratio on applied pressure suggests two possibilities on the formation pathways. The first is that calcite and vaterite independently formed from ACC. The second is that vaterite formed from ACC and calcite transformed via metastable vaterite. For better understanding on pressure-induced crystallization from ACC, in situ observation during pressure-induced crystallization is required, which is described in Chapter 3. In addition, the pressure behavior of vaterite provides important information to understand the formation process of calcite, which is presented in Chapter 4.

## References

- Addadi L, Raz S, and Weiner S (2003) Taking Advantage of Disorder: Amorphous Calcium Carbonate and Its Roles in Biomineralization. *Advanced Materials*, **15**, 959–970.
- Bots P, Benning LG, Rodriguez-Blanco JD, Roncal-Herrero T, and Shaw S (2012) Mechanistic Insights into the Crystallization of Amorphous Calcium Carbonate (ACC). *Crystal Growth & Design*, **12**, 3806–3814.
- Brečević L, and Nielsen AE (1989) SOLUBILITY OF AMORPHOUS CALCIUM CARBONATE. *Journal of Crystal Growth*, **98**, 504–510.
- Cromer DT, and Mann JB (1967) Compton Scattering Factors for Spherically Symmetric Free Atoms. *The Journal of Chemical Physics*, **47**, 1892–1893.
- Dupont L, Portemer F, and Figlarz M (1997) Synthesis and study of a well crystallized CaCO<sub>3</sub> vaterite showing a new habitus. *Journal of Materials Chemistry*, **7**, 797–800.
- Gebauer D, Gunawidjaja PN, Ko JYP, Bacsik Z, Aziz B, Liu L, Hu Y, Bergström L, Tai CW, Sham TK, Edén M, and Hedin N (2010) Proto-Calcite and Proto-Vaterite in Amorphous Calcium Carbonates. *Angewandte Chemie*, **49**, 8889–8891.
- He D, Zhao Q, Wang WH, Che RZ, Liu J, Luo XJ, and Wang WK (2002) Pressure-induced crystallization in a bulk amorphous Zr-based alloy. *Journal of Non-Crystalline Solids*, **297**, 84–90.
- Ibers JA, and Hamilton WC (1974) *International Tables for X-ray Crystallography*. Vol. IV. Kynoch, Birmingham.
- Ihli J, Wong WC, Noel EH, Kim YY, Kulak AN, Christenson HK, Duer MJ, and Meldrum FC (2014) Dehydration and crystallization of amorphous calcium carbonate in solution and in air. *Nature Communications*, **5**, 3169, doi: 10.1038/ncomms4169.
- Kamhi SR (1963) On the Structure of Vaterite, CaCO<sub>3</sub>. *Acta Crystallographica*, **16**, 770–772.
- Koga N, Nakagoe Y, and Tanaka H (1998) Crystallization of amorphous calcium carbonate. *Thermochimica Acta*, **318**, 239–244.
- Kojima Y, Kawanobe A, Yasue T, and Arai Y (1993) Synthesis of Amorphous Calcium Carbonate and Its Crystallization. *Journal of the Ceramic Society of Japan*, **101**, 1145–1152.
- Kontoyannis CG, and Vagenas NV (2000) Calcium carbonate phase analysis using XRD and FT-Raman spectroscopy. *Analyst*, **125**, 251–255.

## Chapter 2. Basic properties of ACC

- Markgraf SA, and Reeder RJ (1985) High-temperature structure refinements of calcite and magnesite. *American Mineralogist*, **70**, 590–600.
- Michel FM, MacDonald J, Feng J, Phillips BL, Ehm L, Tarabrella C, Parise JB, and Reeder RJ (2008) Structural Characteristics of Synthetic Amorphous Calcium Carbonate. *Chemistry of Materials*, **20**, 4720–4728.
- Murao R, Sugiyama K, Kashiwagi Y, Kameoka S, and Tsai AP (2011) Atomic pair distribution function (PDF) analysis of Raney Pd and Ph fine particles. *Philosophical Magazine*, **91**, 2954–2961.
- Navrotsky A (2004) Energetic clues to pathways to biomineralization: Precursors, clusters, and nanoparticles. *Proceedings of the National Academy of Sciences of the United States of America*, **101**, 12096–12101.
- Nielsen MH, Aloni S, and De Yoreo JJ (2014) In situ TEM imaging of CaCO<sub>3</sub> nucleation reveals coexistence of direct and indirect pathways. *Science*, **345**, 1158–1162.
- Ogino T, Suzuki T, and Sawada K (1987) The formation and transformation mechanism of calcium carbonate in water. *Geochimica et Cosmochimica Acta*, **51**, 2757–2767.
- Pandey KK, Garg N, Shanavas KV, Sharma SM, and Sikka SK (2011) Pressure induced crystallization in amorphous silicon. *Journal of Applied Physics*, **109**, 113511-1–7.
- Politi Y, Arad T, Klein E, Weiner S, and Addadi L (2004) Sea Urchin Spine Calcite Forms via a Transient Amorphous Calcium Carbonate Phase. *Science*, **306**, 1161–1164.
- Radha AV, Forbes TZ, Killian CE, Gilbert PUPA, and Navrotsky A (2010) Transformation and crystallization energetics of synthetic and biogenic amorphous calcium carbonate. *Proceedings of the National Academy of Sciences of the United States of America*, **107**, 16438–16443.
- Rodriguez-Blanco JD, Shaw S, and Benning LG (2011) The kinetics and mechanisms of amorphous calcium carbonate (ACC) crystallization to calcite, via vaterite. *Nanoscale*, **3**, 265–271.
- Sato T, and Funamori N (2008) Sixfold-Coordinated Amorphous Polymorph of SiO<sub>2</sub> under High Pressure. *Physical Review Letters*. **101**, 255502-1–4.
- Tao J, Zhou D, Zhang Z, Xu X, and Tang R (2009) Magnesium-aspartate-based crystallization switch inspired from shell molt of crustacean. *Proceedings of the National Academy of Sciences of the United States of America*, **106**, 22096–22101.
- Tsuno H, Kagi H, and Akagi T (2001) Effects of Trace Lanthanum Ion on the Stability of Vaterite and Transformation from Vaterite to Calcite in an Aquatic System. *Bulletin of the Chemical Society of Japan*, **74**, 479–486.

## Chapter 2. Basic properties of ACC

- Wagner CNJ, Ocken H, and Joshi ML (1965) Interference and Radial Distribution Functions of Liquid Copper, Silver, Tin, and Mercury. *Zeitschrift für Naturforschung A*, **20**, 325–335.
- Waseda Y, Matsubara E, and Sugiyama K (1988) Anomalous X-ray Scattering Facility for Structural Characterization of Materials using Synchrotron Radiation. *Science reports of the Research Institutes, Tohoku University. Ser. A, Physics, chemistry and metallurgy*, **34**, 1–14.
- Weiner S, Levi-Kalishman Y, Raz S, and Addadi L (2003) Biologically Formed Amorphous Calcium Carbonate. *Connective Tissue Research*, **44**, 214–218.
- Xu M, Meng Y, Cheng YQ, Sheng HW, Han XD, and Ma E (2010) Pressure-induced crystallization of amorphous  $\text{Ge}_2\text{Sb}_2\text{Te}_5$ . *Journal of Applied Physics*, **108**, 083519-1–5.
- Yoshino T, Maruyama K, Kagi H, Nara M, and Kim JC (2012) Pressure-Induced Crystallization from Amorphous Calcium Carbonate. *Crystal Growth & Design*, **12**, 3357–3361.

## **Chapter 3.**

**Kinetic observation of pressure-induced crystallization of  
ACC: in situ time-resolved X-ray observation and  
observation by SEM and Raman spectroscopy**

### **3.1. Introduction**

In Chapter 2, experiments based on observations of recovered samples using a pelleter are described. The results of the recovering experiments suggest that thermodynamically stable calcite and metastable vaterite co-occurred from ACC by applying pressure. However, it is difficult to determine the pathway of crystallization from ACC to calcite by recovering experiments. There are two possibilities on the pathway under high pressure. The first pathway is that calcite and vaterite formed directly from ACC simultaneously. The second one is that calcite transformed from vaterite which crystallized from ACC. To investigate the kinetics and mechanisms of pressure-induced crystallization from ACC, it is important to perform in situ observation during crystallization of ACC at high pressure.

Some studies reported in situ observation of crystallization from ACC in a supersaturated solution. Rodriguez-Blanco et al. (2011) and Bots et al. (2012) reported time-resolved X-ray observations of the transformation from ACC to calcite via vaterite by energy-dispersive and angle-dispersive XRD methods, respectively. Recently, Nielsen et al. (2014) reported in situ TEM imaging of calcium carbonate nucleation. They suggested that multiple nucleation pathways, which are direct formation from solution and indirect transformation via metastable precursors, occurred. These studies directly provide us the information during crystallization and nucleation.

The combination of time-resolved XRD measurements and high-pressure experiments at a synchrotron facility has been applied to kinetic studies (Horikawa et al., 2001; Inoue et al., 2009). For example, Inoue et al. (2009) investigated the dehydration rate and kinetics of serpentine with increasing temperature (up to 900 °C) at high pressure (3–9 GPa) using multi-anvil apparatus equipped at the synchrotron beamline of Photon Factory, KEK.

This chapter presents in situ XRD observation on crystallization from ACC at high pressure using a multi-anvil apparatus. Moreover, texture observation on samples recovered from the high-pressure experiments can provide more information to elucidate the crystallization mechanism. The results of SEM observation and Raman spectroscopy on the recovered samples are also described in this chapter.

## **3.2. Experimental procedures**

### **3.2.1. Sample preparation**

ACC samples were synthesized with the same method described in Chapter 2. As shown in Chapter 2, ACC with higher H<sub>2</sub>O contents crystallized at lower pressure. For example, ACC (CaCO<sub>3</sub>·*x*H<sub>2</sub>O, *x* = 1.5) crystallized at 0.24 GPa and room temperature. However, it is experimentally difficult to measure and to control pressure at such a lower pressure. In this study, I prepared ACC with low H<sub>2</sub>O content for in situ observation of pressure-induced crystallization from ACC. ACC precipitation was obtained by the same method described in Chapter 2. After drying using a diaphragm pump for 24 h, additional evacuation was conducted using a turbo-molecular pump for 24 h. Water content of ACC was estimated from the weight loss of thermogravimetry (TG) curve, and was 0.67 of *x* value. From the results in Chapter 2, the ACC is expected to crystallize at about 0.6 GPa.

### 3.2.2. Setup for high-pressure experiments

High-pressure experiments were conducted at the AR-NE5C beamline of Photon Factory-Advanced Ring (PF-AR), High Energy Accelerator Research Organization (KEK), Japan. This beamline was equipped with a cubic-type high-pressure apparatus (MAX 80) introduced a multi-anvil 6-6 system, which has an advantage in replacement of the second stage anvils with suitable truncation sizes (Figure 3-1; Nishiyama et al., 2008; Kawazoe et al., 2010). In many cases, the second stage-anvils with 3-6 mm of truncated edge length (TEL), which were made by tungsten carbide, were often used in this beamline. On the other hand, the results from recovered experiments described in Chapter 2 suggest that the pressure-induced crystallization from ACC is expected to occur below 1 GPa. Therefore, I used a relatively large TEL of 10 mm for the second stage anvils (see Figure 3-2).

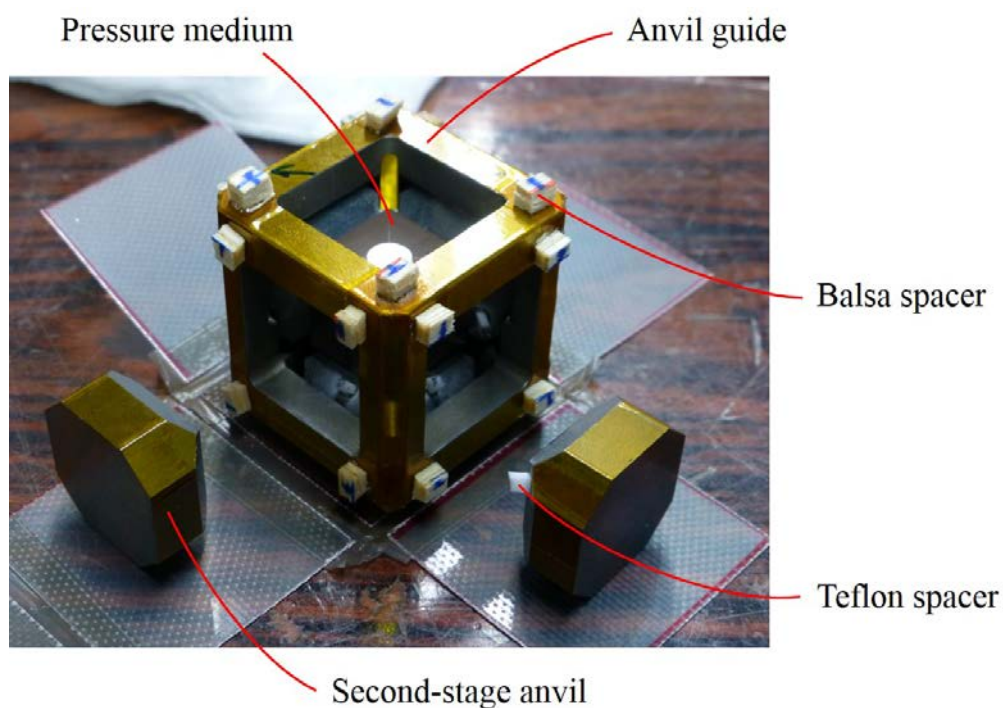


Figure 3-1. Photograph of the multi-anvil 6-6 assembly. In a general experiment at high temperature and high pressure, an anvil guide and second-stage anvils were coated with Kapton tape for electrical insulation. In my experiments, I also used Kapton tape because the anvil guide and these anvils were made by taking the thickness of Kapton tape into consideration. Balsa spacers and Teflon spacers maintained the anvil alignment before compression.

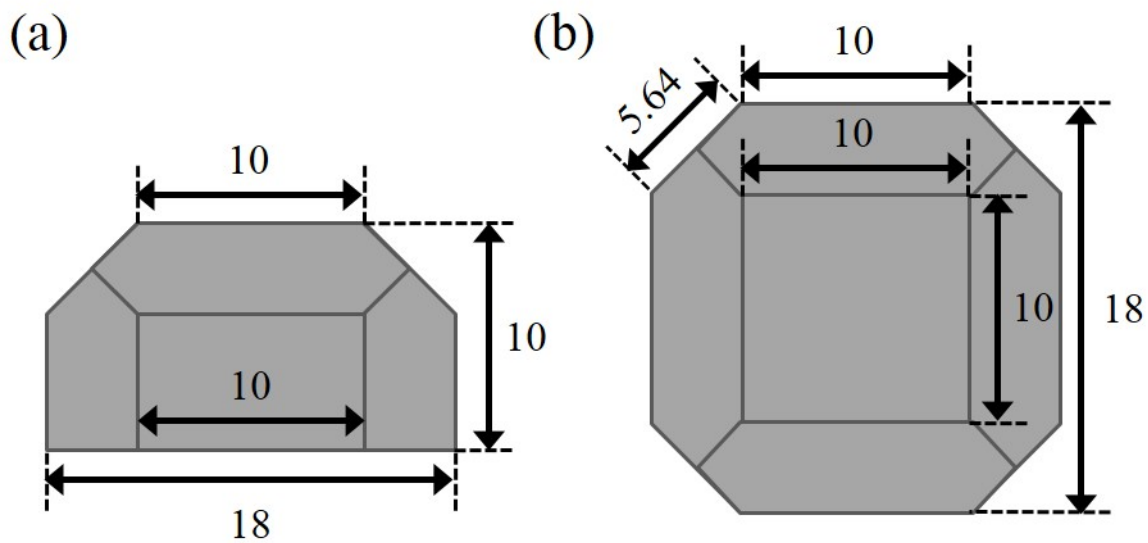


Figure 3–2. Schematic diagrams of a second-stage anvil used in my experiments. (a) Side view and (b) top view of the anvil. The unit of length is millimeter.

### Chapter 3. Kinetic observation of pressure-induced crystallization of ACC

The cell assembly used in this study is shown in Figure 3–3. Boron-epoxy was used as a pressure-transmitting medium; amorphous boron powder and epoxy resin were mixed in a weight ratio of 4:1. This mixture was pressed using a tetragonal mold at 47 MPa, and heated at 110 °C for 10 h. I prepared three hexagonal-boron nitride (h-BN) cylinders to load samples and pressure markers. The first layer was a pressure marker, which was a mixed powder of NaCl and Au (10:1 in a weight ratio). In the second layer, ACC sample mixed with Au powder (20:1 in a weight ratio) was loaded. This second layer was used for time-resolved XRD measurements to estimate pressure in parallel with sample measurements. Third layer contained pure ACC for SEM observations after high-pressure experiment. In general high-pressure and high-temperature experiments of hydrated samples, the pressure marker containing NaCl was loaded into the lower layer for preventing NaCl crystals from growing to coarse grains by dehydrated water. In this study, the high-pressure experiments were conducted at room temperature. The pressure marker was loaded into upper layer with consideration for influence of gravity.

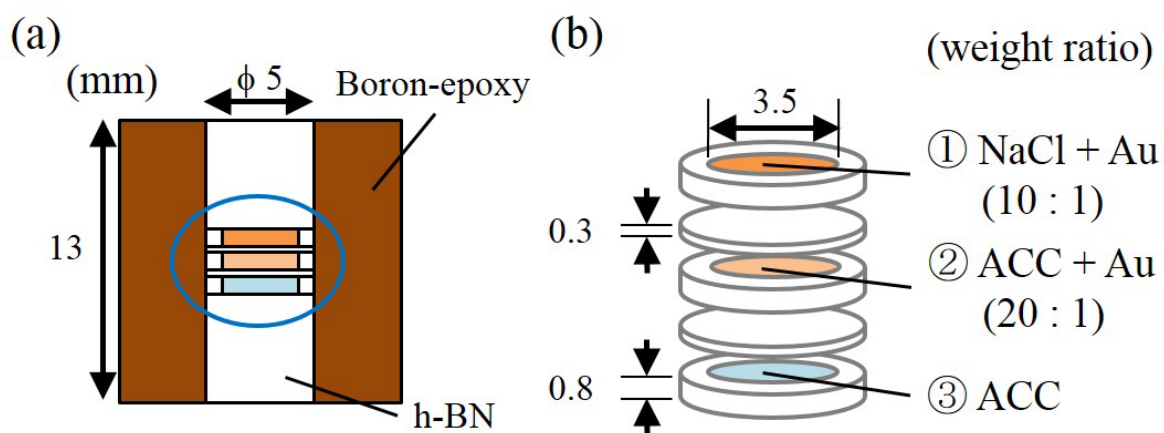


Figure 3–3. (a) Cell assembly used for in this high-pressure experiments. (b) Details of the sample holder inside of a blue circle in the left figure. Each layer was separated by BN disks.

### **3.2.3. In situ X-ray diffraction observations at high pressure**

X-ray diffraction patterns were collected by energy-dispersive XRD method at the AR–NE5C beamline of PF–AR, KEK. Schematic diagram of experimental layout is shown in Figure 3–4. A white X-ray beam, which was shaped to 100  $\mu\text{m}$   $\times$  200  $\mu\text{m}$  rectangle (vertical and horizontal, respectively) by slits, was used as an incident beam. The diffracted X-ray was collimated to 100  $\mu\text{m}$  in vertical direction and detected by a Ge solid-state detector (SSD) after through the receiving slits (200  $\mu\text{m}$   $\times$  300  $\mu\text{m}$ ). Energy was calibrated by characteristic X-rays of eight elements (Mo, Ag, Ba, Nd, Dy, Ta, Au, and Bi) (see Figure 3–5). The SSD was located at a  $2\theta$  angle of about  $6^\circ$ . Accurate position of the SSD was calibrated from lattice parameters of NaCl loaded in the first layer of the cell assembly before compression.

In situ high-pressure experiments were carried out in the following two steps. In the first step, the high-pressure cell was compressed at an oil discharge flow rate of  $0.8 \text{ cc min}^{-1}$  by the maximum load of 33 tons (equivalent to 0.2 GPa by NaCl scale) and XRD patterns from the three sample layers (see Figure 3–3) were obtained by changing the press height at each pressure. The first step was conducted to detect crystallization from ACC by XRD measurements and to obtain pressure calibration data from two sample layers (see layer 1 and 2 in Figure 3–3 (b)) for the next step. Each XRD pattern was collected for exposure time of 300 s. The generated pressures were calculated from diffraction peaks of NaCl and Au using the equation of state of NaCl proposed by Decker (1971) and that of Au proposed by Anderson et al. (1989). In second step, to investigate in situ observations on crystallization of ACC by applying pressure as driving force, time-resolved XRD measurements of the second layer (ACC + Au) were conducted every 10 s with increasing pressure from 33 tons to the end of crystallization at an oil discharge flow rate of  $0.1 \text{ cc min}^{-1}$ . All high-pressure experiments were performed at room temperature.

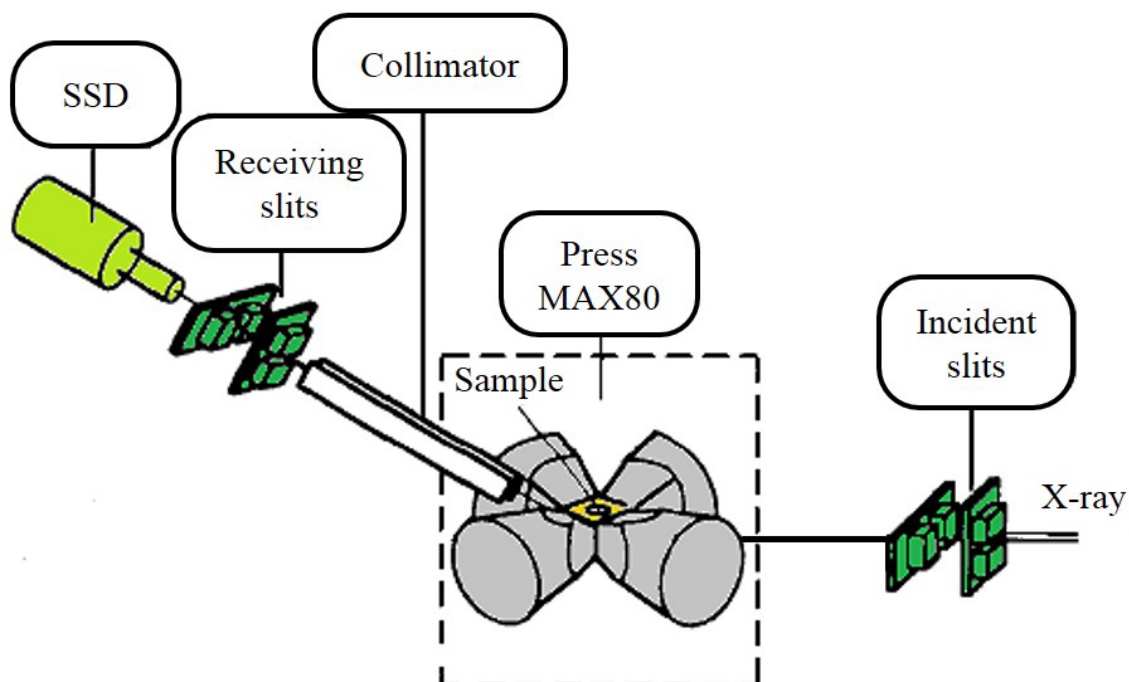


Figure 3–4. Schematic diagram of the facility for energy-dispersive XRD experiments at the synchrotron beamline of PF-AR (Chen et al., 1997, modified). The top and bottom anvils are not depicted to show the inside of anvils.

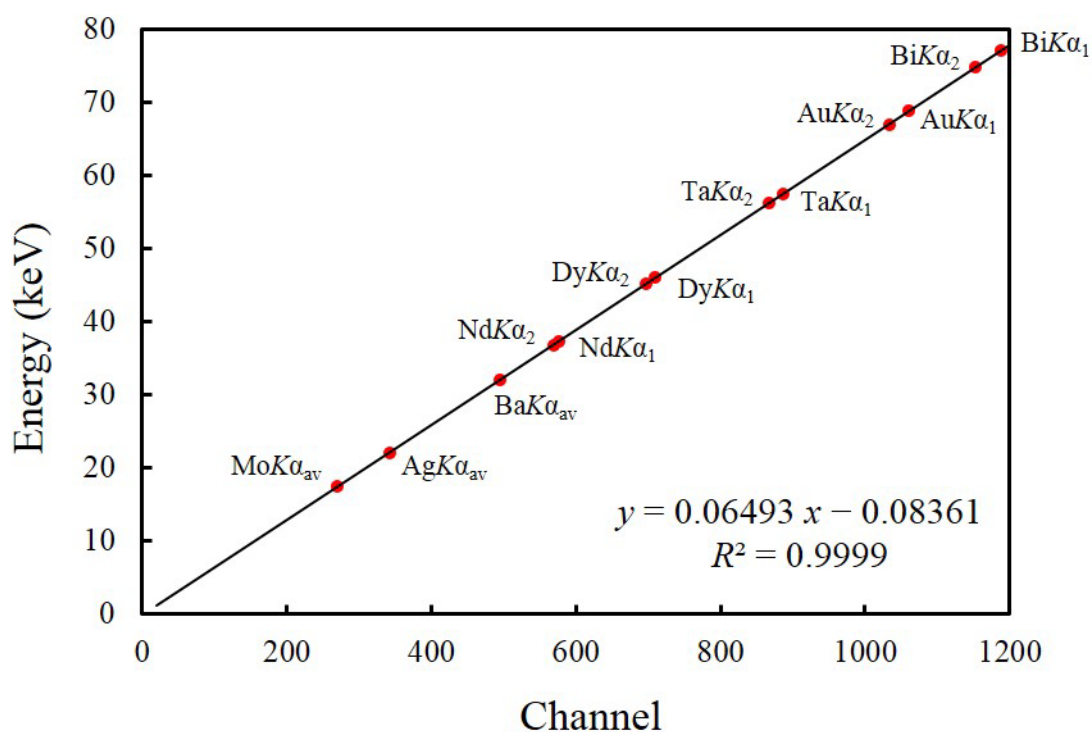


Figure 3–5. Calibration line for energy calculated from the characteristic X-rays of eight elements (Mo, Ag, Ba, Nd, Dy, Ta, Au, and Bi). The weighted average values ( $K\alpha_{av}$ ) were used for three elements (Mo, Ag, and Ba), because the peaks of  $K\alpha_1$  and  $K\alpha_2$  could not be separated.

### **3.2.4. SEM observations for the recovered samples**

To observe microtexture of the run products recovered from high pressure, I collected SEM images. Sample surfaces were coated with carbon using a carbon coater or 5 nm-thick osmium using an osmium coater (Figure 3–6). SEM observations were conducted using a scanning microscope (JSM-6610LA; JEOL). Osmium coating was thin enough to obtain Raman spectra from samples without removing coat.

Polymorphs of calcium carbonate on the fracture surfaces of recovered samples were identified from micro-Raman spectra after SEM observations. Raman spectra were obtained using a micro-Raman spectrometer equipped with a 50-cm single polychromator (500is; Chromex), a Si-based charge-coupled device (CCD) detector with  $1024 \times 128$  pixels (DU-401A-BR-DD; Andor Technology) electrically cooled to  $-70$  °C, and a 514.5 nm Ar<sup>+</sup> laser (543AP-A01; Melles Griot). The spatial resolution is estimated to be about 2  $\mu\text{m}$  in lateral directions.



Figure 3–6. Photograph of osmium coater.

### 3.3. Results and discussion

#### 3.3.1. Time-resolved X-ray diffraction

Figure 3–7 shows time-resolved XRD patterns during crystallization from ACC to calcite and vaterite obtained by energy-dispersive XRD method. Intensity was normalized by Au 111 because the intensity of incident beam at PF–AR beamlines decayed with time. The origin of time (Time = 0) in Figure 3–7 corresponds to the point just before the crystallization started. The intensities of diffraction peaks attributable to calcite and vaterite increased with increasing time. The cooccurrence of calcite and vaterite by applying pressure is consistent with previous experiments based on the recovered samples (see Chapter 2).

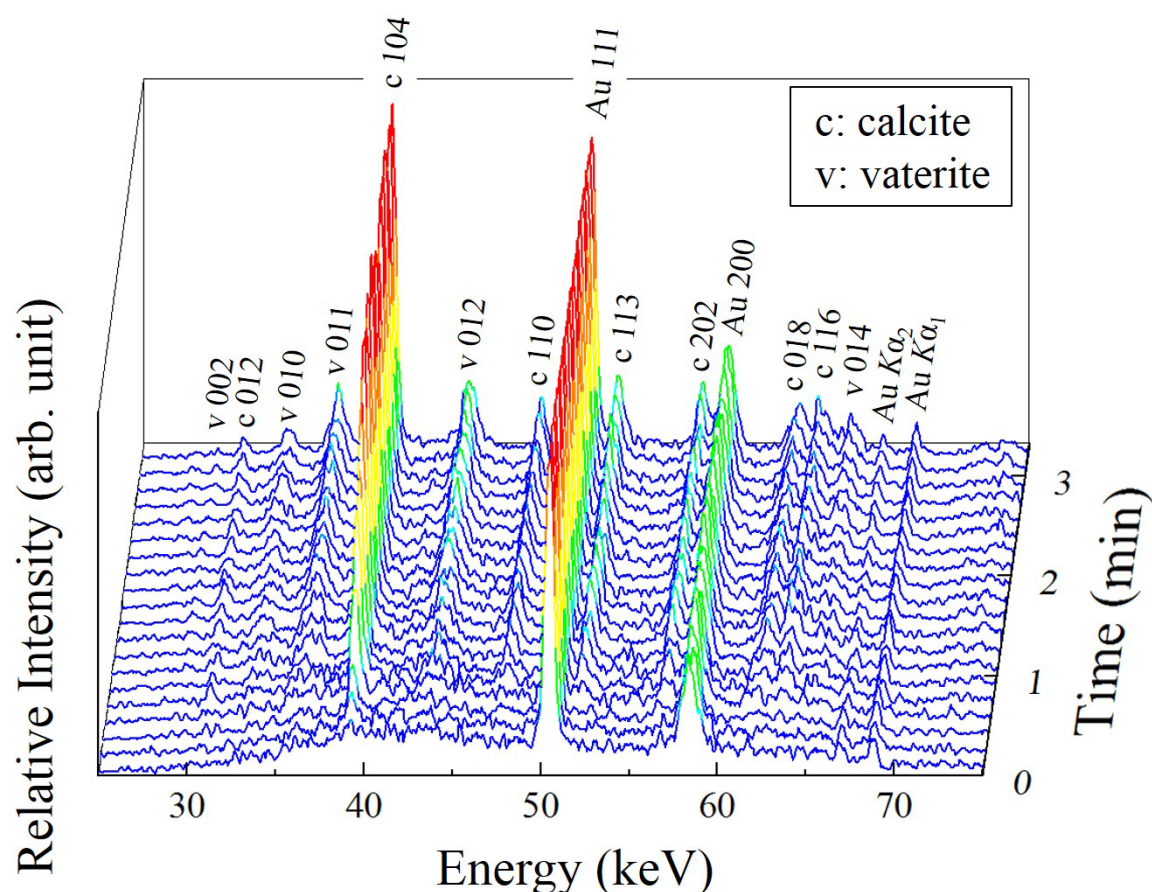


Figure 3–7. Time-resolved energy-dispersive XRD patterns of ACC sample with Au powder during pressure-induced crystallization from ACC to calcite and vaterite at room temperature. Intensity was normalized by the peak intensity of Au (111 reflection). Indices of vaterite are based on a structure model proposed by Kamhi (1963).

### 3.3.2. Estimation of pressure

In general, NaCl is a better pressure marker than Au because the bulk modulus of NaCl (23.84 GPa; Shanker et al., 1997) is smaller than that of Au (166.34(77) GPa; Akahama et al., 2002). However, the grain growth of NaCl would occur by addition of water dehydrated from ACC by applied pressure. Therefore, in this study, Au powder was used as a pressure marker during time-resolved XRD measurements because of its chemical stability. Figure 3–8 shows pressures calculated from each pressure marker at each press load. This figure indicates that Au mixed in ACC showed significantly different behavior from NaCl and Au in the first layer (see Figure 3–3 (b)). The difference in behaviors of Au pressure markers would be due to the large difference in bulk moduli of coexisting materials. The Au powder in NaCl powder would behave as in quasi-hydrostatic condition because of small bulk modulus of NaCl. On the other hand, although there is no report on the bulk modulus of ACC, it is expected that ACC has larger bulk modulus than NaCl judging from the bulk moduli of other crystalline phases of calcium carbonate: 73.46(27) GPa of calcite (Redfern and Angel, 1999), 73.1(22) GPa of aragonite (Ono et al., 2005), and 63.8(6) GPa of vaterite (described in Chapter 4 in this thesis). By annealing at higher temperature, it is expected to estimate more proper pressure. However, the cell could not be annealed in this study because ACC crystallizes to calcite by heating (Kojima et al., 1993; Koga et al., 1998; Ihli et al., 2014). Therefore, pressure during time-resolved measurements was estimated as follow. First, precise load was estimated from lattice volume of Au in ACC (the second layer) and from the extrapolated straight line (1) in Figure 3–8 (see green arrows in Figure 3–8). Then, the pressure was estimated from the extrapolated straight line (2) in Figure 3–8 (see an orange arrow in Figure 3–8). From these straight lines, the following equation was obtained:

$$P = \frac{0.013}{0.070} (P_{\text{Au}} + 1.1) - 0.23 \quad (3-1),$$

where  $P_{\text{Au}}$  is a pressure calculated from Au mixed in ACC. Figure 3–9 shows the variation of pressures estimated from Equation 3–1 during the time-resolved XRD measurement. Pressure increased with increasing press load, and dropped to about 0 GPa when the crystallization occurred at 0.36 GPa (time = 0). The crystallized pressure in this experiment was lower than

### Chapter 3. Kinetic observation of pressure-induced crystallization of ACC

that in Chapter 2 using ACC with similar water contents ( $x = 0.60$ ), which crystallized at 0.64 GPa. The difference in the crystallized pressure would be derived from experimental conditions, for example, time scale, rate of applied pressure, temperature, and so on.

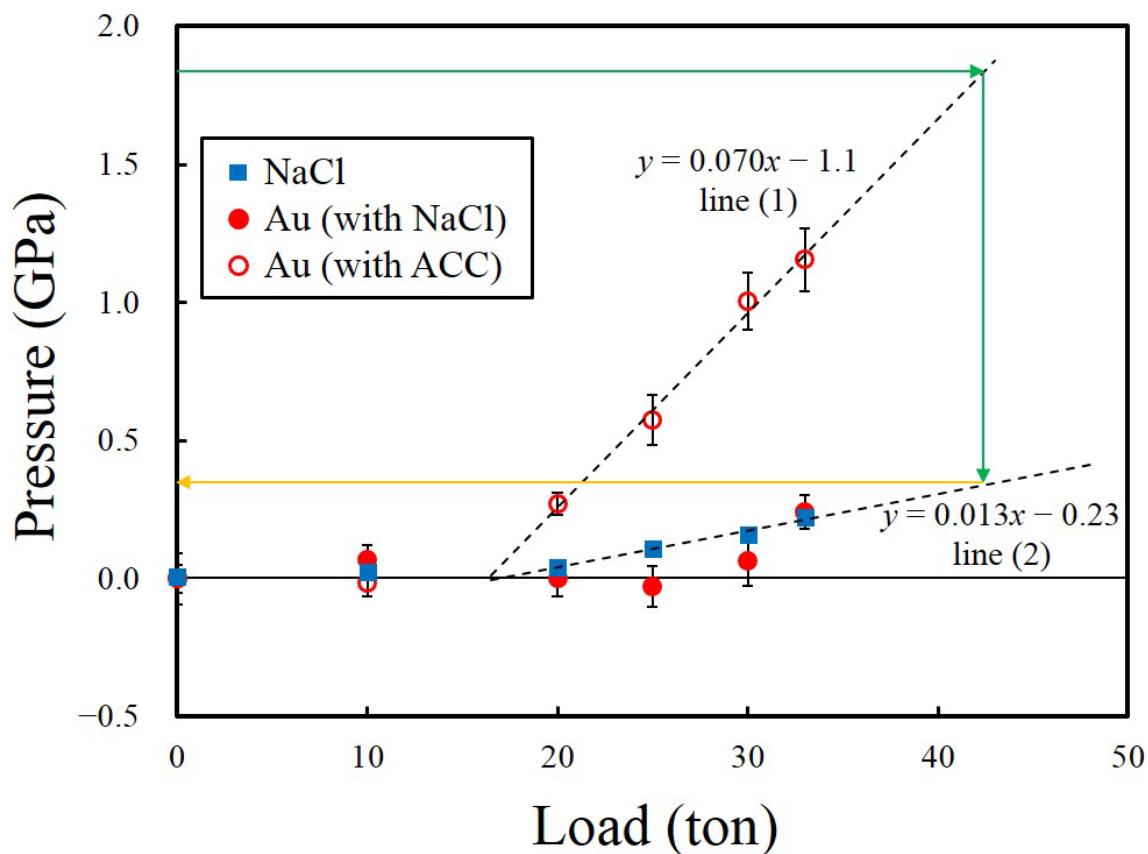


Figure 3–8. Pressure estimated from NaCl and Au at each load. Error bars of NaCl are smaller than the symbol sizes. Approximation straight lines (1) and (2) were obtained from the plot of Au with ACC and NaCl, respectively. These straight lines are drawn by the point at press load higher than 20 tons.

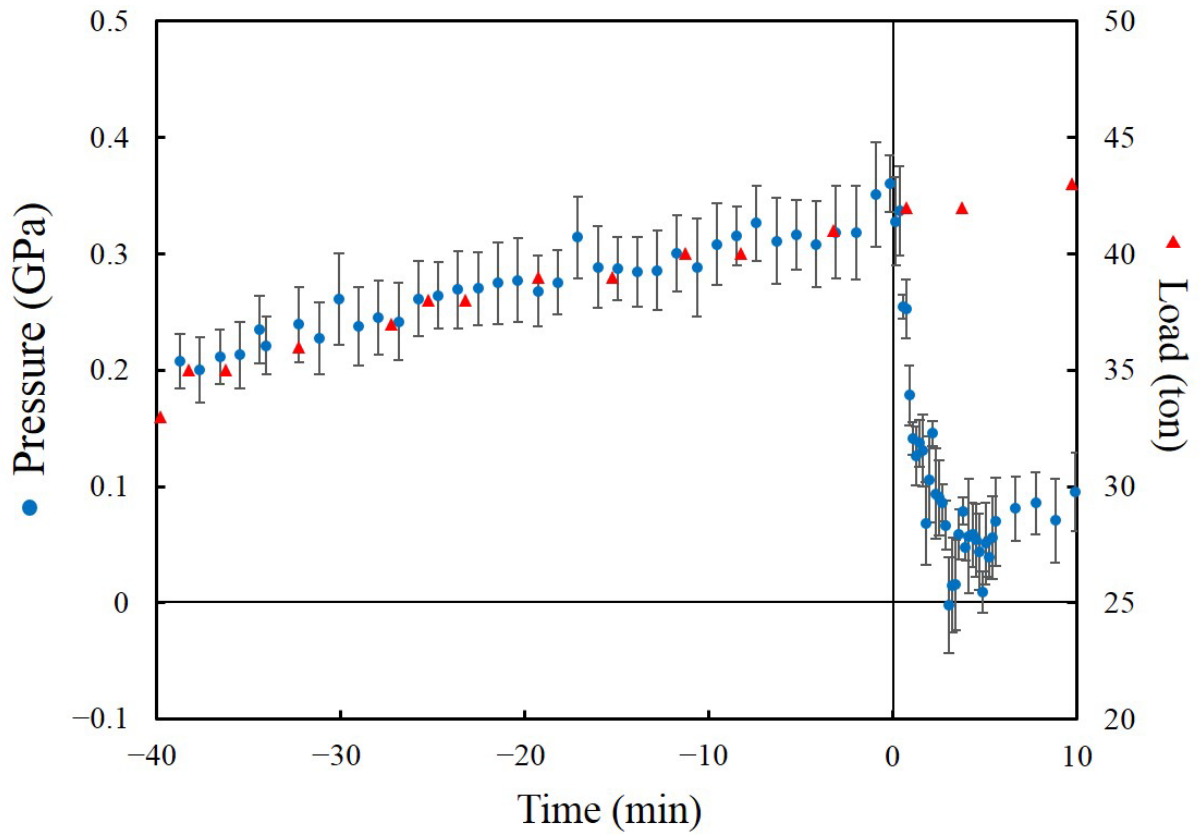


Figure 3-9. Variation of pressure estimated from Equation 3-1 and press load with time. The origin of time (Time = 0) in the figure is the same as that of Figure 3-7, corresponding to the point just before the crystallization started.

### 3.3.3. Kinetics of pressure-induced crystallization from ACC

Figure 3–10 shows the degree of transformation described in molar fraction at high pressure as a function of time. The pressure-induced crystallization from ACC to calcite and vaterite completed in about 3 min. Abundances of calcite and vaterite monotonically increased with increasing time. This result indicates that no notable transformation from vaterite to calcite occurred. The mechanism of pressure-induced crystallization from ACC was different from that of the sequential crystallization from ACC to vaterite and calcite in a supersaturated aqueous solution, following Ostwald's step rule (Tsuno et al., 2001; Rodriguez-Blanco et al., 2011; Bots et al., 2012). Moreover, Nielsen et al. (2014) reported that no direct transformation from ACC to calcite was observed in supersaturated solutions. The obtained results suggest the direct transformation from ACC to calcite, which implies that the formation of calcite occurred without direct involvement of a solution.

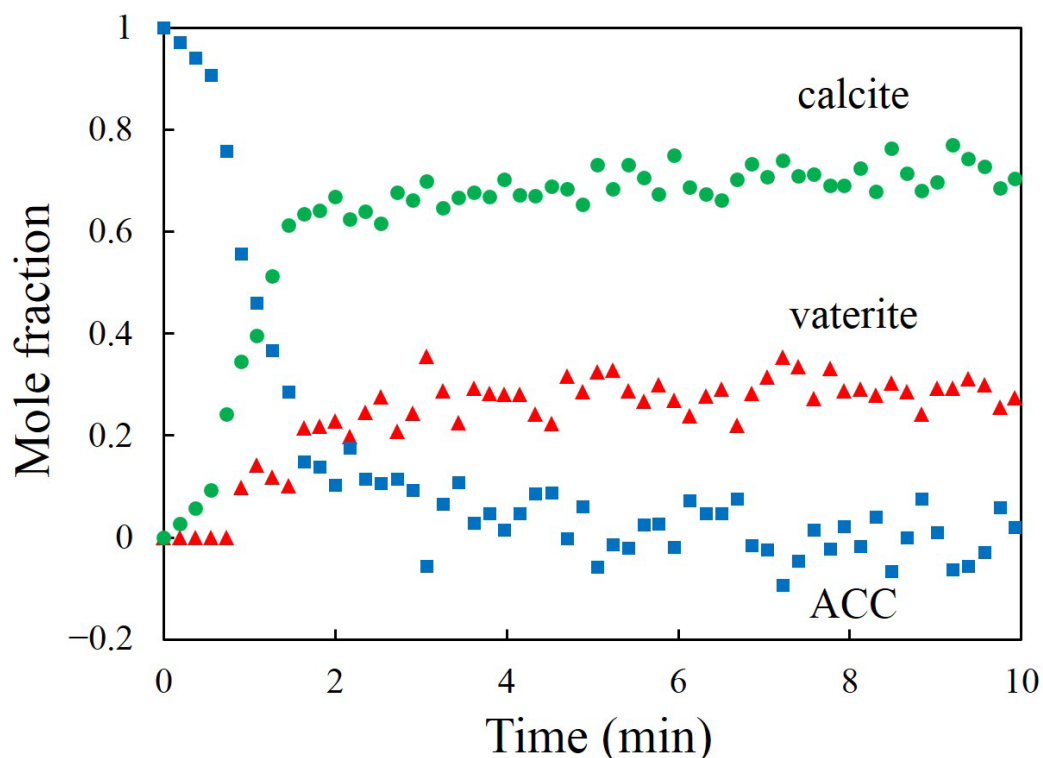


Figure 3–10. Degree of transformation determined from diffraction intensities of vaterite (010 reflection) and calcite (104 reflection) as a function of time. The ratio of calcite to vaterite was calculated using the calibration line described as Chapter 2. The mole fraction of ACC was estimated from the balance of vaterite and calcite.

### Chapter 3. Kinetic observation of pressure-induced crystallization of ACC

To understand the mechanism of pressure-induced crystallization from ACC, the present data were analyzed using Avrami model (Avrami, 1939). The Avrami equation is represented by the following equation:

$$V_t = 1 - \exp(-kt^n) \quad (3-2),$$

where  $V_t$  is the volume fraction at time  $t$ ,  $k$  is the rate constant, and  $n$ , (Avrami exponent) is a constant dependent on the nucleation and crystal growth process. In this study, the volume fraction  $V_t$  was estimated from the relative diffraction intensities at time  $t$  to the intensity at the end of reaction:

$$V_t = I_t/I_{\max} \quad (3-3).$$

The difference in the  $n$  value reflects the crystallization mechanism. For example, the larger  $n$  value means the crystal growth rate is higher than the nucleation rate. In other words, the larger  $n$  value shows nucleation-controlled process, and the lower  $n$  value shows growth-controlled process. Equation 3-2 can be deformed as the following equation:

$$\ln\{-\ln(1 - V_t)\} = \ln k + n \ln t \quad (3-4).$$

In plots of  $\ln\{-\ln(1 - V_t)\}$  vs.  $\ln t$ , the slope indicates the  $n$  value. Figure 3-11 shows the plots for the transformation to calcite and vaterite using the diffraction lines of the highest intensity, respectively. The obtained  $n$  values for calcite and vaterite are 1.8 and 1.4, respectively. The difference in the  $n$  values implies that the formation of calcite is more controlled by the nucleation process than that of vaterite and may result in a difference in the grain size and/or microtexture between calcite and vaterite.

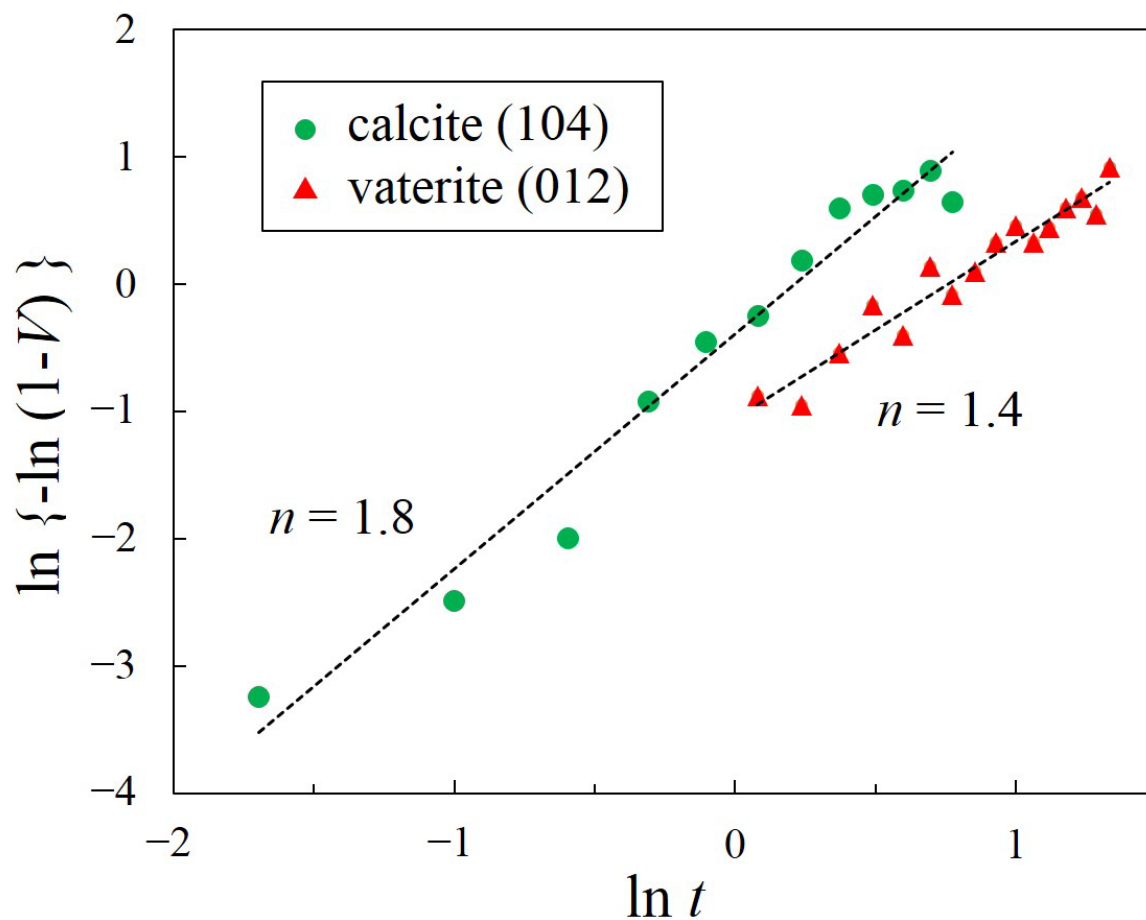


Figure 3-11. Plots of Avrami fitting for calcite (104 reflection) and vaterite (012 reflection) during pressure-induced crystallization from ACC.

### 3.3.4. Microtexture of the recovered samples

To investigate the relationship between polymorphs and its texture of the recovered sample, polymorph distribution on the fracture was determined by Raman mapping analysis (see Figure 3–12). Figure 3–13 shows two types of Raman spectra on the region shown in Figure 3–12. Strong peaks at 1075 and 1091  $\text{cm}^{-1}$  are attributable to the symmetric stretching vibration ( $\nu_1$ ) of carbonate group of vaterite, and a peak at 1085  $\text{cm}^{-1}$  is assignable to that of calcite. Polymorph identification was conducted using these peaks of  $\nu_1$ .

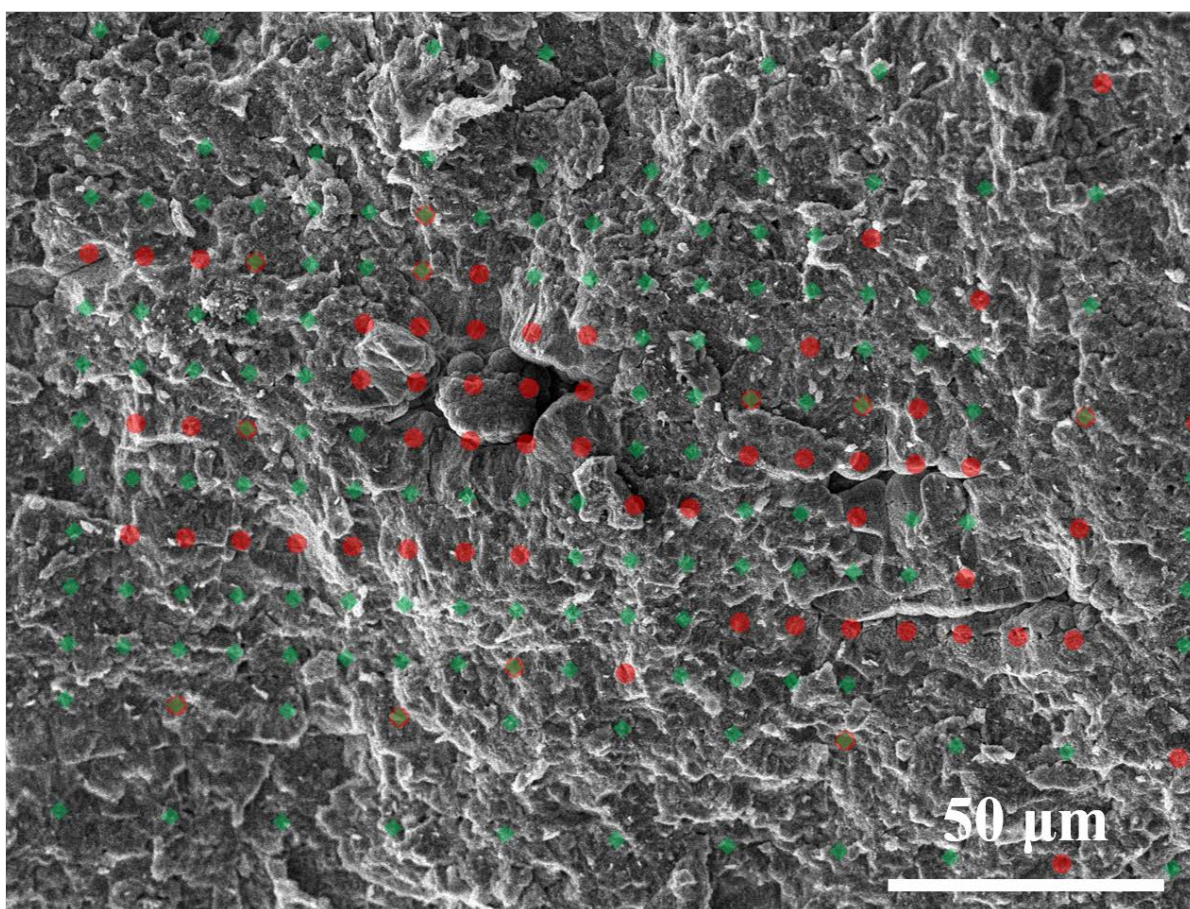


Figure 3–12. SEM image of a fracture surface of a recovered sample and its polymorph distribution determined by Raman spectroscopy. Red circles and green diamonds denote vaterite and calcite, respectively.

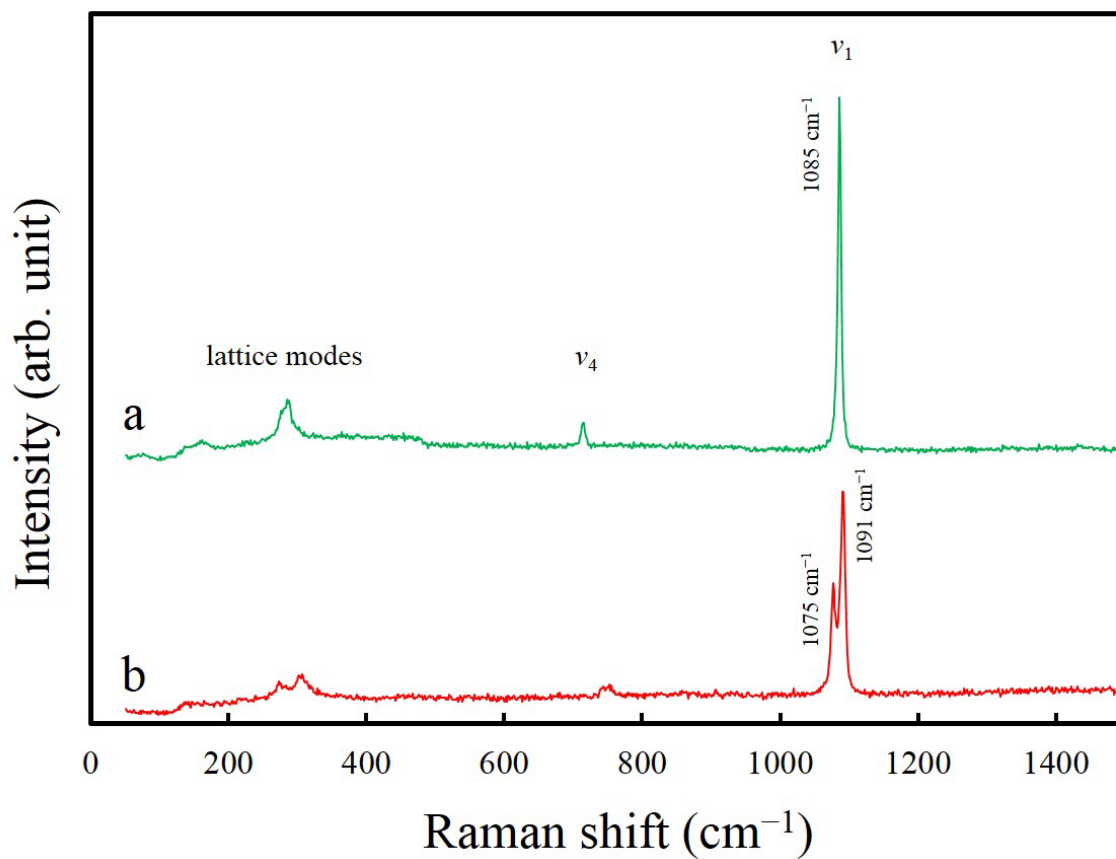


Figure 3–13. Representative Raman spectra obtained by Raman mapping on the region observed by SEM. One is attributable to calcite (a) and the other is assignable to vaterite (b). In addition, Raman spectra represented by the combination of these spectra were also obtained.

### *Chapter 3. Kinetic observation of pressure-induced crystallization of ACC*

Figure 3–12 represents that vaterite mainly distributes around cavities. It is noteworthy that the vacant cavities exist in the compressed sample. At high pressure, these cavities would be filled with fluid, which is dehydrated from ACC. This result suggests that the formation of vaterite deeply involved with dehydrated fluid. Moreover, vaterite distributing around cavities has the same texture as formed in a supersaturated solution (see Figure 3–14 (a) and (b)). This similarity also indicates that vaterite crystals formed in fluid. Vaterite crystals are also found along a vein-structure without cavities (see the center left of Figure 3–12). This vaterite implies that the vein-structure is a trace of fluid connecting cavities to each other.

On the other hand, calcite distributes throughout the sample and no local concentration was observed. Most of calcite crystals have spherical texture, which is different from the euhedral texture of calcite formed in a supersaturated solution and is the pseudomorph of the original ACC grains (see Figure 3–14 (c) and (d)). This result suggests that calcite crystallized directly from ACC. Moreover, euhedral crystals of calcite were also observed as minor structure around the cavities (see Figure 3–14 (e)). In general, it is known that calcite forms as euhedral crystals in a supersaturated solution (Figure 3–14 (f); Nielsen et al., 2014), which suggests that these euhedral calcite observed in this study grew in the dehydrated fluid. However, the formation of calcite from ACC or vaterite takes for longer time than this experimental time scale (e.g. Rodriguez-Blanco et al., 2011; Bots et al., 2012). Therefore, some euhedral calcite crystals observed by SEM observation would form in the dehydrated fluid after high-pressure experiment. Dehydration from ACC occurred with the transformation from ACC to calcite because calcite is an anhydrous mineral and any hydrate of calcium carbonate was not observed. This dehydrated water would be closely related to the formation of vaterite.

Figure 3–14 (a) and (c) show the SEM images focused on the surface texture of vaterite and calcite on the recovered run product, respectively. The grain sizes of vaterite and calcite were 100–200 nm. No significant difference in grain size was found between vaterite and calcite. However, grain sizes of calcite (see Figure 3–14 (c)) might be slightly larger than those of vaterite (see Figure 3–14 (a)). This observation is consistent with the result from Avrami fitting, which suggests the  $n$  value of calcite is larger than that of vaterite.

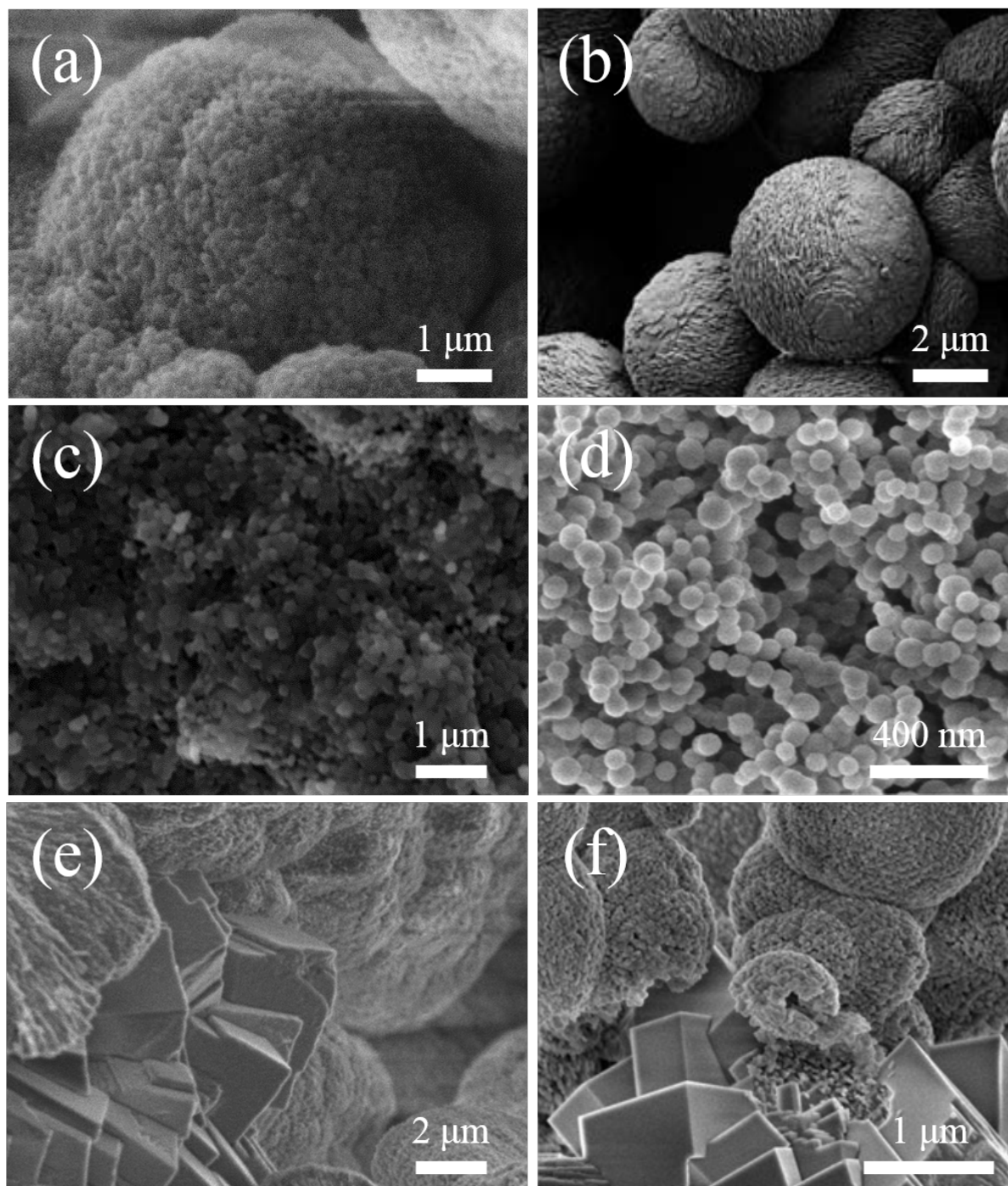


Figure 3–14. SEM images of a fracture surface of a recovered sample in this study and of calcium carbonates formed in supersaturated solutions reported by previous studies. (a) Aggregation of vaterite crystals distributing around cavities, (b) compared to vaterite growing in a supersaturated solution (Andreassen et al., 2012). (c) Spherical texture of calcite distributing throughout the sample, (d) compared to synthesized ACC (Rodriguez-Blanco et al., 2012). (e) Minor structure of euhedral calcite crystals distributing around cavities, (f) compared to euhedral calcite crystals transformed from vaterite in a supersaturated solution (Rodriguez-Blanco et al., 2012).

### **3.3.5. Mechanism of pressure-induced crystallization form ACC**

Vaterite was observed around cavities which were traces of a dehydrated fluid, and the texture of vaterite was the same as vaterite formed in a supersaturated solution. These observations mean that the formation of vaterite needs dehydrated fluid, which is consistent with the results from recovered experiments mentioned in Chapter 2, which suggests that ACC with higher H<sub>2</sub>O contents resulted in higher vaterite/calcite ratio than ACC with lower H<sub>2</sub>O contents. On the other hand, calcite crystals showed pseudomorph of ACC. This result suggests that the formation of calcite occurred by solid-solid phase transition from ACC. When calcite transformed from ACC, the dehydration occurred because calcite is an anhydrous mineral. Therefore, it is thought that the transformation from ACC to calcite occurred before vaterite formed. This suggestion is consistent with the time-resolved XRD observations showing the first appearance of calcite followed by vaterite crystallization (see Figure 3–7 and 3–10). Moreover, not all ACC crystallized to calcite. This implies that pressure distribution existed in the sample chamber and/or that the starting material consisted of the mixture of proto-calcite ACC and proto-vaterite ACC (Gebauer et al., 2010).

From the obtained results, I proposed the following model as pressure-induced crystallization mechanism. At first, a part of ACC crystallizes to calcite by solid-solid phase transition associating dehydration by applied pressure (Figure 3–15 from (a) to (b)). On the other hand, the formation of vaterite occurs in the fluid at the same process as the formation in a supersaturated solution (Figure 3–15 from (b) to (d)). Finally, the trace of the fluid forms cavities after high-pressure experiments (Figure 3–15 (e)). In pressure-induced crystallization, the crystallization from ACC to calcite and vaterite proceeds by such different mechanisms.

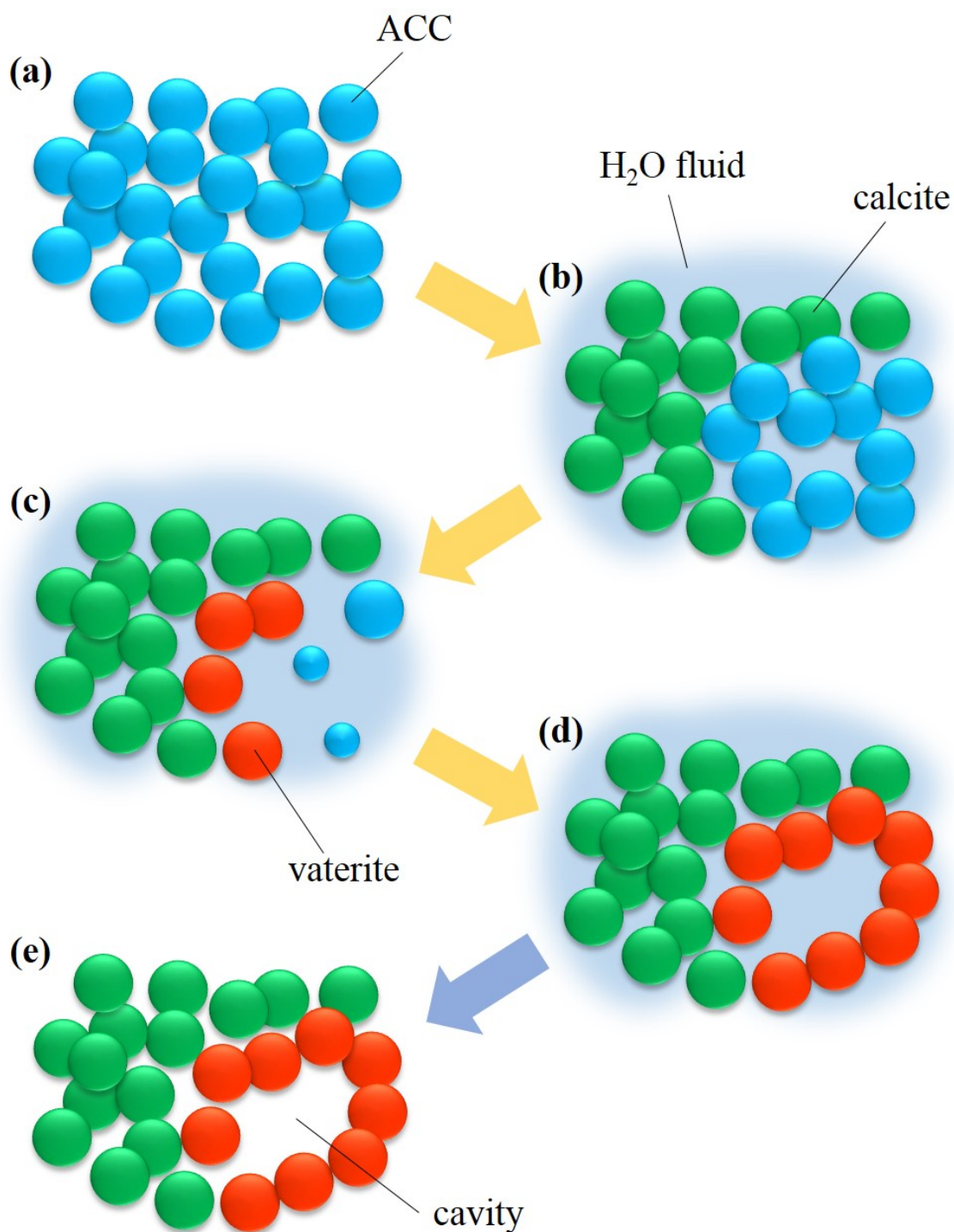


Figure 3–15. Schematic illustrations of the proposed mechanism model of pressure-induced crystallization pathway from ACC to calcite and vaterite.

### **3.4. Conclusion**

In this chapter, pressure-induced crystallization from ACC to calcite and vaterite was observed by in situ time-resolved XRD study. The experiments at relatively lower pressure (< 1 GPa) were achieved using a relatively large TEL of 10 mm for the second-stage anvils. Time-resolved measurements showed that the pressure-induced crystallization proceeded much faster than the crystallization in supersaturated solutions. Moreover, SEM images and Raman spectra of the samples recovered from high pressure indicate that the crystallization mechanisms of vaterite and calcite are different from each other. From the obtained results, I proposed a model of pressure-induced crystallization mechanism; calcite transforms from ACC by solid-solid phase transition associating with dehydration, and vaterite forms in supersaturated solution produced by the formation of calcite. This present study provides a new view of crystallization process of ACC, and may throw light on understanding the behavior of ACC in biomineralization and on the application of ACC in material science.

## References

- Akahama Y, Kawamura H, and Singh AK (2002) Equation of state of bismuth to 222 GPa and comparison of gold and platinum pressure scales to 145 GPa. *Journal of Applied Physics*, **92**, 5892–5897.
- Anderson OL, Isaak DG, and Yamamoto S (1989) Anharmonicity and the equation of state for gold. *Journal of Applied Physics*, **65**, 1534–1543.
- Andreassen JP, Beck R, and Nergaard M (2012) Biomimetic type morphologies of calcium carbonate grown in absence of additives. *Faraday Discussions*, **159**, 247–261.
- Avrami M (1939) Kinetics of Phase Change. I General Theory. *Journal of Chemical Physics*, **7**, 1103–1112.
- Bots P, Benning LG, Rodriguez-Blanco JD, Roncal-Herrero T, and Shaw S (2012) Mechanistic Insights into the Crystallization of Amorphous Calcium Carbonate (ACC). *Crystal Growth & Design*, **12**, 3806–3814.
- Chen J, Kikegawa T, Shimomura O, and Iwasaki H (1997) Application of an Imaging Plate to the Large-Volume Press MAX80 at the Photon Factory. *Journal of Synchrotron Radiation*, **4**, 21–27.
- Decker DL (1971) High-Pressure Equation of State for NaCl, KCl, and CsCl. *Journal of Applied Physics*, **42**, 3239–3244.
- Gebauer D, Gunawidjaja PN, Ko JYP, Bacsik Z, Aziz B, Liu L, Hu Y, Bergström L, Tai CW, Sham TK, Edén M, and Hedin N (2010) Proto-Calcite and Proto-Vaterite in Amorphous Calcium Carbonates. *Angewandte Chemie*, **49**, 8889–8891.
- Horikawa T, Suito K, Kobayashi M, and Onodera A (2001) Time-resolved X-ray diffraction study of C<sub>60</sub> at high pressure and temperature. *Physics Letters A*, **287**, 143–151.
- Ihli J, Wong WC, Noel EH, Kim YY, Kulak AN, Christenson HK, Duer MJ, and Meldrum FC (2014) Dehydration and crystallization of amorphous calcium carbonate in solution and in air. *Nature Communications*, **5**, 3169, doi:10.1038/ncomms4169.
- Inoue T, Yoshimi I, Yamada A, and Kikegawa T (2009) Time-resolved X-ray diffraction analysis of the experimental dehydration of serpentine at high pressure. *Journal of Mineralogical and Petrological Sciences*, **104**, 105–109.
- Kamhi SR (1963) On the Structure of Vaterite, CaCO<sub>3</sub>. *Acta Crystallographica*, **16**, 770–772.

### Chapter 3. Kinetic observation of pressure-induced crystallization of ACC

- Kawazoe T, Nishiyama N, Nishihara Y, and Irifune T (2010) Pressure generation to 25 GPa using a cubic anvil apparatus with a multi-anvil 6-6 assembly. *High Pressure Research*, **30**, 167–174.
- Koga N, Nakagoe Y, and Tanaka H (1998) Crystallization of amorphous calcium carbonate. *Thermochimica Acta*, **318**, 239–244.
- Kojima Y, Kawanobe A, Yasue T, and Arai Y (1993) Synthesis of Amorphous Calcium Carbonate and Its Crystallization. *Journal of the Ceramic Society of Japan*, **101**, 1145–1152.
- Nielsen MH, Aloni S, and De Yoreo JJ (2014) In situ TEM imaging of CaCO<sub>3</sub> nucleation reveals coexistence of direct and indirect pathways. *Science*, **345**, 1158–1162.
- Nishiyama N, Wang Y, Sanehira T, Irifune T, and Rivers ML (2008) Development of the Multi-anvil Assembly 6-6 for DIA and D-DIA type high-pressure apparatuses. *High Pressure Research*, **28**, 307–314.
- Ono S, Kikegawa T, Ohishi Y, and Tsuchiya J (2005) Post-aragonite phase transition in CaCO<sub>3</sub> at 40 GPa. *American Mineralogist*, **90**, 667–671.
- Redfern SAT, and Angel RJ (1999) High-pressure behaviour and equation of state of calcite, CaCO<sub>3</sub>. *Contributions to Mineralogy and Petrology*, **134**, 102–106.
- Rodriguez-Blanco JD, Shaw S, and Benning LG (2011) The kinetics and mechanisms of amorphous calcium carbonate (ACC) crystallization to calcite, *via* vaterite. *Nanoscale*, **3**, 265–271.
- Rodriguez-Blanco JD, Shaw S, Bots P, Roncal-Herrero T, and Benning LG (2012) The role of pH and Mg on the stability and crystallization of amorphous calcium carbonate. *Journal of Alloys and Compounds*, **536S**, S477–S479.
- Shanker J, Kushwah SS, and Kumar P (1997) Equation of state and pressure derivatives of bulk modulus for NaCl crystal. *Physica B*, **239**, 337–344.
- Tsuno H, Kagi H, and Akagi T (2001) Effects of Trace Lanthanum Ion on the Stability of Vaterite and Transformation from Vaterite to Calcite in an Aquatic System. *Bulletin of the Chemical Society of Japan*, **74**, 479–486.



## **Chapter 4.**

**Pressure response of vaterite: in situ observation at high  
pressure by powder X-ray diffraction and Raman  
spectroscopy**

## **4.1. Introduction**

Vaterite, a metastable phase of  $\text{CaCO}_3$ , is a rare mineral occurring as biominerals and abiogenic minerals. Several studies reported the occurrences of vaterite in geological minerals (Cole and Kroone, 1959; Wehrmeister et al., 2010) and biominerals (Gauldie et al., 1997; Wehrmeister et al., 2010). Because of its metastability, vaterite is known as a precursor material in precipitations of more stable  $\text{CaCO}_3$  polymorphs: calcite and aragonite (Ogino et al., 1987).

Historically, for the crystal structure of vaterite, two structure models with hexagonal and orthorhombic symmetries have been proposed (Olshausen, 1925; Meyer, 1959, 1969; Kamhi, 1963). The crystal structure of vaterite has been debated for a long time because it is difficult to obtain large and pure single crystals of vaterite (Kabalah-Amitai et al., 2013). Moreover, it is thought that carbonate ions are disordered in vaterite structure (Kamhi, 1963; Wang and Becker, 2009). Recently, an orthorhombic fully ordered structural model was proposed by Le Bail et al. (2011). Demichelis et al. (2013) proposed a new vaterite structure having the lowest energy using first-principles calculations. Kabalah-Amitai et al. (2013) reported that vaterite comprises of at least two crystallographic structures that are mutually interspersed: a major structure with hexagonal symmetry and a minor unknown structure.

The infrequency of vaterite as a natural mineral and the indetermination of crystal structure of vaterite may result in no report about pressure response of vaterite. As described in Chapter 2, the vaterite/calcite ratio decreased with increasing applied pressure, suggesting a possibility of the transition from vaterite to calcite by applying pressure in pressure-induced crystallization of ACC. Although in situ X-ray diffraction study and the observations of microtexture indicate that vaterite and calcite crystallized from ACC with different process simultaneously (described in Chapter 3), the pressure response of vaterite should be clarified. Moreover, the pressure response of vaterite might provide some clues to understand metastable materials under high pressure. Therefore, this study investigated the high-pressure behavior of vaterite by powder X-ray diffraction and Raman spectroscopy using diamond anvil cells (DACs).

## 4.2. Experimental procedures

### 4.2.1. Synthesis of vaterite

Vaterite powder sample was synthesized using a lower supersaturated solution than that used for the synthesis of ACC as described in Chapter 2. Two aqueous solutions, 250 mL of 60 mM  $\text{CaCl}_2$  and 250 mL of 60 mM  $\text{NaHCO}_3$ , were kept at 30 °C. These solutions were mixed in a 500 mL plastic bottle, and the mixed solution was stirred for 10 min in a water bath maintained at 30 °C. After stirring, the mixed solution was filtered using an aspirator and a membrane filter with a pore size of 0.45  $\mu\text{m}$ , washed by pure water kept at 30 °C, and dried at about 130 °C. Synthesized sample was identified as vaterite from powder X-ray diffraction (XRD) pattern (see Figure 4–1) using an X-ray diffractometer (30 kV, 15 mA,  $\text{CuK}\alpha$ , Miniflex II; Rigaku Corp.) and thermogravimetry (TG) analysis using a thermal analysis instrument (TG-8120; Rigaku Corp.).

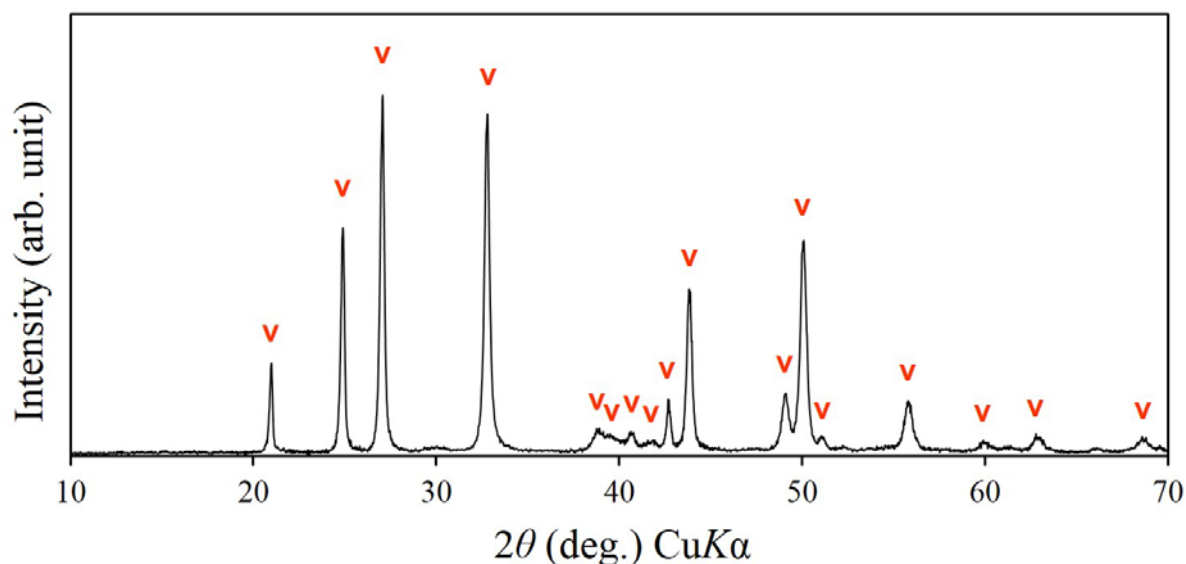


Figure 4–1. XRD pattern of synthesized vaterite. ‘v’ denotes peak positions of vaterite.

### 4.2.2. Setup for high-pressure experiments

High-pressure experiments were conducted using DACs (see Figure 4–2) with flat culet diamond anvils having 600  $\mu\text{m}$  of culet diameter. A stainless steel gasket (SUS 301) with initial thickness of 200  $\mu\text{m}$  was pre-indented to 100  $\mu\text{m}$  and a hole of 250  $\mu\text{m}$  in diameter was made on the center. Powder sample of vaterite was mounted into the gasket hole. Tiny ruby crystals were also mounted with sample as a pressure marker using a ruby fluorescence technique. Helium gas was used as a pressure-transmitting medium to achieve a quasi-hydrostatic high-pressure condition (Zha et al., 2000). Helium gas was introduced into the sample hole using a gas-loading system operating with gas pressure of 180 MPa at National Institute for Materials Science (NIMS) in Tsukuba, Japan (Takemura et al., 2001). An initial pressure of approximately 0.5 GPa was then applied. Pressure was increased up to 14 GPa, and XRD patterns and Raman spectra were obtained at each pressure point. The pressure increment and decrement during compression and decompression were approximately 0.3–1 GPa. Pressure was determined from the wavelength of the ruby *R1* fluorescence line by the following equation (Mao et al., 1986; Zha et al., 2000):

$$P = 1904 \times \{(\lambda/\lambda_0)^{7.715} - 1\}/7.715 \quad (4-1),$$

where  $P$  is pressure in GPa, and  $\lambda_0$  and  $\lambda$  are the wavelength values of the *R1* line in nm at ambient pressure and high pressure, respectively.

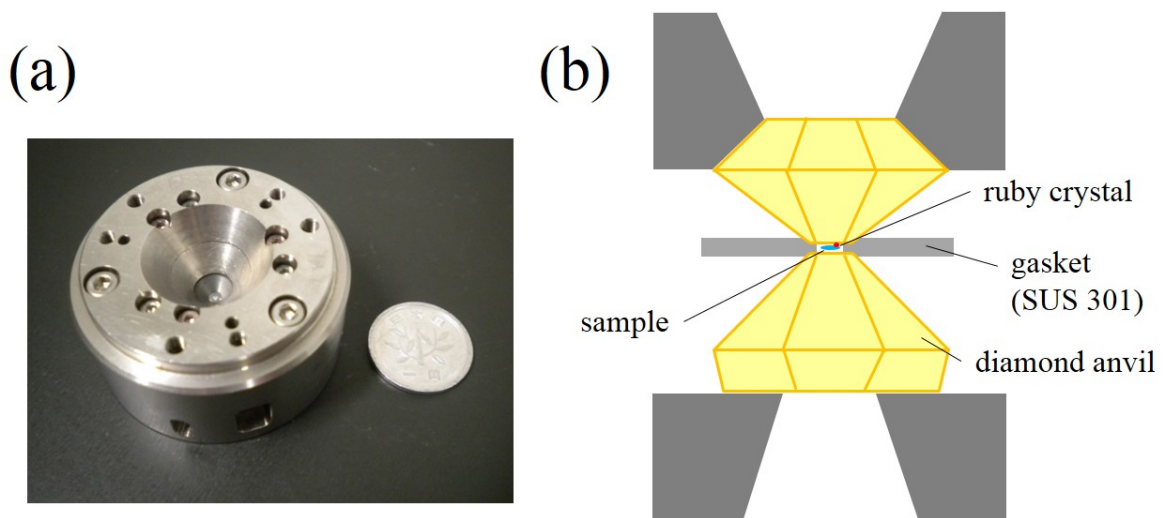


Figure 4–2. (a) Photograph of a DAC, and (b) cross section of the cell assembly.

### 4.2.3. Powder X-ray diffraction

Angle-dispersive XRD experiments were conducted at the synchrotron beamline of BL-18C in the Photon Factory, KEK (Figure 4-3). A monochromated incident X-ray with the energy of 20 keV (about 0.6 Å in wavelength) was collimated to a diameter of 100 μm, and was directed to samples in DACs. Each XRD pattern was collected using an imaging plate (IP) detector for exposure time of 10 min at room temperature. The X-ray wavelength and pixel sizes of the IP were calibrated using diffraction patterns of CeO<sub>2</sub>. The camera length was calibrated from diffraction peaks of the vaterite sample in DACs at the initial pressure before high-pressure experiments. The two-dimensional XRD images on the IPs were integrated into one-dimensional patterns as a function of  $2\theta$  using the software IPAnalyzer (Seto et al., 2010; Seto, 2012). The lattice constants of observed phases were obtained using the Rietveld structural refinement program GSAS with EXPGUI (Larson and Von Dreele, 1994; Toby, 2001).

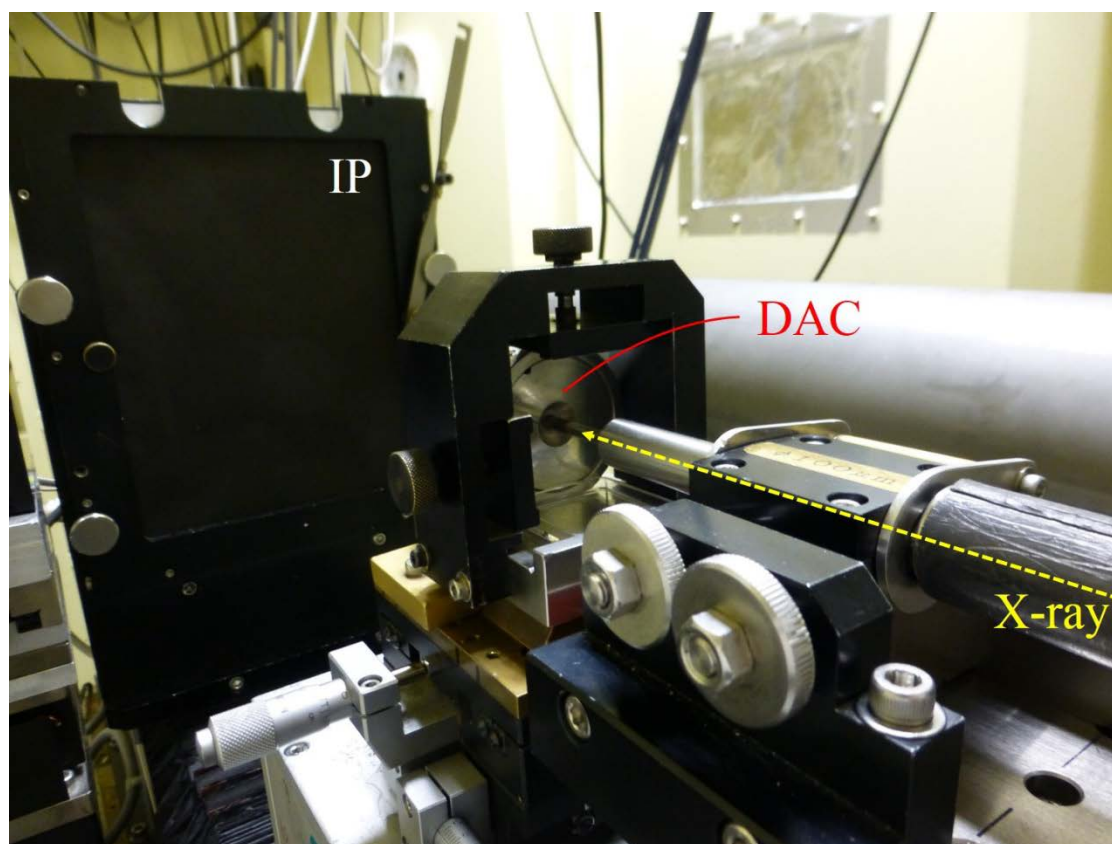


Figure 4-3. Photograph of experimental setup for in situ observation at high pressure at the beamline of BL-18C in the Photon Factory. Diffracted X-ray from samples in DACs was detected on the IP.

#### **4.2.4. Raman spectroscopy**

Raman spectra of vaterite at high pressure were obtained in the frequency region (150–1500  $\text{cm}^{-1}$ ) including the  $\text{CO}_3^{2-}$  stretching vibration mode and lattice modes. A micro-Raman spectrometer consisted of a 50-cm single polychromator (500is; Chromex), an optical microscope (BX60; Olympus Optical Co. Ltd.), and a Si-based charge-coupled device (CCD) detector with 1024×128 pixels (DU-401A-BR-DD; Andor Technology) electrically cooled to  $-70$  °C. Excitation was provided by 514.5 nm emission of an  $\text{Ar}^+$  laser (543-AP-A1; Melles Griot) operated at 50 mW power on the target sample surface. Each Raman spectrum was obtained for 60 s at room temperature.

Moreover, Raman spectra of calcite at high pressure were also measured under the same conditions as vaterite. Powder reagent of calcite (Wako Pure Chemical Industries Ltd.) was used in the comparison experiments.

### 4.3. Results and discussion

#### 4.3.1. X-ray diffraction patterns at high pressure with compression

Representative XRD patterns obtained at high pressure with compression are shown in Figure 4-4. Diffraction patterns below 4.7 GPa indicate no phase transition of vaterite. At 4.7 GPa, three main peaks of vaterite ( $2\theta \approx 10, 11, \text{ and } 13^\circ$  shown by orange-shaded regions in Figure 4-4) split into two peaks, respectively. In addition, weak peaks at about  $12^\circ$  in  $2\theta$  (green-shaded region in Figure 4-4) appeared and became prominent gradually with increasing pressure. These peaks were assignable to calcite III (Merlini et al., 2012). Except for the split peaks of vaterite and the appearance of calcite III, the ambient-pressure phase of vaterite remained below 8.7 GPa. In Figure 4-4, these peaks assignable to vaterite together with split peaks are denoted by blue 'v' symbols. The appearance of unknown phase having split peaks and calcite III indicates pressure-induced phase transition of vaterite. At 8.0 GPa, new peaks denoted by diamond symbols in Figure 4-4 appeared instead of the disappearance of peaks assigned by blue 'v' symbols, which implies the additional phase transition. The peaks appearing at 8.0 GPa were observed until 13.8 GPa. However, additional diffraction peaks appeared around  $20^\circ$  in  $2\theta$  (purple asterisks in Figure 4-4), suggesting the formation of coarse grains derived from another pressure-induced phase transition.

In following sections, I discussed about several phase transitions of vaterite and related phases observed from XRD patterns.

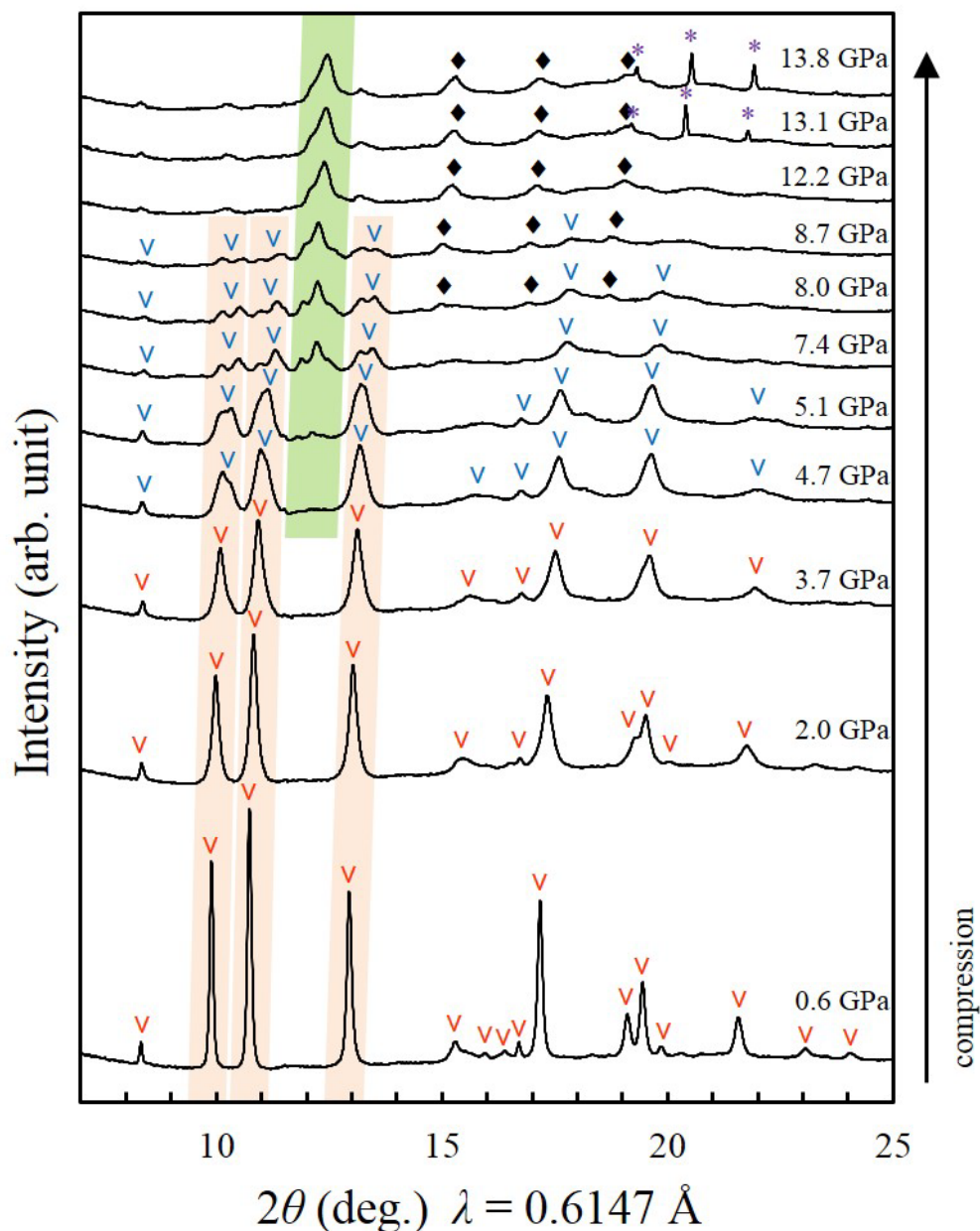


Figure 4-4. Representative XRD patterns at high pressure with compression. The intensity has been normalized to the same measurement time. ‘v’ and ‘v’ denote the peaks of the ambient-pressure phase of vaterite and the combination of split peaks and residue of vaterite, respectively. The orange-shaded regions indicate three main peaks of vaterite. The green-shaded region means the appearance of the highest intensity peaks of calcite III. New feature observed at higher pressures than 8.0 GPa and 13.1 GPa are denoted by black-solid diamonds and purple asterisks, respectively.

### 4.3.2. Determination of unit-cell parameters and bulk moduli

The diffraction patterns observed at pressures higher than 4.7 GPa, (denoted by blue ‘v’ symbols in Figure 4–4), except for the appearance of calcite III, were similar to that of vaterite at ambient pressure. This similarity suggests the structural affinity between this observed high-pressure phase and vaterite. Two symmetries with hexagonal and orthorhombic have been proposed as the crystal structure of vaterite. In the case of orthorhombic symmetry, several diffraction peaks are represented by the combination of two peaks with similar  $d$ -spacing. The crystal structure model with orthorhombic symmetry can reproduce the split of diffraction peaks observed at 4.7 GPa. In this study, the unit-cell parameters of vaterite were refined using the *Ama2* model recently proposed by Le Bail et al. (2011) shown in Figure 4–5. However, diffraction intensities could not be reproduced by the model because of coexisting at least two different structure and/or disordering of CO<sub>3</sub> group (Kabalah-Amitai et al., 2013). For this reason, atomic coordinates were fixed and only unit-cell parameters were refined in this study.

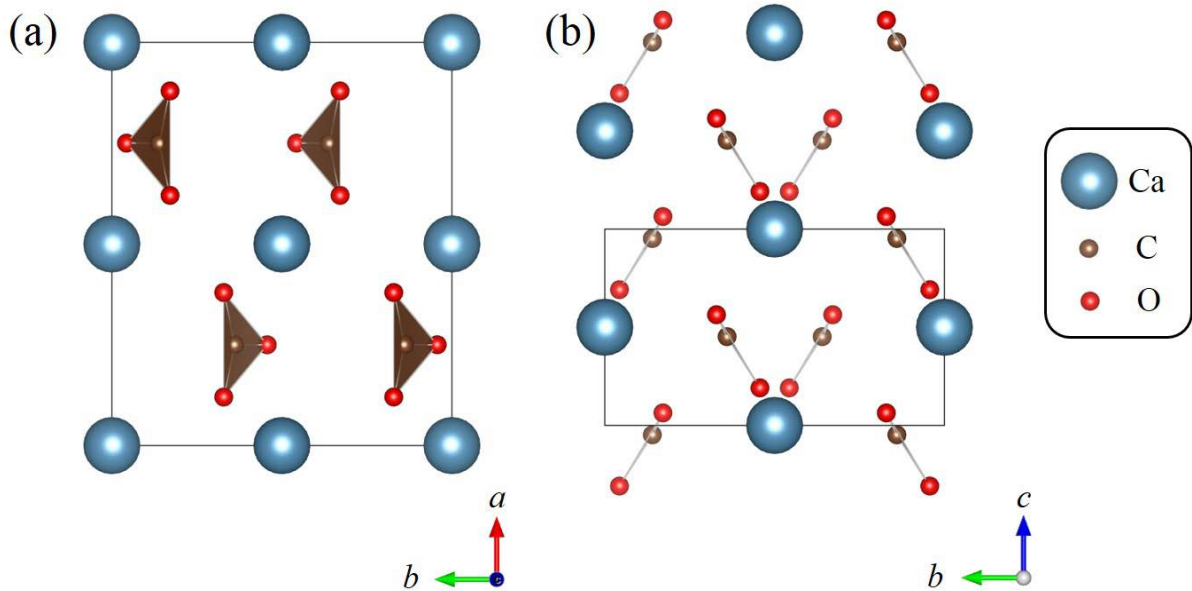


Figure 4–5. Crystal structure model of vaterite (*Ama2*) proposed by Le Bail et al. (2011): (a) from the  $c$ -axis, and (b) direct to the  $a$ -axis. Rectangles represent a unit cell.

## Chapter 4. Pressure response of vaterite

Figure 4–6 shows axial compressibility of vaterite obtained using Le Bail’s structure model. Up to 3.7 GPa, the *a*-axis of vaterite was less compressible than either the *b*-axis or *c*-axis. This contrast is explained by the fact that the *a*-axis is parallel to the planar CO<sub>3</sub><sup>2-</sup> ions (see Figure 4–5 (b)), resulting from incompressible C–O covalent bonds compared with compressible Ca–O ionic bonds. This is the same behavior as those of calcite (Redfern and Angel, 1999) and aragonite (Martinez et al. 1996).

Around 4.7 GPa, the compression data changed discontinuously: the *a*-axis length increased, while that of the *c*-axis decreased. Moreover, the *a*-axis became more compressible and the *b*-axis became less compressible at pressures higher than 4.7 GPa. This discontinuous change in the unit cell parameters and compression behaviors suggests the occurrence of a pressure-induced phase transition of vaterite at 3.7–4.7 GPa. Hereinafter, the initial phase appearing at lower pressures from ambient pressure to 4.7 GPa and the high-pressure phase with split diffraction peaks are denoted, respectively, as vaterite I and vaterite II.

In the pressure range from 4.7 to 8.7 GPa, the relative intensity of diffraction peaks assignable to vaterite II decreased concomitantly with increasing pressure (see Figure 4–4). It finally almost disappeared until about 9 GPa. In contrast, the diffraction intensity of calcite III increased up to 9 GPa synchronized with decreasing that of vaterite. These changes suggest that calcite III was transformed from the high-pressure phase of vaterite (vaterite II).

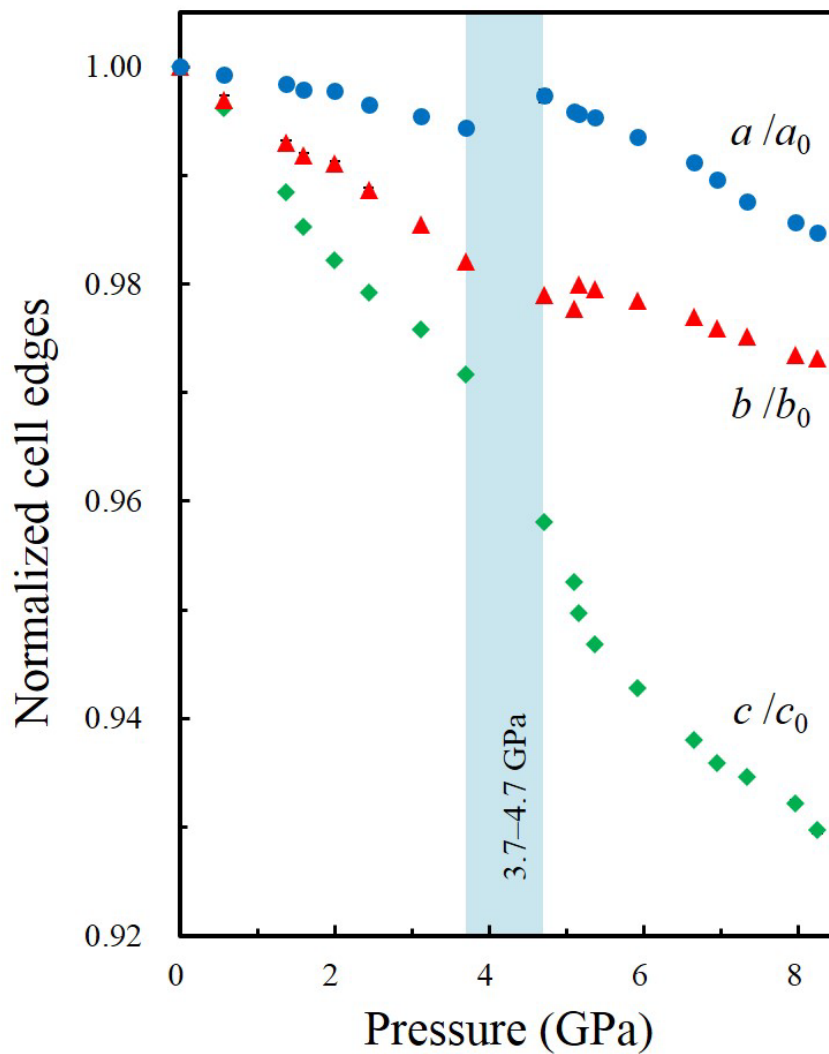


Figure 4–6. Axial compressibility of vaterite normalized to the ambient pressure. Error bars are smaller than the symbol sizes. The phase transition from vaterite I to vaterite II occurred at pressures represented by blue-shaded region from 3.7 to 4.7 GPa.

## Chapter 4. Pressure response of vaterite

Unit-cell volumes of vaterite I and vaterite II at each pressure are portrayed in Figure 4-7. The bulk modulus ( $K_{T0}$ ) was calculated based on the changes of cell constants of vaterite using the third-order Birch–Murnaghan equation of state:

$$P = \frac{3}{2}K_{T0} \left\{ \left( \frac{\rho}{\rho_0} \right)^{\frac{7}{3}} - \left( \frac{\rho}{\rho_0} \right)^{\frac{5}{3}} \right\} \left[ 1 + \frac{3}{4}(K_{T0}' - 4) \left\{ \left( \frac{\rho}{\rho_0} \right)^{\frac{2}{3}} - 1 \right\} \right] \quad (4-2),$$

where  $P$  is pressure,  $\rho_0$  and  $\rho$  are the density at ambient pressure and at high pressure, respectively, and  $K_{T0}'$  is the first derivative of  $K_{T0}$  with respect to pressure. When  $K_{T0}'$  is fixed to 4, the last term of Equation 4-2 can be ignored.  $K_{T0, \text{vaterite I}}$  was  $63.8 \pm 0.6$  GPa when  $K_{T0}'$  was fixed to 4. This value was notably lower than those of calcite and aragonite reported from earlier studies (see Table 4-1). Extrapolation of the fitted line for vaterite I shows significant upshift from the observations at 4.7 GPa and higher pressure. This relation suggests that vaterite II is a more compressible phase than vaterite I. The bulk modulus of vaterite II ( $K_{T0, \text{vaterite II}}$ ) was  $51.1 \pm 1.8$  GPa;  $V_0$  was  $252.6 \pm 0.8 \text{ \AA}^3$  when  $K_{T0}'$  was fixed to 4.

Vaterite II is more compressible than vaterite I. Moreover, no significant volume discontinuity was observed upon phase transition from vaterite I to vaterite II, which suggests a second-order phase transition (see Figure 4-7). This relation of vaterite I and vaterite II is similar to that of calcite I and calcite II; calcite II is also more compressible than calcite I (Vo Thanh and Lacam, 1984; Redfern, 2000), and the phase transition from calcite I to calcite II also has the characteristics of a second-order transition with no volume discontinuity (Merrill and Bassett, 1975; Redfern, 2000; Merlini et al., 2014). Calcite II can be described as distorted calcite I, with a lowering of symmetry involving the rotation of carbonate groups and the small displacement of calcium atoms (see Figure 1-3; Merrill and Bassett, 1975; Merlini et al., 2014). The results of this study suggest that vaterite II could be described as a distortion of vaterite I in the same manner as calcite II.

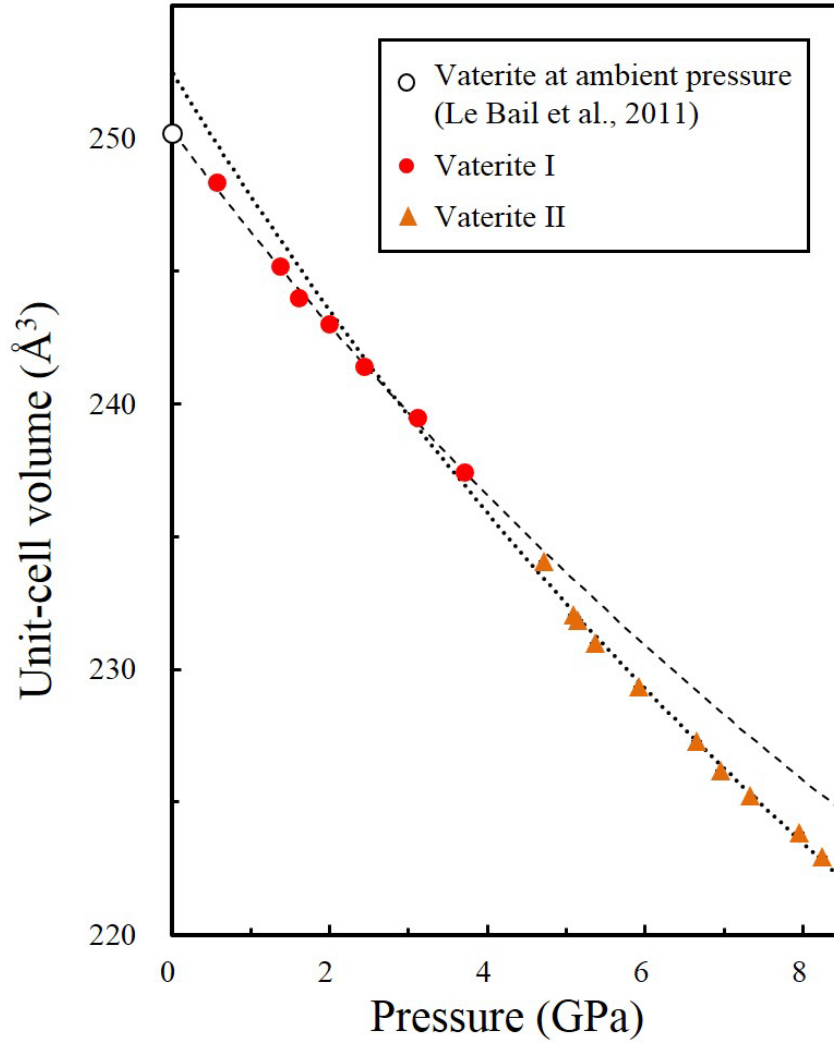


Figure 4–7. Unit-cell volume of vaterite I and II under high pressure. Error bars are smaller than the symbol size.

Table 4–1. Bulk moduli of  $\text{CaCO}_3$  polymorphs

polymorphs	$K_0$ (GPa)	$K_0'$	Method (pressure medium)	Reference
vaterite I	$63.8 \pm 0.6$	4	DAC (He)	This work
vaterite II	$51.1 \pm 0.6$	4		
calcite I	$69.5 \pm 2.1$	4	DAC (silicone oil)	Fiquet et al. (1994)
	$73.46 \pm 0.27$	4	DAC (methanol:ethanol)	Redfern and Angel (1999)
calcite III	$93.2 \pm 1.9$	4	DAC (silicone oil)	Fiquet et al. (1994)
aragonite	$64.81 \pm 3.48$	4	multi-anvil (boron epoxy)	Martinez et al. (1996)
	$73.1 \pm 2.2$	4	DAC (NaCl)	Ono et al. (2005)
	$68.9 \pm 1.4$	–	Brillouin spectroscopy	Liu et al. (2005)

### 4.3.3. High-pressure phases of vaterite at pressures higher than 8 GPa

At pressures higher than 8.0 GPa, weak and broad diffraction peaks denoted by solid diamonds in Figure 4–4 were observed. These diffraction peaks cannot be explained by calcite III and “unknown features” in a high-pressure experiment of calcite reported by Fiquet et al. (1994). Moreover, a peak at approximately  $8.3^\circ$  in  $2\theta$ , which is corresponding to the 200 reflection of vaterite structure provided by Le Bail et al. (2011), exists in all diffraction patterns. The variation of the peak is shown in Figure 4–8, and two discontinuous changes were observed. The first discontinuous change at pressures between 3.7 and 4.7 GPa suggests the phase transition from vaterite I to vaterite II as described in previous section. The second one at 8.7 GPa also suggests another phase transition from vaterite II to a new phase. Hereinafter, this new phase that appeared around 8.7 GPa is denoted as vaterite III.

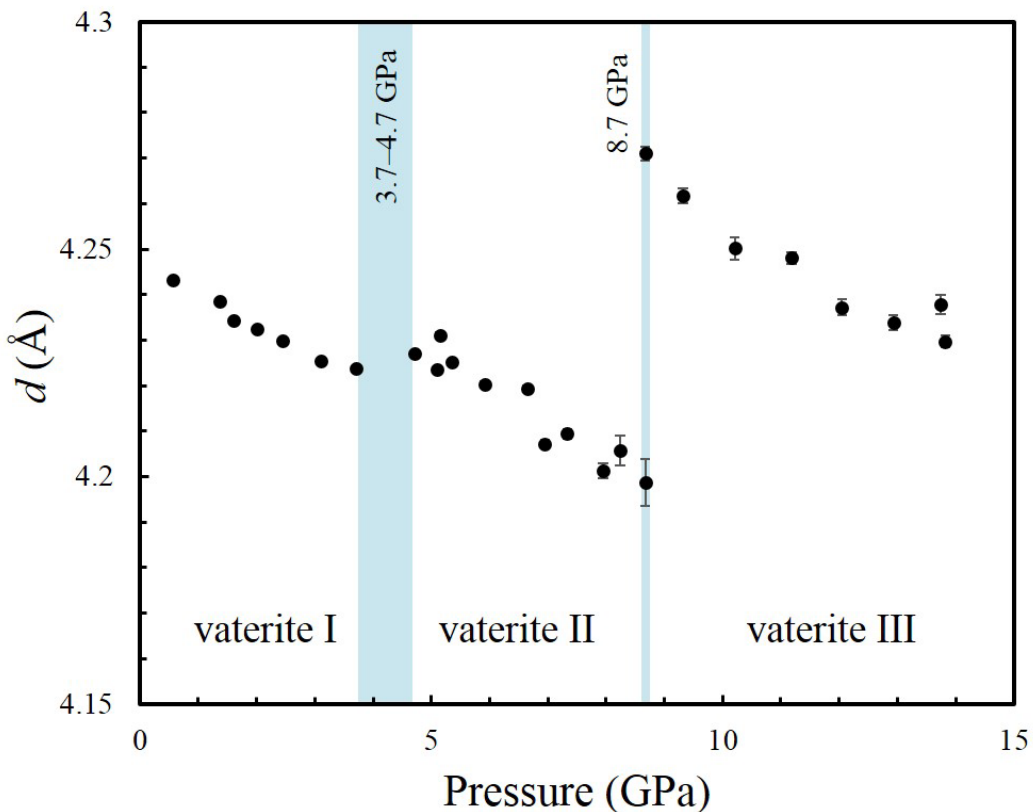


Figure 4–8. Variation of  $d$ -spacing corresponding to a reflection  $2\theta \approx 8.3^\circ$  with increasing pressure. At pressures lower than 4 GPa, the peak is attributable to the 200 of vaterite I. The phase transitions from vaterite I to vaterite II and from vaterite II to vaterite III occurred at pressures represented by blue-shaded regions from 3.7 to 4.7 GPa and at 8.7 GPa, respectively.

## Chapter 4. Pressure response of vaterite

At 13.1 GPa, new diffraction peaks denoted by purple asterisks in Figure 4-4 appeared around  $20^\circ$  in  $2\theta$ . These peaks were derived from several spots on the imaging plate (see Figure 4-9), suggesting the formation of coarse grains derived from another pressure-induced phase transition. The formation of coarse grains was reproduced from several experiments. No previous study reported such spots, and these peaks were not explainable by the diffraction peaks from any high-pressure polymorphs of  $\text{CaCO}_3$  expected in the pressure region: calcite III, calcite VI (Fiquet et al., 1994; Merlini et al. 2012), and aragonite (De Villiers 1971). These results indicate that the new spots appearing at 13.1 GPa are derived from another high-pressure phase of vaterite (hereinafter, vaterite IV), which transformed from not calcite III but vaterite III. The formation of vaterite IV supports the inference that not all of vaterite II transformed to calcite III.

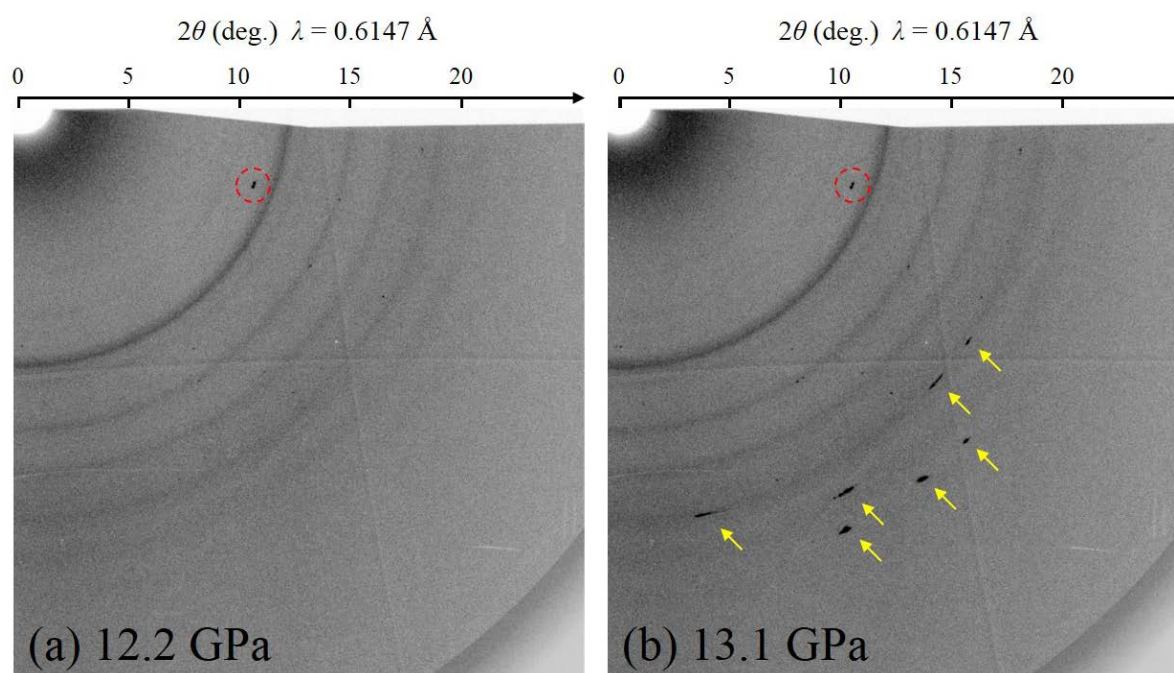


Figure 4-9. Two-dimensional diffraction patterns of vaterite sample at 12.2 GPa (a) and 13.1 GPa (b), respectively. Yellow arrows denote diffraction spots at  $19.2^\circ$ ,  $20.4^\circ$ , and  $21.7^\circ$  in  $2\theta$ . The spots surrounded by red dotted circles at  $11.6^\circ$  in both images are identified as the 104 of calcite I attached outside of DAC.

#### **4.3.4. X-ray diffraction patterns at high pressure with decompression**

Figure 4–10 shows representative XRD patterns with decompression. Vaterite IV denoted by purple asterisks disappeared at 11.6 GPa. The phase transition from vaterite III to vaterite IV is reversible, and vaterite IV can exist at pressures higher than 13.1 GPa.

Under further decompression, back transformations from vaterite III to vaterite II occurred at 5.5 GPa (see Figure 4–10), which is a notably low pressure at 8.0 GPa compared to the transition pressure from vaterite II to vaterite III (see Figure 4–4). After decompression to ambient pressure, it is noteworthy that the reflections attributable to vaterite were notably broad compared with those of the initial vaterite before compression, which suggests that the recovered sample did not back-transform completely to vaterite I or had defects. Figure 4–11 shows the variation of unit-cell parameters refined using Le Bail's structure. At pressure from 0.7 to 0 GPa, the discontinuous changes were observed in all parameters, and approached toward initial values. These observations present two possibilities: vaterite II remained even at ambient pressure; alternatively, an intermediate state between vaterite I and vaterite II existed.

On the other hand, calcite III transformed to calcite I after decompression to ambient pressure (see Figure 4–10). This result suggests that the transition from vaterite II to calcite III was irreversible.

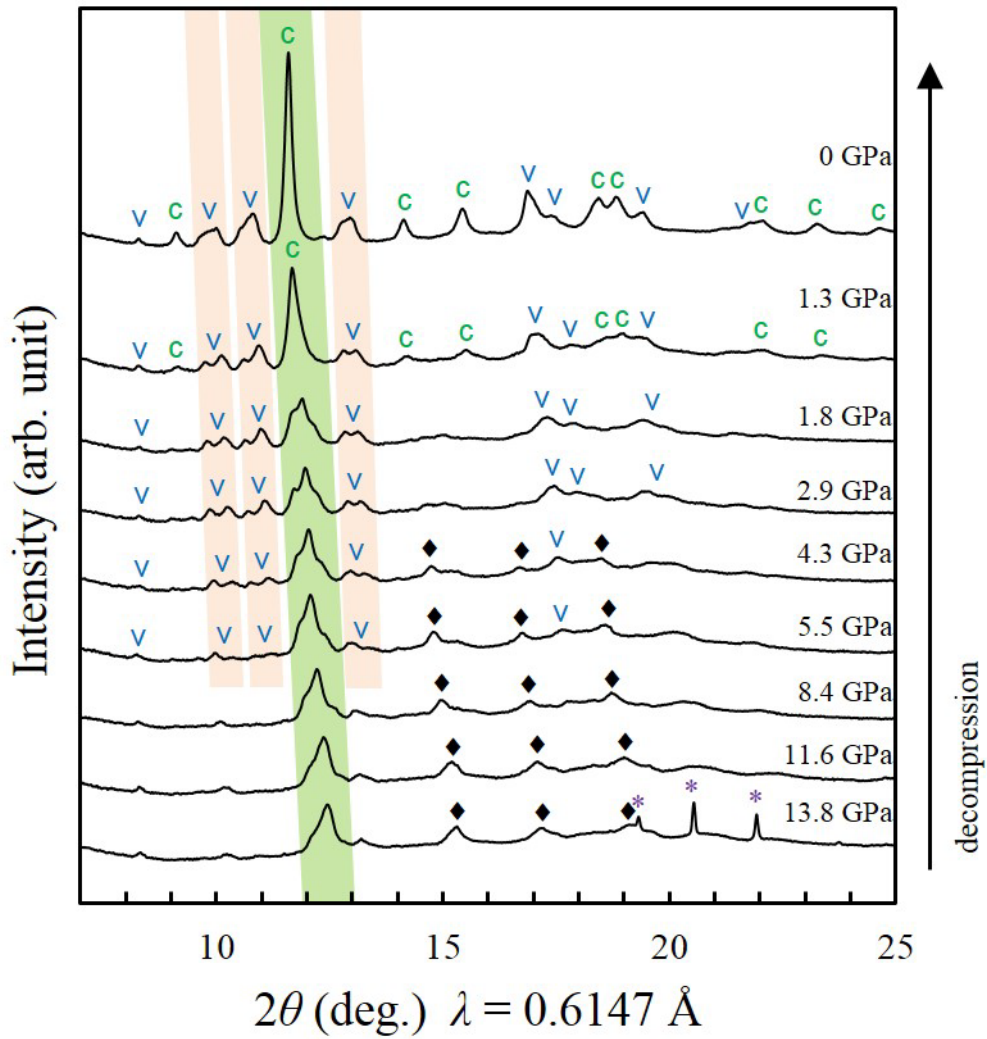


Figure 4–10. Representative XRD patterns at high pressure with decompression. The intensity has been normalized to the same measurement time. ‘c’ and ‘v’ denote the peaks of calcite I and the combination of split peaks and residue of vaterite, respectively. The orange-shaded regions indicate three main peaks of vaterite. The green-shaded region means the highest intensity peaks of calcite III, calcite II, and calcite I. Black-solid diamonds and purple asterisks denote the peaks observed with compression at 8.0 GPa (vaterite III) and 13.1 GPa (vaterite IV), respectively.

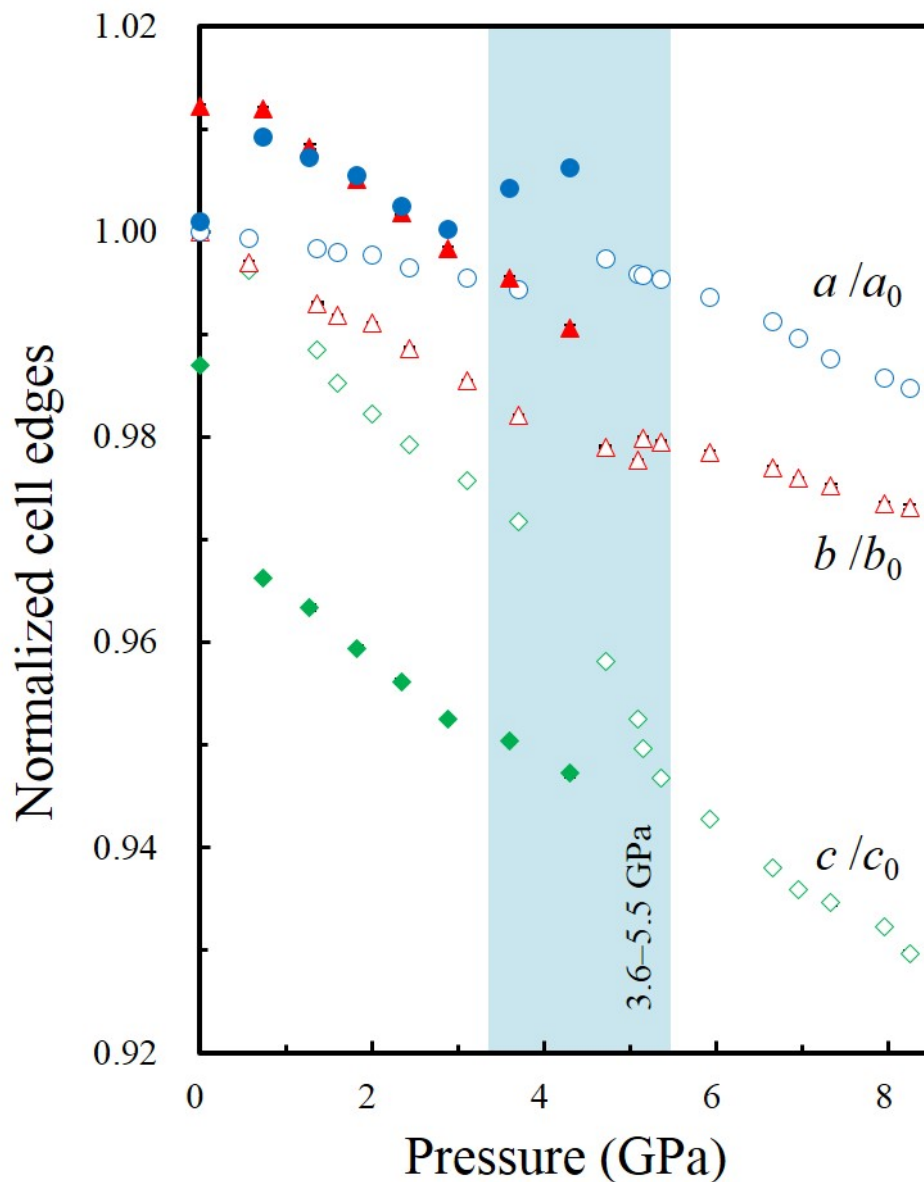


Figure 4–11. Axial compressibility of vaterite normalized to the ambient pressure. Solid and open symbols represent with decompression and with compression, respectively. Error bars are smaller than the symbol sizes. Blue-shaded region means the pressure range of co-existence of vaterite II and vaterite III at 3.6–4.3 GPa, which suggests that the obtained values of unit cell parameters of vaterite II may be affected by vaterite III.

### 4.3.5. Raman spectra of vaterite and calcite at high pressure

Figure 4–12 shows the variation of Raman spectra of calcite and vaterite under high pressure. There are many reports about Raman spectra of calcium carbonate at ambient pressure (Porto et al., 1966; Scheetz and White, 1977; Kontoyannis and Vagenas, 2000; Addadi et al., 2003; Wehrmeister et al., 2010). Strong Raman modes around  $1100\text{ cm}^{-1}$  are attributable to the symmetric stretching vibration ( $\nu_1$ ) of carbonate group (see right columns of Figure 4–12). Weak peaks in the  $700\text{--}800\text{ cm}^{-1}$  region and around  $870\text{ cm}^{-1}$  are due to in-plane bending ( $\nu_4$ ) and out-of-plane bending ( $\nu_2$ ), respectively (see center columns of Figure 4–12). Raman peaks at  $100\text{--}400\text{ cm}^{-1}$  are associated with lattice modes (see left columns of Figure 4–12). In this study, the  $\nu_3$  band observed at  $1400\text{--}1500\text{ cm}^{-1}$  was undetected because of the fluorescence of diamond anvils.

At ambient pressure and ambient temperature, calcite I has five peaks in Raman spectrum:  $\nu_1$  at  $1085\text{ cm}^{-1}$ ,  $\nu_3$  at  $1435\text{ cm}^{-1}$ ,  $\nu_4$  at  $711\text{ cm}^{-1}$ , and lattice modes at  $155\text{ cm}^{-1}$  and  $281\text{ cm}^{-1}$  (Wehrmeister et al., 2010). In Raman spectra of calcite I, no peak associated with  $\nu_2$  is observed because of the inversion symmetry of the crystal structure of calcite I (Fong and Nicol, 1971; Wehrmeister et al., 2010). At 2.1 GPa, the appearance of  $\nu_2$  and the split of  $\nu_4$  were observed in Figure 4–12 (a), which indicates the existence of calcite II (Fong and Nicol, 1971; Liu and Mernagh, 1990). It is known that calcite II transforms to calcite III at 1.8–2.5 GPa (Bridgman, 1939; Liu and Mernagh, 1990; Suito et al., 2001; Merlini et al., 2012). The Raman spectra of calcite III were characterized by split of  $\nu_1$ , three peaks of  $\nu_4$ , and additional peaks in the region of lattice modes (Fong and Nicol, 1971; Liu and Mernagh, 1990). In Figure 4–12 (a), the shoulder peak in  $\nu_1$  indicates the existence of calcite III at 2.7 GPa. After the transition to calcite III (at 4.5–12.4 GPa), peak shift and peak broadening were observed, which suggests no transformation of calcite III. Under decompression, calcite III back-transformed to calcite I via calcite II, reversibly. The Raman observation on calcite is consistent with previous studies which reported the pressure-induced phase transition of calcite (Fong and Nicol, 1971; Liu and Mernagh, 1990; Suito et al., 2001).

Chapter 4. Pressure response of vaterite

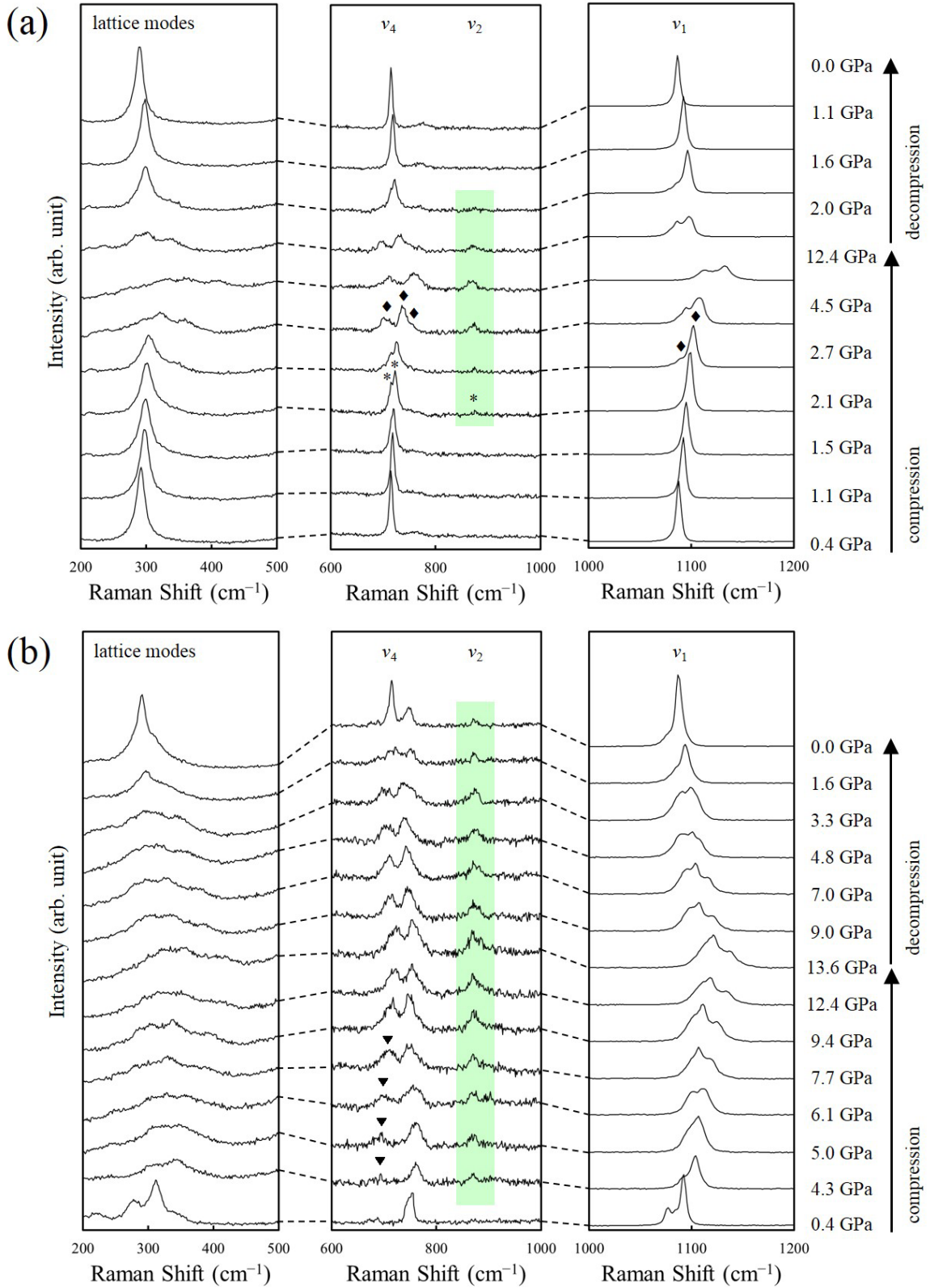


Figure 4–12. Representative Raman spectra of calcite (a) and vaterite (b) at high pressure, respectively. Green regions present the appearance of  $\nu_2$  peaks. Asterisks and solid diamonds denote calcite II and calcite III, respectively, at first-observed pressures. Solid triangles denote calcite III becoming prominent gradually.

## Chapter 4. Pressure response of vaterite

On the other hand, vaterite I has more complex Raman spectrum than that of calcite I at ambient pressure and ambient temperature. Wehrmeister et al. (2010) reported Raman band positions of the internal modes of the carbonate ion in vaterite. According to their study, the most intense Raman band  $\nu_1$  consists of two strong peaks (1075 and 1091  $\text{cm}^{-1}$ ) and one weak peak (1081  $\text{cm}^{-1}$ ). The peaks in  $\nu_4$  region and lattice modes can be decomposed to six peaks (666, 672, 685, 738, 743, and 751  $\text{cm}^{-1}$ ) and to eight peaks (106, 120, 151, 175, 210, 268, 302, and 333  $\text{cm}^{-1}$ ). The very weak peaks around 875  $\text{cm}^{-1}$  and 1450  $\text{cm}^{-1}$  are assigned to  $\nu_2$  and  $\nu_3$ , respectively. Although the peaks assignable to  $\nu_2$  and  $\nu_3$  could be undetected in the initial vaterite at 0.4 GPa, most of these features were suited to the obtained result of initial vaterite in this study (see Figure 4–12 (b)).

At high pressure, the line shapes of  $\nu_1$  changed significantly (see right column of Figure 4–12 (b)). The peak positions in  $\nu_1$  region are plotted in Figure 4–13. The discontinuous changes were observed at 5.0 and 7.7 GPa, and a new additional peak component appeared at 8.6 GPa. These changes are consistent with the results from XRD measurements; first one indicates the phase transition from vaterite I to vaterite II, and second one indicates that from vaterite II to vaterite III. In the  $\nu_2$  region, the peak at 875  $\text{cm}^{-1}$  was observed at pressures higher than 4.3 GPa with compression (see green region in Figure 4–12 (b)). This peak remained after decompression to ambient pressure, which suggests that the peak of  $\nu_2$  is assignable to not only calcite III but also vaterite II. In the  $\nu_4$  region, the peak at about 700  $\text{cm}^{-1}$  appeared at 5.0 GPa, and became prominent gradually with increasing pressure (see solid triangles in Figure 4–12 (b)), which suggests that this peak is attributable to calcite III because of the same behavior as the results from XRD measurements. The peaks of lattice modes broadened with compression, and were undetected at high pressure (see left column of Figure 4–12 (b)). After decompression to ambient pressure, a peak at about 290  $\text{cm}^{-1}$  assignable to calcite I and a shoulder peak at about 310  $\text{cm}^{-1}$  assignable to vaterite I were observed. These results from Raman spectra are consistent with the observations by XRD study.

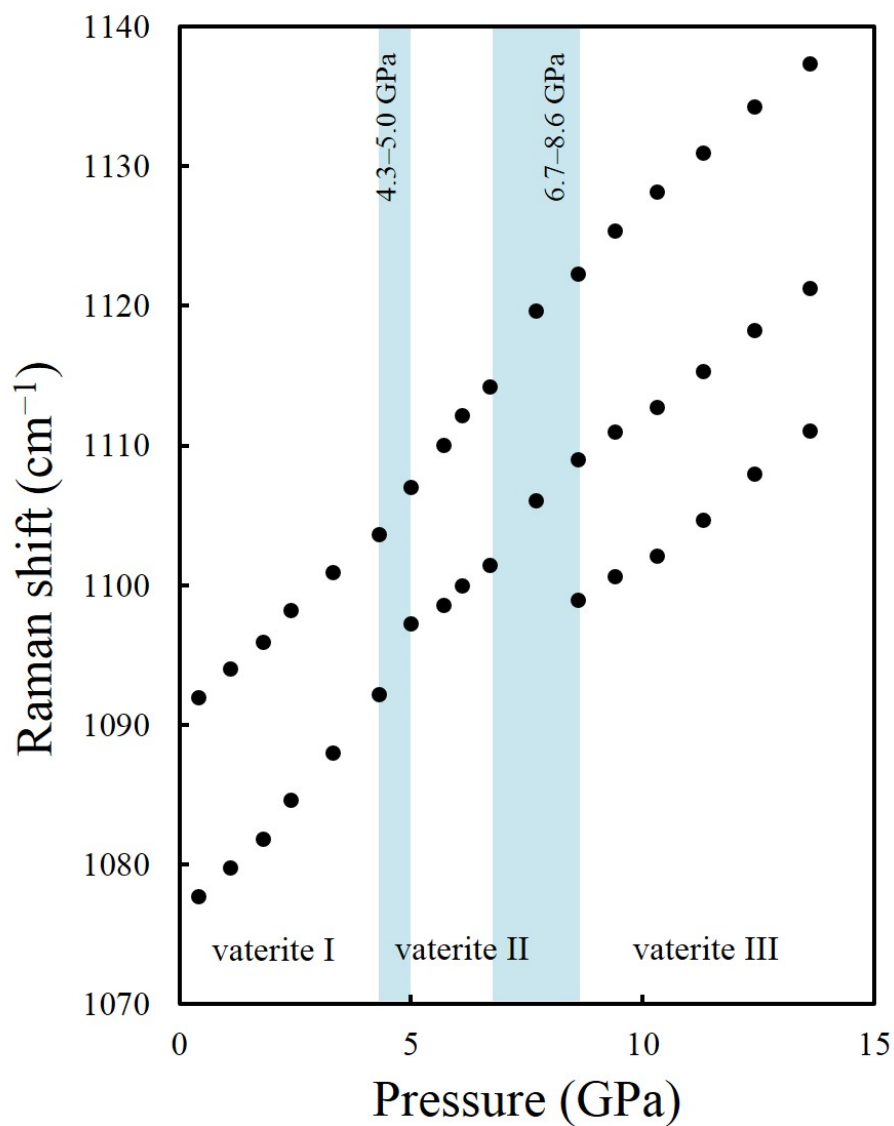


Figure 4–13. Pressure dependence of Raman peaks of vaterite in the  $\nu_1$  region. The phase transitions from vaterite I to vaterite II and from vaterite II to vaterite III occurred at pressures represented by blue-shaded regions from 4.3 to 5.0 GPa and from 6.7 to 8.6 GPa, respectively.

**4.3.6. Summary of phase transitions of vaterite at high pressure**

Figure 4–14 shows phase transition pathways of vaterite at high pressure and at room temperature, suggested from this study. Only the phase transition from vaterite II to calcite III is irreversible, which results in two sequences of pressure-induced phase transitions in parallel. Kabalah-Amitai et al. (2013) reported that vaterite comprises at least two crystallographic structures interspersed in the structure: a major structure with hexagonal symmetry and minor structure, which is still unknown. The two sequences phase transition of vaterite may be caused by two types of vaterite I with different crystal structures, which transform to vaterite III and calcite III via vaterite II, respectively.

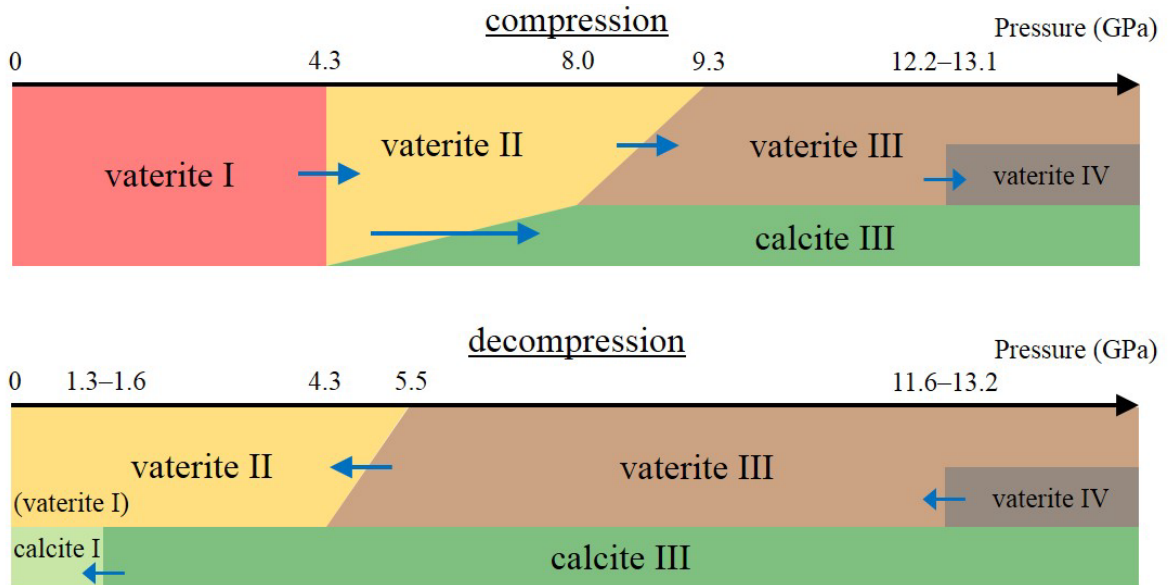


Figure 4–14. Schematics of phase transition pathways of vaterite with compression and decompression suggested from the results of XRD measurements and Raman spectroscopy.

## **4.4. Conclusion**

In this study, the high-pressure behavior of vaterite was investigated using DACs. I proposed new high-pressure phases of vaterite (vaterite II, vaterite III, and vaterite IV). However, the crystal structures of these phases, including vaterite I, have been unsolved. Although a large-size single crystal of vaterite I needed for a single-crystal experiment has not been still obtained, synthesizing a large-size single crystal of vaterite I will provide us well understandings for not only the crystal structure of vaterite I but also those of its high-pressure phases. The present study clarified that vaterite underwent very complex pressure-induced phase transitions (see Figure 4-14), which may be caused by the metastability of vaterite. The high-pressure behavior of vaterite will give us important insights into understanding high-pressure phase transitions of thermodynamically metastable minerals.

Moreover, no phase transition from vaterite I was observed below 1 GPa. This result is consistent with the results described in Chapter 3, suggesting that calcite transformed not via vaterite but from ACC directly.

## References

- Addadi L, Raz S, and Weiner S (2003) Taking Advantage of Disorder: Amorphous Calcium Carbonate and Its Roles in Biomineralization. *Advanced Materials*, **15**, 959–970.
- Bridgman PW (1939) THE HIGH PRESSURE BEHAVIOR OF MISCELLANEOUS MINERALS. *American Journal of Science*, **237**, 7–18.
- Cole WF, and Kroone B (1959) Carbonate Minerals in Hydrated Portland Cement. *Nature*, **184**, B.A.57.
- De Villiers JPR (1971) CRYSTAL STRUCTURES OF ARAGONITE, STRONTIANITE, AND WITHERITE. *The American Mineralogist*, **56**, 758–767.
- Demichelis R, Raiteri P, Gale JD, and Dovesi R (2013) The Multiple Structures of Vaterite. *Crystal Growth & Design*, **13**, 2247–2251.
- Fiquet G, Guyot F, and Itié JP (1994) High-pressure X-ray diffraction study of carbonates:  $\text{MgCO}_3$ ,  $\text{CaMg}(\text{CO}_3)_2$ , and  $\text{CaCO}_3$ . *American Mineralogist*, **79**, 15–23.
- Fong MY, and Nicol M (1971) Raman Spectrum of Calcium Carbonate at High Pressures. *The Journal of Chemical Physics*, **54**, 579–585.
- Gauldie RW, Sharma SK, and Volk E (1997) Micro-Raman Spectral Study of Vaterite and Aragonite Otoliths of the Coho Salmon, *Oncorhynchus kisutch*. *Comparative Biochemistry and Physiology*, **118**, 753–757.
- Kabalah-Amitai L, Mayzel B, Kauffmann Y, Fitch AN, Bloch L, Gilbert PUPA, and Pokroy B (2013) Vaterite Crystals Contain Two Interspersed Crystal Structures. *Science*, **340**, 454–457.
- Kamhi SR (1963) On the Structure of Vaterite,  $\text{CaCO}_3$ . *Acta Crystallographica*, **16**, 770–772.
- Kontoyannis CG, and Vagenas NV (2000) Calcium carbonate phase analysis using XRD and FT-Raman spectroscopy. *Analyst*, **125**, 251–255.
- Larson AC, and Von Dreele RB (1994) General Structure Analysis System (GSAS). *Los Alamos National Laboratory Report LAUR*, 86–748.
- Le Bail A, Ouhenia S, and Chateigner D (2011) Microtwinning hypothesis for a more ordered vaterite model. *Powder Diffraction*, **26**, 16–21.
- Liu LG, and Mernagh TP (1990) Phase transitions and Raman spectra of calcite at high pressures and room temperature. *American Mineralogist*, **75**, 801–806.
- Liu LG, Chen CC, Lin CC, and Yang YJ (2005) Elasticity of single-crystal aragonite by Brillouin

## Chapter 4. Pressure response of vaterite

- spectroscopy. *Physics and Chemistry of Minerals*, **32**, 97–102.
- Mao HK, Xu J, and Bell PM (1986) Calibration of the Ruby Pressure Gauge to 800 kbar Under Quasi-Hydrostatic Conditions. *Journal of Geophysical Research*, **91**, 4673–4676.
- Martinez I, Zhang J, and Reeder RJ (1996) In situ X-ray diffraction of aragonite and dolomite at high pressure and high temperature: Evidence for dolomite breakdown to aragonite and magnesite. *American Mineralogist*, **81**, 611–624.
- Merlini M, Crichton WA, Chantel J, Guignard J, and Poli S (2014) Evidence of interspersed co-existing CaCO<sub>3</sub>-III and CaCO<sub>3</sub>-IIIb structures in polycrystalline CaCO<sub>3</sub> at high pressure. *Mineralogical Magazine*, **78**, 225–233.
- Merlini M, Hanfland M, and Crichton WA (2012) CaCO<sub>3</sub>-III and CaCO<sub>3</sub>-VI, high-pressure polymorphs of calcite: Possible host structures for carbon in the Earth's mantle. *Earth and Planetary Science Letters*, **333–334**, 265–271.
- Merrill L, and Bassett W (1975) The Crystal structure of CaCO<sub>3</sub>(II), a High-Pressure Metastable Phase of Calcium Carbonate. *Acta Crystallographica*, **B31**, 343–349.
- Meyer HJ (1959) Über Vaterit und seine Struktur. *Angewandte Chemie*, **71**, 678–679.
- Meyer HJ (1969) Struktur und Fehlordnung des Vaterits. *Zeitschrift für Kristallographie*, **128**, 183–212.
- Ogino T, Suzuki T, and Sawada K (1987) The formation and transformation mechanism of calcium carbonate in water. *Geochimica et Cosmochimica Acta*, **51**, 2757–2767.
- Olshausen S (1925) Strukturuntersuchungen nach der Debye-Scherrer-Methode. *Zeitschrift für Kristallographie*, **61**, 463–514.
- Ono S, Kikegawa T, Ohishi Y, and Tsuchiya J (2005) Post-aragonite phase transformation in CaCO<sub>3</sub> at 40 GPa. *American Mineralogist*, **90**, 667–671.
- Porto SPS, Giordmaine JA, and Damen TC (1966) Depolarization of Raman Scattering in Calcite. *Physical Review*, **147**, 608–611.
- Redfern SAT, (2000) Structural Variations in Carbonates. *Reviews in Mineralogy and Geochemistry*, **41**, 289–308.
- Redfern SAT, and Angel RJ (1999) High-pressure behavior and equation of state of calcite, CaCO<sub>3</sub>. *Contrib Mineral Petrol*, **134**, 102–106.
- Scheetz BE, and White WB (1977) Vibrational spectra of the alkaline earth double carbonates. *American Mineralogist*, **62**, 36–50.
- Seto Y, Nishio-Hamane D, Nagai T, and Sata N (2010) Development of a Software Suite on X-ray

## Chapter 4. Pressure response of vaterite

- Diffraction Experiments. *The Review of High Pressure Science and Technology*, **20**, 269–276.
- Seto Y (2012) Whole Pattern Fitting for Two-Dimensional Diffraction Patterns from Polycrystalline Materials. *The Review of High Pressure Science and Technology*, **22**, 144–152.
- Suito K, Namba J, Horikawa T, Taniguchi Y, Sakurai N, Kobayashi M, Onodera A, Shimomura O, and Kikegawa T (2001) Phase relations of CaCO<sub>3</sub> at high pressure and high temperature. *American Mineralogist*, **86**, 997–1002.
- Takemura K, Sahu PCh, Yoshiyasu K, and Yasuo T (2001) Versatile gas-loading system for diamond anvil cells. *Review of Scientific Instruments*, **72**, 3873–3876.
- Toby BH (2001) EXPGUI, a graphical user interface for GSAS. *Journal of Applied Crystallography*, **34**, 210–213.
- Vo Thanh D, and Lacam A (1984) Experimental study of the elasticity of single crystalline calcite under high pressure (the calcite I–calcite II transition at 14.6 kbar). *Physics of the Earth and Planetary Interiors*, **34**, 195–203.
- Wang J, and Becker U (2009) Structure and carbonate orientation of vaterite (CaCO<sub>3</sub>). *American Mineralogist*, **94**, 380–386.
- Wehrmeister U, Soldati AL, Jacob DE, Häger T, and Hofmeister W (2010) Raman spectroscopy of synthetic, geological and biological vaterite: a Raman spectroscopic study. *Journal of Raman Spectroscopy*, **41**, 193–201.
- Zha CS, Mao HK, and Hemley RJ (2000) Elasticity of MgO and a primary pressure scale to 55 GPa. *Proceedings of the National Academy of Sciences of the United States of America*, **97**, 13494–13499.

*Chapter 4. Pressure response of vaterite*

## **Chapter 5.**

### **Conclusions of this thesis**

## *Chapter 5. Conclusions of this thesis*

In the present study, pressure responses of ACC and vaterite, which are metastable phases of calcium carbonate, were investigated to understand the recently reported pressure-induced crystallization from ACC to calcite and vaterite. The experiments based on the recovered samples indicate that the crystallization pressure and the polymorph ratio were dependent on water contents of ACC, which restricts the crystallization mechanism.

In situ time-resolved XRD measurements observed with increasing pressure clarified the kinetics and mechanisms of pressure-induced crystallization of ACC. Time-resolved XRD patterns indicate that the crystallization from ACC to calcite and vaterite occurred almost simultaneously, which is different from the sequential crystallization of ACC observed in a supersaturated aqueous solution. Moreover, SEM images and Raman spectra of the recovered sample indicate that calcite and vaterite had different texture and distribution, suggesting the difference of crystallization mechanisms. The formation of vaterite proceeds by dissolution-reprecipitation process, which is the same process as that in a supersaturated solution. On the other hand, calcite transforms by solid-solid phase transition process. This direct transformation from ACC to calcite is also suggested by the results from high-pressure experiments of vaterite.

Pressure-induced phase transitions of vaterite at room temperature were observed using powder XRD and Raman spectroscopic methods. This study proposed new high-pressure phases of calcium carbonate: vaterite II, vaterite III, and vaterite IV. In particular, vaterite II, which transformed from vaterite I at 4.3 GPa, could be described as a distortion of vaterite I. However, the crystal structures of these high-pressure phases including vaterite I remain unsolved. Although a large-size single crystal of vaterite I has not been still obtained, it is expected to determine these crystal structures by single-crystal XRD studies in future. An irreversible pressure-induced phase transition from a part of vaterite II to calcite III was observed. This result suggests that vaterite I is composed of two different crystal structures, which is consistent with a recent report by Kabalah-Amitai et al. (2013).

## *Chapter 5. Conclusions of this thesis*

The present study reveals several phase transitions of metastable phases under high pressure and at room temperature. These phase transitions are very complex, which may be caused by the metastability of these phases. The obtained results will give us important insights into understanding high-pressure phase transitions of thermodynamically metastable minerals and materials, which have many unknown parts. In addition, these phase transitions might provide some clues to elucidate the crystal structure of vaterite I.

The phase transitions at high pressure presented in this thesis are not directly related to the reactions in biomineralization because pressure in which crystallization from ACC occurs is much higher than pressure environments for livings producing biominerals. However, pressure-induced crystallization is expected to provide useful information as a possible crystallization process of ACC to understand biomineralization. In addition, this study shows a possibility that the pressure-induced crystallization of ACC can be applied to material science. The crystallization and molding of ACC can be conducted simultaneously by applying pressure. If polymorph ratio can be controlled, it is expected to engender developments of new materials.

## **Acknowledgements**

First of all, I would like express my gratitude to the supervisor, Prof. H. Kagi. He provided me the opportunity of this study and enormous support for almost seven years. Special thanks also go to the supervisors, Prof. K. Notsu and Prof. K. Nagao. I am very grateful to Dr. T. Yoshino for giving me experimental supports and many useful advices about calcium carbonate. Dr. K. Komatsu gave me many comments about crystallography and high-pressure experiments. I would like to thank Prof. T. Inoue and Prof. H. Ohfuji for providing technical support and practical advice on high-pressure experiments. Prof. M. Nara provided me technical support on the measurements of ATR. Dr. S. Nakano technically helped with He-gas loading. Prof. K. Sugiyama and Dr. H. Arima taught me about PDF analysis. Mr. H. Suenami, Mr. S. Kakizawa, and Dr. N. Cai, who are/were the members of Prof. Inoue's laboratory, gave me technical support for the experiments at the synchrotron facility. Finally, I appreciate generous support by all members of Geochemical Research Center.

This study was financially supported by Grant-in-Aid for JSPS Fellows from the Japan Society for Promotion of Science (JSPS), Global COE Programs (Chemistry Innovation through Cooperation of Science and Engineering, the University of Tokyo; Center for Advanced Experimental and Theoretical Deep Earth Mineralogy, Ehime University) from MEXT in Japan, and KIGAM Basic Research Program.